UNIVERSITY OF CALIFORNIA,
IRVINE

Hygroscopicity of Amphiphilic Nanoparticles:

The Role of Size and Composition

DISSERTATION

submitted in partial satisfaction of the requirements
for the degree of

DOCTOR OF PHILOSOPHY

in Chemistry

by

Christopher Warren Harmon

Dissertation Committee:
Professor Sergey A. Nizkorodov, Chair
Professor Barbara J. Finlayson-Pitts
Professor Douglas J. Tobias

2009

ProQuest LLC
789 East Eisenhower Parkway
P.O. Box 1346
Ann Arbor, MI 48106-1346

DEDICATION

To my parents, Elza and Patricia Harmon, who continually provided support and enthusiasm, without which, none of this would be possible.

"Without struggle, there can be no progress."

Frederick Douglas, 1857

"If I have been able to see further,
it was only because I stood on the shoulders of giants"

Sir Isaac Newton, 1675

TABLE OF CONTENTS

LIST OF FIGURES

Chapter 1 – Water Uptake by Atmospheric Aerosols

Chapter 2 – Experimental Approach for Studying Hygroscopic Growth of Amphiphilic Nanoparticles

Chapter 3 – Hygroscopic Growth and Deliquescence of NaCl Nanoparticles

Chapter 4 – Hygroscopic Growth and Deliquescence of SDS/NaCl Nanoparticles

Chapter 5 – Characterization of SDS/NaCl Nanoparticles

Chapter 6 – Final Remarks and Suggested Future Work

LIST OF TABLES

ACKNOWLEDGEMENTS

I would like to express my sincere gratitude to my research advisor, Professor Sergey A. Nizkorodov, whose infinite patience, benevolence, and comradery was a constant source of inspiration. He continually challenged me and allowed me to work, as I desired, which I am forever thankful for. Without his guidance and friendship this dissertation would not have been possible.

I would like to thank my committee members, Professor Barbara J. Finlayson-Pitts and Professor Douglas. J. Tobias, whose teachings and wisdoms I will be a student of for a long time to come. Professor Finlayson-Pitts is a world-class educator and I am honored to have learned from her. Professor Tobias is one of the most personable professionals I have ever met and this makes him a role model for future researchers and educators.

In addition, I would like to express my kindest regards for Professor R. Benny Gerber, whose ability to convey difficult concepts in chemistry is only rivaled by his sincere friendship and compassion for his fellow colleagues.

This dissertation would not have been possible without the Graduate Assistance in Areas of National Need award in 2005-2006, the AirUCI Institute, which is funded by the National Science Foundation, and the Dean's Dissertation Fellowship in 2009.

Lastly, I would like to express my deepest thanks for my friends and colleagues in the AirUCI Institute: Theresa McIntire, Ron Grimm, Adam Bateman, Lisa Wingen, Ming Cheng, Samar Moussa, Steve Mang, Ahmad Alshawa, Vanessa Angel, Bosa Njegic, and Mark Peterson, all of whom contributed to this dissertation in one way or another.

385A Rowland Hall
Irvine, CA 92697-2025
Office: (949) 824-7473
fax: (949) 824-8571

Christopher W. Harmon

Curriculum Vitae

University of California, Irvine
Department of Chemistry,
The AirUCI Institute
cwharmon@uci.edu

PROFESSIONAL EXPERIENCE

United States Environmental Protection Agency,

Region 5 Central Region Laboratory (U.S. E.P.A., Region 5 C.R.L)…….2004 – 2005

Chicago, IL: Field/Analytical Scientist

EDUCATION

University of California, Irvine – Ph.D. in Physical Chemistry……2005 – 2009

Irvine, CA: August 2005 – November 2009

Purdue University – B.S. in Chemistry……2000 – 2004

West Lafayette, IN

RESEARCH EXPERIENCE

University of California, Irvine……..2007 – 2009

Research Advisor: Prof. Sergey A. Nizkorodov

Area of Study: Hygroscopicity of Amphiphilic Nanoparticles

University of California, Irvine……..2005 – 2007

Research Advisor: Prof. Barbara J. Finlayson-Pitts

Area of Study: Photolytic Induction of Secondary Organic Aerosol Formation

Purdue University……2003 – 2004

Research Advisor: Prof. Paul Shepson

Area of Study: Heterogeneous Ice Crystal Morphology and Formation

TEACHING EXPERIENCE

University of California, Irvine……..2005 – 2009

Chem 152: lab TA **Advanced Analytical Chemistry** Winter ’08 & Winter ‘06

Chem 1A & 1B: discussion TA **General Chemistry** Fall ’07 & Spring ‘05 respectively

PUBLICATIONS

1. Christopher W. Harmon, Ronald L. Grimm, Theresa M. McIntire, Mark Peterson, Bosiljka Njegic, Vanessa M. Angel, Ahmad Alshawa, Joelle S. Underwood, Douglas J. Tobias, R. Benny Gerber, Mark S. Gordon, John C. Hemminger, Sergey A. Nizkorodov, ***“Hygroscopic Growth and Deliquescence of NaCl Nanoparticles Mixed with Surfactant SDS,”*** *(2009)* **in submitted to** *J.P.C. B*

2. Christopher W. Harmon, Steve A. Mang, John Greaves and Barbara J. Finlayson-Pitts, ***“Identification of Phospholipids, Fatty Acids in Oils and Their Oxidation Products using Matrix Assisted Laser Desorption Ionization (MALDI) Mass Spectrometry and Electrospray Ionization Mass Spectrometry (ESI-MS),”*** *J. Chem. Ed. (2009)* **submitted and under review**

3. Ahmad Alshawa, Otto Dopfer, Christopher W. Harmon, Sergey A. Nizkorodov and Joelle S. Underwood ***“Hygroscopic Growth and Deliquescence of NaCl Nanoparticles Coated with Surfactant AOT,”*** *J. Phys. Chem. A (2009),* **DOI: 10.1021/jp809869r**

PUBLICATIONS CONTINUED

4. Yong Yu, Michael J. Ezell, Alla Zelenyuk, Dan Imre, Liz Alexander, John Ortega, Barbara D'Anna, Chris W. Harmon, Stanley N. Johnson and Barbara J. Finlayson-Pitts ***"Photooxidation of α-pinene at High Relative Humidity in the Presence of Increasing Concentrations of NO_x"*** *Atmos. Envirn. (2008),* **DOI: 10.1016/j.atmosenv**

5. Yong Yu, Michael J. Ezell, Alla Zelenyuk, Dan Imre, Liz Alexander, John Ortega, Jennie L. Thomas, Karun Gogna, Douglas J. Tobias, Barbara D'Anna, Chris W. Harmon, Stanley N. Johnson and Barbara J. Finlayson-Pitts *"**Nitrate Ion Photochemistry at Interfaces: A New Mechanism for Oxidation of α-pinene**," Phys. Chem. Chem. Physics* (2008), **DOI: 10.1039/b719495a**

AWARDS

University of California, Irvine……2005 – 2009

2009 – 2010 Recipient of the Dean's Dissertation Fellowship

2008 – 2009 Recipient of the Joan Rowland award

2006 – 2007 Upperclassman Co-TA of the Year

2005 – 2006 Graduate Assistance in Areas of National Need Fellow (GAANN)

U.S. E.P.A., Region 5 C.R.L……..2004 – 2005

2004 – 2005 Oakridge Research Institute for Science Education Fellow (ORISE)

Purdue University……2000 – 2004

2002 – 2003 Skull and Crescent Junior-Greek Leadership Honorary

2000 – 2001 National Society of Collegiate Scholars

2000 – 2001 Alpha Lambda Delta Freshman Honor Society

2000 – 2001 Phi Etta Sigma Freshman Honor Society

ORAL PRESENTATIONS

1. AirUCI Annual Workshop, January 2009, Laguna Beach, CA ***"Hygroscopic Growth of NaCl Nanoparticles Containing Surfactant Sodium Dodecyl Sulfate."***

2. AirUCI Seminar, October, 2008, Irvine, CA ***"Deliquescence and Thin Water Films"***

3. American Chemical Society National Meeting, April 2008, New Orleans, LA ***"Hygroscopicity of Amphiphilic Nanoparticles: The Role of Size and Composition for Potential Cloud Condensation Nuclei."***

4. AirUCI Annual Workshop, February 2008, Newport Beach, CA "***Hygroscopicity of Amphiphilic Nanoparticles: The Role of Size and Composition."***

5. Original Proposal for Ph.D. Candidacy, September 2007, Irvine, CA ***"Circular Dichroism Spectra of AminoAcids in Conditions Relevant to Space as an Investigation to the Origin of Biomolecular Homochirality."***

6. Research Progress for Ph.D. Candidacy, September 2007, Irvine, CA ***"Photolytic Sodium Nitrate as a Precursor to Secondary Organic Aerosol Formation."***

7. AirUCI Seminar, April, 2007, Irvine, CA ***"Secondary Organic Aerosol Formation: Achieving Mass Balance."***

8. U.S. E.P.A., Region 5 C.R.L Final Methodology Report, May 2005, Chicago, IL ***"Method Implementation of VOC Analysis using GC/MS for Air Toxicology Research."***

POSTER PRESENTATIONS

1. American Association for Aerosol Research, 2009, Minneapolis, MN. Christopher W. Harmon, Ronald L. Grimm, Theresa M. McIntire, Mark Peterson, Bosiljka Njegic, Vanessa M. Angel, Ahmad Alshawa, Joelle S. Underwood, Douglas J. Tobias, R. Benny Gerber, Mark S. Gordon, John C. Hemminger, Sergey A. Nizkorodov, ***"Hygroscopic Growth and Deliquescence of NaCl Nanoparticles Mixed with Surfactant SDS."***

2. Informal Symposium on Kinetics and Photochemistry in the Atmosphere, 2008, Los Angeles, CA.. Chris W. Harmon, Ahmad Alshawa, Joelle S. Underwood, Sergey A. Nizkorodov ***"Hygroscopicity of Amphiphilic Nanoparticles:: The Role of Size and Composition."***

3. Informal Symposium on Kinetics and Photochemistry in the Atmosphere, 2007, Los Angeles, CA. Chris W. Harmon, Yong Yu, Michael Ezell, Stanley N. Johnson, Barbara J. Finlayson-Pitts ***"A New Reactor for Studying Secondary Organic Aerosol Formation."***

OUTREACH

1. Dana Hills High School AP Environmental Science Class Oral Presentation, 2007, Dana Point, CA. ***"Chemistry in the Atmosphere."***

2. AirUCI Annual Summer Science Teacher Training Program Lab Instructor, July 2007 & 2008, Irvine, CA

3. California State Science Fair Judge, *Chemistry Upper Division*, May 2007 , 2008 & 2009, Los Angeles, CA

4. Purdue University Alumni Seminar Oral Presentation, March 2005, West Lafayette, IN. ***"Method Implementation of VOC Analysis using GC/MS for Air Toxicology Research."***

ABSTRACT OF THE DISSERTATION

Hygroscopicity of Amphiphilic Nanoparticles:

The Role of Size and Composition

By

Christopher Warren Harmon

Doctor of Philosophy in Chemistry

University of California, Irvine, 2009

Professor Sergey A. Nizkorodov, Chair

Direct and indirect effects of aerosols on radiative forcing are poorly understood; therefore fundamental processes involved in water uptake on model atmospheric surfaces were examined experimentally and theoretically. Water uptake on NaCl nanoparticles (< 20 nm) with varying coverage of sodium dodecyl sulfate (SDS) was studied because key features, such as monolayer water-uptake, are amplified in nanoparticle hygroscopic growth curves compared to larger, micron size particles. Experimental techniques employed in this work are novel due to their ability to probe hygroscopic growth of nanoparticles in the monolayer coverage regime and bulk regime without the influence of a substrate. Nanoparticles were generated with an electrospray ionization-neutralization apparatus and their hygroscopic growth was quantified by exposure, varied from 1 to 70 seconds, to relative humidity (RH) and tandem-nano-differential mobility analysis techniques. As surfactant coverage level increases in the nanoparticles water uptake begins at lower RH values compared to NaCl and no *prompt* deliquesce transition is observed, contrary to observations of larger (> 60 nm) surfactant containing NaCl nanoparticles. Hygroscopic growth is continually suppressed as surfactant coverage increases. Variance in RH

exposure time made no difference to experimental observations. Hygroscopic growth models are used to evaluate growth of NaCl and surfactant/NaCl nanoparticles. In the post-deliquescence regime, a modified version of Köhler theory is used to compare with NaCl nanoparticle growth and the Zdanovskii-Stokes-Robison model is used to evaluate surfactant/NaCl nanoparticle growth. In the pre-deliquescence regime, standard adsorption isotherms (Brunauer-Emmett-Teller and/or Frenkel-Halsey-Hill) are used to evaluate growth. A nanoparticle jet impactor has also been constructed for imaging and chemical analysis of nanoparticles. Atomic force microscopy images, X-ray photoelectron spectra and Fourier transform infrared spectra confirm the success and usefulness of the jet impactor. Characterizations of SDS/NaCl nanoparticles reveal the core-shell model, which is a commonly assumed morphology for organic-inorganic particles, may not be accurate for describing the morphology of high surfactant containing SDS/NaCl nanoparticles.

Chapter 1 – Water Uptake by Atmospheric Aerosols

Section 1.1 – *Aerosol Effects on Radiative Forcing*

1.1.1 - The Role of Atmospheric Water, both in the Condensed Phase and the Vapor Phase

Planet Earth is set aside from the other planets in our solar system due to the unique coexistence of water in its three phases: gas, liquid, and solid. The majority, roughly 97%,[1] of water on Earth is saline and exists in the oceans. The remaining 3% is fresh water, which are mostly ice caps and glaciers.[1] A very small percent of Earth's total water, some 1.0×10^{-3} %, is atmospheric water.[1] In Earth's atmosphere the coexistence of water as vapor, liquid droplets, and ice particles is crucial for maintaining the delicate balance of our climate.[2,3]

Atmospheric water plays many roles in the climate system. These roles can be sub-divided into two main categories: scattering and absorbing Earth bound radiation from the Sun. Categorizing atmospheric water is difficult because there is rarely one phase without the other on planet Earth. Nevertheless, the role of atmospheric gaseous water is an absorber of solar radiation and condensed-phase atmospheric water is a scatterer of solar radiation.[2]

Water's role as an absorber of solar radiation is related to the greenhouse effect. The greenhouse effect is the trapping of long wave radiation by atmospheric gases re-emitted from absorbed short wave solar radiation at the Earth's surface. The content of gaseous water in Earth's atmosphere is quite variable, ranging from 1-4% by volume[4] depending on the prevailing conditions. Gaseous water in the atmosphere is crucial for maintaining a comfortable average temperature of 287 K (14°C), which would be 255 K (–18°C) without the greenhouse effect.[4]

The role of water as a scatterer of solar radiation is related to Earth's albedo, which is a measure of the reflectivity of the planet. The average albedo is roughly 0.30,[5] in other words 30% of incoming visible solar radiation is scattered back to space by (mostly) clouds, glaciers,

sand, and oceans.[4] Satellite images of Earth always show global cloud cover.[5] Clouds keep the planet cool by scattering visible radiation back to space. Condensed phases of water in the atmosphere are therefore crucial for maintaining the albedo balance, which if increased or decreased will have strong influences on Earth's temperature.

1.1.2 – Aerosols as Cloud Condensation Nuclei; Indirect Effect of Aerosols on Climate

Atmospheric particles, or aerosols, can take up gaseous water and grow under high relative humidity conditions or lose water and shrink under low relative humidity conditions. The extent and magnitude of this growth is a strong function of size and composition. Aerosol has direct and indirect effects on atmospheric radiative forcing which are poorly understood.[2] Direct effects include scattering of light by particulate matter, whereas indirect effects include scattering of light by clouds and cloud condensation nuclei (CCN).[2]

Radiative forcing is used as a means to quantify the influence of a species on the climate system. Figure 1.1 is adapted from the Intergovernmental Panel on Climate Change (IPCC) 2007 report[2] and shows the radiative forcing by components of the atmosphere and the quantitative extent which they contribute to the climate system. Earth receives an average daily radiation flux of 341 W m^{-2} from the Sun.[5] The sum of all radiative forcing components illustrated in Figure 1.1 demonstrates currently the planet is in a state of warming. A flux of +0.6 to +2.4 W m^{-2}, mostly from increasing levels of longed-lived greenhouse gases such as carbon dioxide and methane, is forced into our atmosphere.[2] The indirect effect of aerosols, which is also known as the cloud albedo effect, is a consequence of aerosol acting as CCN, which forms cloud droplets by taking up water vapor from the atmosphere. This has a net cooling effect and its quantitative magnitude, –1.8 to –0.3 W m^{-2}, is poorly understood and has a wide margin of uncertainty.[6] While the quantitative magnitude of greenhouse gases in the

atmosphere are known, the total net anthropogenic radiative forcing is unknown a priori because of the uncertainty associated with the aerosol indirect effect.

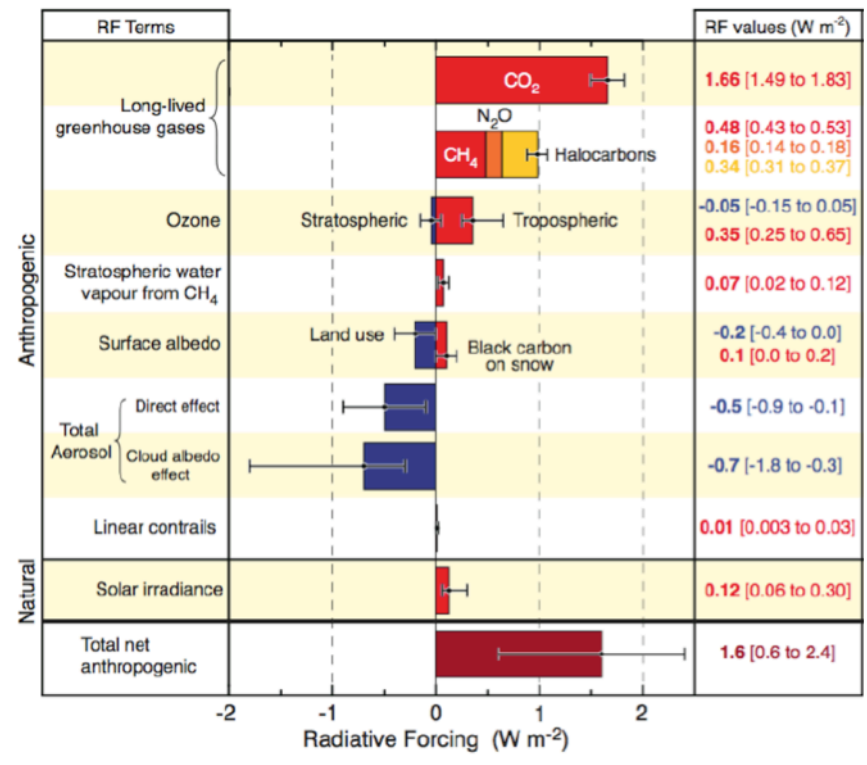

Figure 1.1: Radiative Forcing components in the atmosphere and their contribution to the climate system. Figure is adapted from Ref. 2

1.1.3 – Role of Chemical Composition and Critical Diameter for CCN Activity

Chemical composition of atmospheric particles plays an important role in water uptake. Generally, highly water-soluble species have a stronger propensity for forming CCN because they are hygroscopic, which is defined as the ability of a substance to adsorb water vapor from the surrounding environment. Aerosols that can contribute to CCN concentration in the atmosphere are called CCN-active and this not only depends on composition, but also depends on size.

CCN-active aerosol particles increase their size by a large factor to become cloud droplets when the ambient relative humidity (RH) around the particle's surface achieves

supersaturation (RH > 100%), which is common in atmospheric updrafts.[7] Because of the Kelvin effect (increase in the water vapor pressure over a curved aqueous surface) only particles above a certain size are CCN-active for a given supersaturation. Typical minimum CCN-activation diameters at 100.5 % RH are 20-30 nm and 100-200 nm for soluble inorganic and weakly soluble organic particles, respectively.[7]

1.1.4 – Unresolved Questions

Despite their larger activation diameters, atmospheric organic aerosol particles do act as CCN.[8-24] However, it is still a matter of active debate whether CCN-activity of an organic particle can be changed by atmospheric heterogeneous chemistry.[7,25-29] Furthermore, atmospheric particles are rarely pure components and often represent mixtures of hydrophobic and hydrophilic compounds.[30] There is a positive correlation between hygroscopicity and CCN-activity; more hygroscopic particles tend to have smaller CCN activation diameters.[30] Further experimentation and understanding is needed to elucidate CCN-activity of atmospherically relevant aerosols and how this contributes to the cloud albedo effect. The large uncertainty in the magnitude of the cloud albedo effect on radiative forcing in the atmosphere also substantiates the aforementioned claim.

Section 1.2 – *Review of Terminology and Basic Concepts*

1.2.1 – Mobility Growth Factor, Deliquescence and Efflorescence

Atmospheric particles can significantly expand in size by taking up water as the ambient RH around the particle's surface increases. This hygroscopic growth increases the particle's single scattering albedo and plays an important role in cloud droplet formation.[18,31] Hygroscopicity of individual particles is quantified in terms of the mobility growth factor, GF_m,

seen in equation 1.1, the ratio of the measured wet particle mobility diameter at a specified RH, $d_m(RH)$, to that of the initial, dry particle mobility diameter, $d_m(0)$.[32]

$$GF_m = \frac{d_m(RH)}{d_m(0)} \qquad (1.1)$$

The extent and rate of the hygroscopic growth is a sensitive function of the particle's chemical composition. For highly soluble inorganic particles, such as NaCl, and certain highly soluble organic particles, such as malonic acid, GF_m may experience a discontinuity at a well-defined deliquescence relative humidity (DRH) corresponding to a phase transition from a solid to a dissolved state.[31,33-36] The reverse phase transition occurs at the efflorescence relative humidity (ERH), which can be considerably lower than DRH because of kinetic constraint (see section 1.2.2). For example, NaCl particles experience almost no growth below the DRH of 75% at room temperature and pressure.[37] At the deliquescence point, NaCl particles undergo a phase transition from crystalline to aqueous droplet, which is accompanied by a prompt increase in the particle mobility diameter. The ERH for NaCl occurs at ~45%.[38]

Figure 1.2 is a demonstration of the hygroscopic growth curve (GF_m vs. RH). This coordinate system will also be referred to as growth space herein. Deliquescence and efflorescence are demonstrated by the prompt increase/decrease in growth factor.

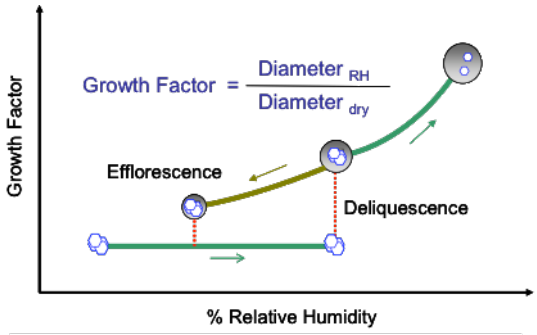

Figure 1.2: Demonstration of GF_m, deliquescence, and efflorescence for NaCl aerosol (> 100 nm). Plot of GF_m vs. RH is called a hygroscopic growth curve.

1.2.2 – Gibbs Equilibrium Condition for a Phase Transition

The Gibbs equilibrium condition for a phase transition states when two phases A and B have identical chemical potentials (μ) at a certain environmental condition (i.e. temperature, pressure, or even RH) both phases are thermodynamically stable and each will be observed.[39] As a condition of equilibrium, $\mu_A = \mu_B$ and $\Delta\mu = 0$.[39] As the condition is changed the phase which has the lowest chemical potential will be observed while the other is unstable and is not observed.[39] Figure 1.3 is an illustration of Gibbs equilibrium condition for a phase transition with respect to temperature. Below the critical temperature (indicated by the dashed line) phase A is the thermodynamically stable phase. Above the critical temperature phase B is the thermodynamically stable phase.

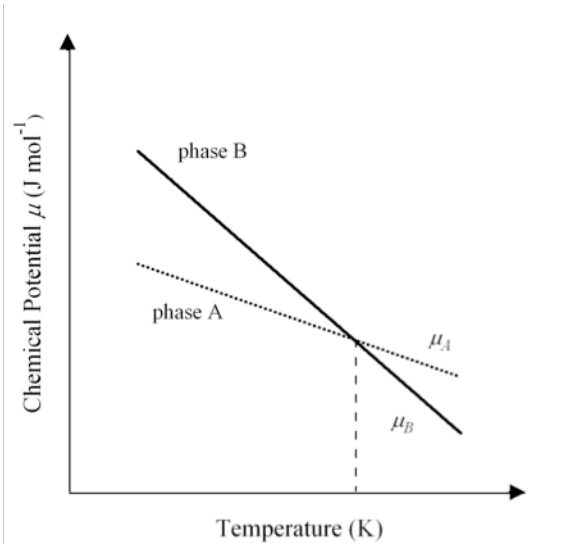

Figure 1.3: Illustration of Gibbs equilibrium condition for a phase transition with respect to temperature.

The actual stability of chemical phases can also be influenced by the time required to complete the phase transition.[39] The time needed for a transition into the thermodynamically favored state can be very slow, to the point of being unobservable on experimental time scales. This is known as kinetic stability, which often is synonymous with thermodynamic meta-stability.[39] If the time required to complete the phase transition illustrated in Figure 1.3 is long, the lifetime of the universe for example, phase A will still be observed above the critical temperature and is called the meta-stable phase.[39] One example of this in every day life is graphite and diamond. At room temperature and pressure graphite is the thermodynamically

stable phase and diamond is the kinetically stable (or meta-stable) phase.[39] Luckily, diamond jewelry purchased in this millennium won't be turning into graphite any time soon!

1.2.3 – Thermodynamics of Non-ideal Solutions

Upon deliquescence, NaCl particles become saturated aqueous solutions and subsequently become more dilute as they take on more water. Due to the non-ideality associated with concentrated electrolyte solutions, solubility, free energy of mixing, freezing-point depression, boiling-point elevation, osmotic pressure, and vapor pressure must be determined experimentally.[39]

Gas-phase water always exists over surfaces of bulk liquids, ices and atmospheric particles under ambient conditions.[39] The kinetic energy of molecules rapidly permits the escape of a molecule to the gas phase from the condensed phase at a given temperature.[39] Equilibrium is reached when the number of molecules exiting the condensed phase equals the number entering the condensed phase. This is known as equilibrium vapor pressure p^0_{vap} and can be determined by the Clausius-Clapeyron equation (1.2) shown below (for vapor-liquid). ΔH_{vap}, T^0_1; T^0_2; $p^0_{vap,1}$; $p^0_{vap,2}$; and R are the molar enthalpy of vaporization, temperature of condition 1 with equilibrium vapor pressure $p^0_{vap,1}$; temperature of condition 2 with equilibrium vapor pressure $p^0_{vap,2}$; and the ideal gas constant, respectively. Condition 1 is usually set at the boiling temperature and pressure whereas condition 2 is the observed vapor pressure at a specified temperature.

$$\ln\left[\frac{p_{vap,2}}{p_{vap,1}}\right]^0 = -\frac{\Delta H_{vap}}{R}\left[\frac{1}{T_2^0} - \frac{1}{T_1^0}\right] \qquad (1.2)$$

The Clausius-Clapeyron equation is derived from Maxwell's relationships[39] and contains some approximations which can lead to slight deviation in calculated equilibrium vapor pressure versus measured equilibrium vapor pressure.[39] The change in molar volume is taken to be

constant as gases typically have molar volumes that are 1,000 times greater than liquid molar volumes. The ideal gas law is used to calculate molar volume, which is a good approximation in typical atmospheric conditions. To simplify integration steps, the temperature dependence of heat capacity is neglected, making enthalpy of vaporization a constant.[39] These approximations are expected to contribute minimally to errors associated in calculated vapor pressure.[39]

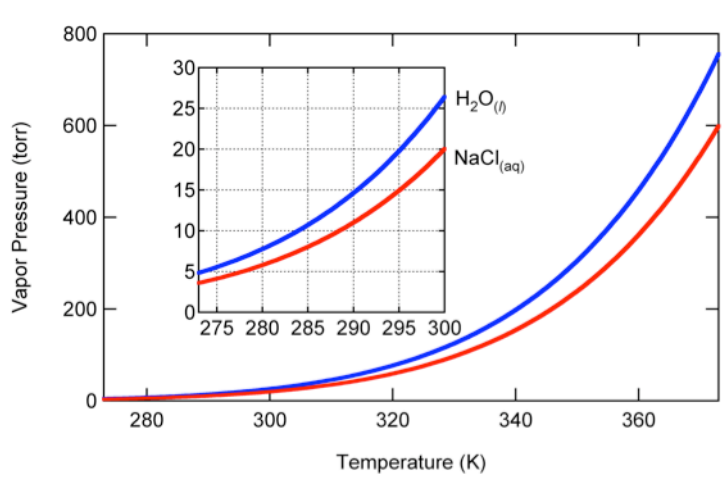

Figure 1.4: Equilibrium vapor pressures of neat liquid water (blue curve) and a saturated NaCl solution (red curve) predicted by the Clausius-Clapeyron equation.

Figure 1.4 is a plot of the Clausius-Clapeyron equation for neat liquid water (blue curve) and a saturated NaCl solution (red curve) with appropriate considerations of boiling point (373 K and 380 K) and enthalpy of vaporization (42.7 kJ mol^{-1} and 43.3 kJ mol^{-1}), respectively.[40] The Clausius-Clapeyron equation predicts a saturated NaCl solution has a lower vapor pressure than neat liquid water, which is always true.[39] This is due to elevation of boiling point and an increase in the molar enthalpy of vaporization, which are entropic effects.[39]

The evaporation of a water molecule from condensed phases is endothermic (with $\Delta H > 0$).[39] Equation 1.3 reflects the Gibbs Free Energy and condition of equilibrium with the enthalpic and entropic, ΔS, relationships outlined above for gas phase water in equilibrium with neat liquid water as well as a saturated NaCl solution.[39]

$$\Delta G = \Delta H - T\Delta S \equiv 0$$
$$\Delta H = T\Delta S \qquad (1.3)$$

A saturated NaCl solution has a larger enthalpy of vaporization, consequently a lower vapor pressure, than neat liquid water. Equation 1.3 thus predicts $\Delta S > 0$ for water evaporating from both $NaCl_{(aq)}$ and $H_2O_{(l)}$, whereas the magnitude of ΔS is larger for the $NaCl_{(aq)}$ situation. An increase in entropy is an increase in disorder, therefore water molecules evaporating from a saturated NaCl solution have an overall larger increase in disorder going to the gas phase than compared to neat liquid water because initially waters are more constrained in the solution. Moreover, liquid water experiences a large entropic cost for incorporating ions into its hydrogen bond network, thus making it a non-ideal solution as solute-solvent interactions are expected to be large.[39] Figure 1.5 is a cartoon depiction of interactions associated with dissolved NaCl in water, which lead to the entropic effects of vapor pressure lowering discussed above.

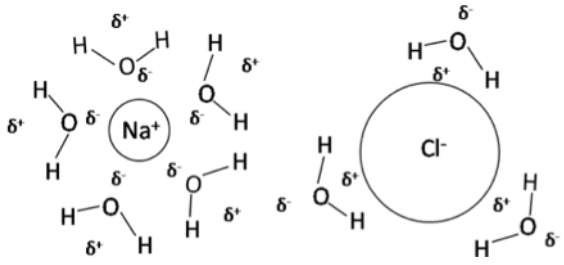

Figure 1.5: A cartoon depiction of NaCl dissolved in water.

The concentration of solutes dissolved will affect the observed vapor pressure of the solution, vapor pressure lowering is a therefore a colligative property.[39] Raoult's Law combined with Dalton's Law, equation 1.4 below, can be used to predict the vapor pressure of a multi-component mixture with knowledge of the vapor pressure of pure components i, p^0_{vap}, and mole fraction χ_i. Solid NaCl does not have an appreciable vapor pressure at room temperature and pressure, thus the vapor pressure expression simplifies to a linear relationship with χ_{H_2O} as the slope.

$$p^0_{vap,aq} = \sum_i \chi_i \cdot p^0_{vap} = \chi_{H_2O} \cdot p^0_{vap,H_2O} \qquad (1.4)$$

Vapor pressures of NaCl solutions ($p^{0}_{vap,aq}$) predicted by equation 1.4 are inaccurate as Raoult's law and Dalton's law only work in the ideal solution regime at infinite dilution.[39]

Activity, a, is often used in association with equilibrium vapor pressure over non-ideal solutions. The formal property of activity is seen in equation 1.5, where g^* is a reference state of any choosing.[39] Replacing g^* with vapor pressure of pure water and re-arrangement leads to equation 1.6, which is defined as water activity, a_w, for bulk liquids.[39]

$$\lim_{g \to g^*} \left[\frac{a}{g}\right] = 1 \qquad (1.5)$$

$$a_w = \frac{p^0{}_{vap,aq}}{p^0_{vap,H_2O}} = \frac{RH}{100} \qquad (1.6)$$

Equation 1.6 shows at the deliquescence point of 75% RH at 295 K,[37] the equilibrium vapor pressure over the dissolved NaCl particle surface will be 15.5 torr. As can be seen in Figure 1.4, this is the vapor pressure over a saturated NaCl solution at 295 K. Thus, the deliquescence point corresponds to equilibrium vapor pressure when solutes are at saturation compositions. The hygroscopic growth curve depicted in Figure 1.2 shows as the ambient RH around the particle surface increases it takes on more water and subsequently becomes more dilute. So as the concentration of dissolved NaCl in solution decreases, the equilibrium vapor pressure over its surface increases.

Water activity as a function of NaCl weight fraction w_t in solution, $a_w(w_t)$, has been determined experimentally for $0 < w_t < 0.45$.[41] Equation 1.7 shows this empirical relationship, which is monotonically increasing activity with decreasing NaCl weight fraction ($C_1 = -6.366 \times 10^{-3}$, $C_2 = 8.624 \times 10^{-5}$, $C_3 = -1.158 \times 10^{-5}$, and $C_4 = 1.518 \times 10^{-7}$).[41] Thus, the vapor pressure over a NaCl solution of any composition can be easily determined by use of equation 1.7 and 1.6.

$$a_w(w_t) = 1.0 + \sum_{i=4} C_i \cdot w_t^i \qquad (1.7)$$

Raoult's Law and empirical formulations of $NaCl_{(aq)}$ activity $a_w(w_t)$ (equation 1.7)[41] are compared in Figure 1.6, which is specified as activity space herein. Raoult's Law is not linear with respect to NaCl weight percent. NaCl has a solubility of 26.5 weight percent in water at 295 K.[40] The marker in Figure 1.6 indicates this composition has an activity of 0.75 as determined by $a_w(w_t)$. Raoult's law is converted from a function of χ_{H2O} to a function of NaCl w_t and predicts a saturated NaCl solution has an activity of 0.90, which is much larger than the measured value of 0.75. The comparison of these two formulations demonstrates concentrated NaCl solutions are real solutions, well out of the ideal solution regime, and this must be considered when exploring thermodynamic properties of concentrated electrolyte solutions. Activity values below 0.75 are representative of a super-saturated NaCl solution. These compositions are kinetically stabilized in particles that have deliquesced, and then subsequently enter an environment of decreased humidity (efflorescence mode growth).

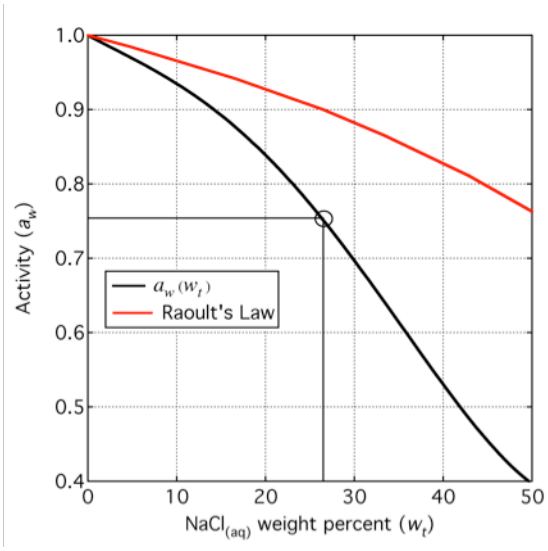

Figure 1.6: Raoult's law compared to empirical determination of $NaCl_{(aq)}$ activity as a function of solute weight percent.

1.2.4 – The Kelvin Effect

The free energy of transition between stable interfaces must be positive;[42] were it negative or zero, nothing would keep materials from completely dispersing into one another. This is known as surface tension, which can be thought of as a free energy per unit area, or even

a force per unit length.[42] Surface tension is the work required to bring a molecule across an interface.

The Clausius-Clapeyron equation (eq. 1.2) above can effectively predict vapor pressure over surfaces that are nominally flat. Surfaces that are curved, such as very small liquid droplets or capillaries, have an effect on the free energy of interface formation. This effect has been described by Young and Laplace as a pressure drop ΔP across a curved interface, seen in equation 1.8.[42] Here σ is surface tension and r is the radius of curvature for the interface in question.

$$\Delta P = \frac{2\sigma}{r} \tag{1.8}$$

The Young and Laplace equation (1.8) demonstrates for planar surfaces the radius of curvature will be infinite and thus $\Delta P = 0$. The effect of a change in pressure at constant temperature on the free energy of a system is shown in equation 1.9.[42]

$$\Delta G = \int V dP \tag{1.9}$$

When molar volume V is taken to be constant and equation 1.8 is used for dP, and assuming that free energy can be related to vapor pressure and behaves as an ideal gas ($G = G^0 + RT\ln P$), equation 1.10 results.[42] This is known as the Kelvin equation, or the Kelvin effect, which predicts an increase in vapor pressure over a curved surface relative to a flat surface for liquids.[42] The ratio P/P^0 is the predicted increase in vapor pressure due to surface curvature, where P^0 is the normal vapor pressure and P is the observed vapor pressure over the curved surface. For water, P/P^0 = 1.001 if r = 1 μm, 1.011 if r = 0.1 μm, and 1.114 if r = 0.01 μm.

$$RT \cdot \ln\left(\frac{P}{P^0}\right) = \frac{2\sigma V}{r} \tag{1.10}$$

The Kelvin effect, $C_K(\sigma, d)$, can be related to water activity, a_w, as in equation 1.6 and is shown in equation 1.11, where radius r has been replaced by diameter d and molar volume V has been replaced by molecular weight M and density ρ.

$$a_w \cdot C_K(\sigma, d) = \frac{RH}{100} = a_w \cdot exp\left(\frac{4M\sigma}{RT\rho d}\right) \qquad (1.11)$$

Another consequence of the Kelvin effect is the empirical activity-solubility relationship (eq. 1.7) discussed previously. The Kelvin effect is applied to equation 1.7 and those results are shown in activity space in Figure 1.7 for d = 5 nm, 20 nm, and 100 nm $NaCl_{(aq)}$ droplets, where a representative surface tension for $NaCl_{(aq)}$ of 80 mN m^{-1} was used for all sizes. Figure 1.7 demonstrates that for 100 nm droplets there is a difference in activity-solubility compared to a bulk liquid; however, for droplets smaller than 20 nm there is a much greater effect on activity-solubility relationships. Consequently, when droplets smaller than 20 nm deliquesce their aqueous composition will be much different than the composition of a bulk saturated solution.

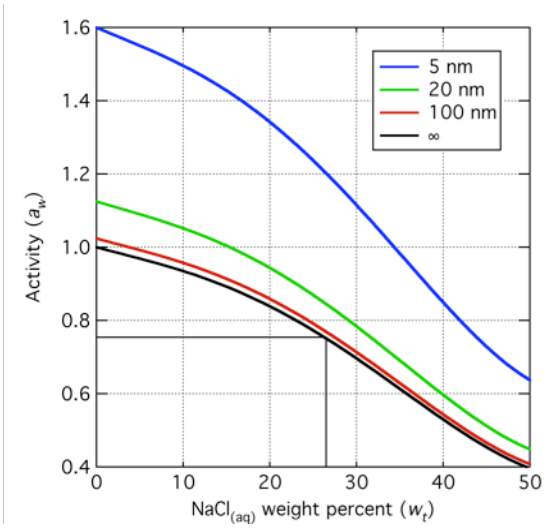

Figure 1.7: Activity-solubility relationships of a $NaCl_{(aq)}$ solution (∞) and the Kelvin effect for 5 nm, 20 nm, and 100 nm droplets.

Section 1.3 – *Hygroscopic Growth of NaCl Aerosols*

1.3.1 – NaCl as a Model for Sea Salt Aerosol

Field measurements have shown sea-salt comprises over 80% by mass for open ocean and marine based aerosol.[30] NaCl is a model system for sea-salt aerosols; however, $MgCl_2$ is also an important component of sea-salt aerosol.[43] Marine and open ocean aerosols are generated through wave action and are typically 1-4 μm in diameter.[4] As marine and open ocean aerosols are transported inland to regions of lower RH than compared to over the ocean, they can effloresce.[43] Subsequently, they can also take up water again and deliquesce in regions of higher humidity. Understanding the transport of aerosols in the atmosphere is thus important as hysteresis in hygroscopic growth occurs over RH ranges expected in the lower atmosphere (i.e. 45-75% RH). NaCl aerosols have also been shown to participate in chemistry of the lower atmosphere.[4,43,44] NaCl aerosols can be chemically aged through uptake and reaction of oxides of nitrogen[45] and nitric acid,[46] reaction with hydroxyl radical,[47] or even uptake of sulfuric acid,[48] all of which can liberate reactive gases in the atmosphere such as $HCl_{(g)}$, $Cl_{2(g)}$,[47,49] $ClNO_{2(g)}$,[49] and $ClNO_{(g)}$.[4,43]

Solid NaCl has a highly ordered crystalline structure, which is face centered cubic. In NaCl each Na^+ is surrounded by 6 Cl^- neighbors and each Cl^- is surrounded by 6 Na^+ neighbors. Thus, the top view of a smooth NaCl crystal would yield an equal number of Na^+ cations and Cl^- anions. By the Miller Index system, this crystal plane is called the (100) face and is electrically neutral. This is the bulk crystalline termination plane for most NaCl crystal structures at room temperature and pressure.[43] The surface density of ion pairs for the NaCl (100) face (S_{NaCl}) is 6.4×10^{14} cm^{-2}.[50] Another crystal plane of NaCl is the (111) face, which is either all Na^+ or all Cl^- when viewed from above. This crystal plane is not electrically neutral and often surface defects of this nature are found on NaCl surfaces.[43] Surface defects which are electrostatic in nature

can bias molecular scale uptake of gaseous compounds and this is typically where initial adsorption of water on NaCl occurs.[43]

1.3.2 – Adsorption of Thin Water Films on NaCl Surfaces

Thin water films are ubiquitous on many common surfaces, including atmospheric particles, under ambient conditions.[51] In many instances, these thin films are responsible for macroscopic observations, even though they may only constitute a very small fraction of the system's total mass or volume. Previous measurements on bulk crystalline NaCl showed that above 70% RH, NaCl acquires 3.5-4.0 monolayers (ML) of water.[43,44,51] As the RH above the NaCl surface increases, the film becomes thick enough to dissolve NaCl[51] at the deliquescence point.

Water coverage layer, Θ_w, is typically used to quantify the number of ML of water adsorbed on a surface below the DRH. The definition of a coverage layer for water on NaCl is seen in equation 1.12,[51] where S_w is the surface density of water, typically quantified from measurement, and S_{NaCl} is the surface density of ion pairs for the (100) face.

$$\Theta_w(S) = \frac{S_w}{S_{NaCl}} \qquad (1.12)$$

The structure of water on a bulk NaCl (100) surface was previously investigated by Fourier transform infrared (FTIR) spectroscopy.[51] Researchers concluded that for $\Theta_w \leq 0.5$ water molecules aggregate into islands or clusters on the surface held together by hydrogen bonds and electrostatic surface attraction; at $0.5 \leq \Theta_w \leq 2.5$ a transition region occurs with islands and a multilayer thin film; at $2.5 \leq \Theta_w \leq 3.5$ a multilayer film with properties similar to bulk liquid water exists; and finally, the range $\Theta_w \geq 3.5$ has been called the pre-solution region.[51] Equating water density to 33 molecules nm^{-3} (997.1 kg m^{-3}) is therefore appropriate only at sufficiently large coverage. As water adopts on an ice-like structure at low coverage levels, a more appropriate density in the low coverage regime should be somewhere between 30-33 nm^{-3}.

The physical adsorption of gases by solids is theoretically described by a variety of adsorption isotherms. As with many theoretical treatments, there are assumptions and approximations made which may or may not be physically accurate and can give rise to deviations in agreement with experimental data.

Brunauer-Emmett-Teller (BET): The BET isotherm has been used extensively to describe multilayer adsorption of gases by solids.[42,51,52] It is an expansion of Langmuir single-layer adsorption to a multilayer adsorption. In the BET isotherm there are three assumptions: (1) in all layers except the first one, the interaction potential is equal to the molar heat of adsorption q_L, (2) in all layers except the first, vibrational frequencies υ_L and evaporation-condensation coefficients a_L are identical (i.e. $\upsilon_2 = \upsilon_3 = \ldots = \upsilon_L$), and (3) when $P = p^0_{vap}$ the adsorbate condenses on the surface with properties of a bulk liquid.[42,52] Similarly to the Langmuir isotherm, lateral interactions are not taken into consideration in the BET isotherm.

$$\Theta_w(S) = \frac{c \cdot S}{(1-S)\cdot(1-S+c\cdot S)} \tag{1.13}$$

$$S = \frac{RH}{100 \cdot C_K(\sigma, d)} \tag{1.14}$$

$$c = m\,exp\left(\frac{q_1 - q_L}{RT}\right) = \frac{a_1 \upsilon_L}{a_L \upsilon_1} exp\left(\frac{q_1 - q_L}{RT}\right) \tag{1.15}$$

Equation 1.13 is the functional form of the BET isotherm with a Kelvin effect correction term $C_K(\sigma,d)$ for saturation ratio S (equation 1.14), which should be used for highly curved surfaces. Equation 1.15 shows the BET constant c in detail. The pre-exponential factor m is typically taken to be unity; however, a range of m values between 10^{-5}–10 are fairly realistic.[52] Heat of adsorption values for a multilayer of water on bulk NaCl have been quantified from FTIR spectroscopy measurements.[51] A representative value for the BET constant c for water on NaCl is 1.5, corresponding to a positive ~1 kJ mol^{-1} difference in heat of adsorption values between

the first layer (q_1) and multilayer (q_L).[51] Heat of adsorption values are negative, thus condensation to the multilayer is more exothermic than condensation to the first layer.

Certain approximations can be made to take lateral interactions into account.[42] Using Adamson's (1997)[42] derivation of lateral interactions for the Langmuir isotherm, which shows only the Langmuir constant is affected from lateral interaction considerations,[42] it can be shown only the BET constant c is affected by lateral interactions, not the mathematical form of the isotherm itself. Thus, caution should be used when reporting heat of adsorption values from BET isotherm analysis when lateral interactions are expected to be large.

Frenkel-Halsey-Hill (FHH): A different approach to multilayer adsorption is described by the FHH isotherm, which is based on derivation from potential field theory. A potential field (U) at the adsorbent surface decays by distance r^{-B} from the surface (i.e. $U = U_0/r^B RT$). Adsorbate molecules can be viewed as "falling" into a potential well as they get closer to the surface.[42] A key assumption of the FHH isotherm is the principle interaction between adsorbate and adsorbent is of the dispersive type. The use of B = 3 is therefore appropriate;[42] however, it is more common to treat B as an empirical parameter and a wide range of values have been reported.[42]

$$\ln(S) = \frac{A}{\Theta_w^B(S)} \tag{1.16}$$

$$A = \frac{U_0}{r^B RT} \tag{1.17}$$

The FHH isotherm is seen in equation 1.16 and contains a Kelvin effect correction term for saturation ratio as in the BET isotherm for sufficiently curved surfaces. The parameter A in equation 1.17 is dependant upon which interaction type exists between adsorbate and adsorbent as described above. A value of 0.96 has been used for A to describe water on NaCl[42,52,53] and values of 0.5-1 have been used for B.[42,52,53]

1.3.3 – Hygroscopic Growth of NaCl Aerosol, Sub-Saturation Köhler Theory Considerations

Mobility growth factors of particles in an aqueous phase at a certain RH can be predicted with knowledge of activity-solubility relationships presented above in section 1.2. The following is a derivation of Köhler theory, which has been used to predict hygroscopic growth of NaCl aerosol.[54,55] The mass of a soluble solid (m_S) should be equal to the mass of a corresponding solution made from that solid multiplied by its respective weight fraction ($w_t/100$) in solution (equation 1.18).[39]

$$m_S = \rho_S \cdot V_S = \frac{w_t}{100} \rho_{aq} \cdot V_{aq} \qquad (1.18)$$

Using the approximation that each particle (dry and wet) are spherical, and considering the definition of growth factor in equation 1.1, equation 1.18 rearranges to Köhler theory seen in equation 1.19.[54] Here, the density of the solid ρ_S is constant (2165 kg m^{-3} for NaCl); however, weight fraction as a function of activity $w_t(a_w)$ and density as a function of weight fraction $\rho_{aq}(w_t(a_w))$ (which depends on activity as well) for the solution are needed to predict growth factors for any value of RH, vapor pressure, or activity.

$$GF_m = \left(\frac{100\rho_s}{w_t(a_w) \cdot \rho_{aq}(w_t(a_w))} \right)^{1/3} \qquad (1.19)$$

Rearrangement of equation 1.7 is adequate for $w_t(a_w)$ and $\rho_{aq}(w_t(a_w))$ has also been determined empirically for $NaCl_{(aq)}$ $0 < w_t < 45\%$.[41] Using equations 1.6 and 1.7 with 1.19 will describe growth factors for large droplets (> 100 nm). Figure 1.8 shows the hygroscopic growth curve for large NaCl particles, where the solid vertical lines indicate the DRH (75% RH)[37] and ERH (45% RH)[38] values.

Upon exposure to increasing RH, NaCl particles take up a few ML of water (1). At 75% RH they deliquesce (2), then take up water and grow substantially (3) as predicted by Köhler theory. As the droplets enter a lower humidity environment, they lose water and shrink (4) as predicted by Köhler theory. At 45% RH they re-crystallize (5). Measurements have confirmed these predicted growth factors by Köhler theory for large NaCl particles at room temperature and pressure.[37,41]

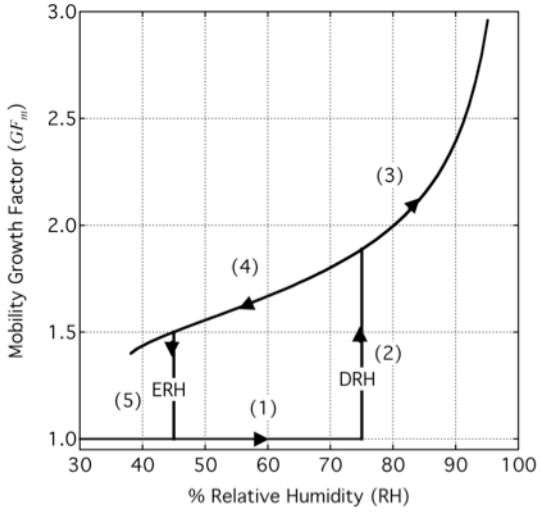

Figure 1.8: Hygroscopic growth curve for large NaCl particles calculated from eq. 1.19

Using equations 1.11 and 1.7 with 1.19 will describe growth factors for nanometer sized droplets (< 100 nm).[55] Surface tension terms in the Kelvin effect also depend on NaCl weight fraction in solution. Empirical formulations of $\sigma_{aq}(w_t(a_w))$ have been determined for $NaCl_{(aq)}$ $0 < w_t < 45\%$.[56] Figure 1.9 is a plot of equation 1.19 for NaCl particles, with Kelvin effect considerations for a 5 nm, 20 nm, and 100 nm particle compared to a large particle (∞). As can be seen in Figure 1.9, mobility growth factors are predicted to be much smaller for a given RH as a consequence of the Kelvin effect, which has also been confirmed by measurements.[55]

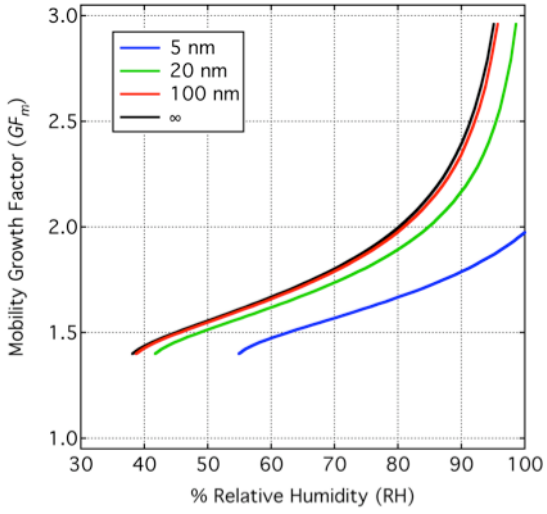

Figure 1.9: Hygroscopic growth curves predicted by Köhler theory for large particles (∞) compared to 5 nm, 20 nm, and 100 nm particle.

Section 1.4 – *Hygroscopic Growth of Mixed Organic-Inorganic Particles*

1.4.1 – Mixed Organic-Inorganic Aerosols in the Atmosphere

Field measurements have shown aerosols represent complex mixtures of soluble inorganic materials, water-soluble organic materials (WSOM), water-insoluble organic materials (WIOM), and organic, or non sea-salt, sulfates.[30] The sub-micron sizes of aerosol have a larger fraction of organic material than micron sizes of aerosol.[30] Many investigators confirm organics can interfere with hygroscopic behavior of soluble inorganic aerosols.[9,32,57-61]

1.4.2 – Previous Measurements of Mixed Organic-Inorganic Aerosols

Several groups have studied the effects of organic material on hygroscopic properties of inorganic particles, which are believed to have inorganic core-organic shell morphology.[9,32,57-62] The organic material did not inhibit growth of the soluble inorganic core, even for cases when the organic material comprised the majority of the particle mass.[32,57] GF_m could be predicted by use of the Zdanovskii-Stokes-Robinson (ZSR) model, which assumes particle constituents adsorb water independently and GF_m can be predicted by volume weighting of individual GF_m for each respective component.[9,58] The soluble inorganic core is therefore expected to contribute solely to hygroscopic growth of mixed organic-inorganic particles because pure amphiphilic organic particles are not expected to take up any measurable amount of water at humidities between 5-95% RH.[62] In one particular study on 100 nm mixed NaCl particles, the deliquescence point shifted to lower RH values, by approximately 4% RH, compared to pure NaCl when surface active materials (glutaric and pyruvic acid) were a major component.[61] Hygroscopic growth of 70-100 nm sodium dodecyl sulfate (SDS)/NaCl particles have been examined, which showed at a weight percent corresponding to roughly one coverage layer of SDS, deliquescence was shifted to lower values by only 1% RH.[59]

1.4.3 – Hygroscopic Growth of Mixed Systems

The solubility of components in a multi-component mixture is expected to be altered significantly when solute-solute and solute-solvent interactions are strong.[39] Recall vapor pressure lowering is a colligative property, therefore as the amount of dissolved material increases in solution equilibrium vapor pressure is decreased. The composition that minimizes equilibrium vapor pressure, or activity, is known as the eutonic point, or eutonic composition.[41] The eutonic composition of two components represents their maximum miscibility, therefore components which are highly miscible with each other have highly suppressed activities. For example, the eutonic point of NaCl and $NaNO_3$ occurs at an activity of 0.69 and $\chi_{NaCl} = 0.40$,[35,62] whereas the eutonic point of NaCl and Na_2SO_4 occurs at an activity of 0.74 and $\chi_{NaCl} = 0.60$.[41,62] Therefore NaCl is more miscible with $NaNO_3$ in solution than with Na_2SO_4. Multi-component particles which have a eutonic composition display mutual deliquescence at the eutonic activity.[41]

The miscibility and activity of SDS and NaCl in adsorbed films, aggregates and bulk solutions has been studied experimentally.[62,63] Researchers find at high total molalities > 2 mol kg^{-1} the surface tension of SDS/NaCl aqueous mixtures is independent of SDS mole fraction[63] and has a constant value between 30-35 mN m^{-1}.[63] NaCl reduces the critical micelle concentration (CMC) of SDS in solution, thereby enhancing free SDS monomers at the interface (when SDS concentration is above the CMC) and leading to the nearly constant surface tension value, even at very small SDS mole fractions.[63] Consequently, NaCl and SDS are not miscible with each other as demonstrated by the measured eutonic activity of 0.75 at $\chi_{NaCl} = 0.92$[64] and the measured mutual deliquescence point of 75% RH for SDS/NaCl particles at $\chi_{NaCl} = 0.99$.[59]

1.4.4 – The Zdanoviskii-Stokes-Robinson (ZSR) Model

One approach for modeling hygroscopic growth of mixed organic-inorganic particles is the ZSR model. In the ZSR model, the hygroscopic growth of a multi-component system is estimated from the known GF_m values of its pure components and their volume fractions.[9,65-67] The ZSR model assumes that there are no interactions among the different mixture components; therefore, the hygroscopic growth of the internally mixed particles is an appropriately weighed sum of the hygroscopic growth factors of its components.[68] It also assumes an ideal mixing behavior with spherical particles having a shape factor of unity. For poorly miscible species, such as NaCl and SDS, an ideal mixing behavior is a good assumption as NaCl and SDS are expected to segregate in the particle and not interact with each other.

The ZSR model is shown in equation 1.20, where ε_1 is the volume fraction of a soluble inorganic component and ε_2 is the volume fraction of a weakly soluble organic component. In the limit of a completely insoluble organic inclusion, the ZSR model reduces to equation 1.21 and thus the soluble inorganic component contributes entirely to hygroscopic growth of the mixed particle.

$$GF_{particle}^3 = \varepsilon_1 GF_1^3 + \varepsilon_2 GF_2^3 \quad (1.20)$$

$$GF_{particle}^3 \approx 1 + \varepsilon_1 \left(GF_1^3 - 1 \right) \quad (1.21)$$

1.4.5 – The Role of Organic Materials in Köhler Theory of Mixed Inorganic-Organic Particles

A theoretically rigorous approach for modeling the effect of surfactants on hygroscopic growth of mixed organic-inorganic particles is a modified version of Köhler theory, which has been examined by several groups.[13,20,69,70] When surfactant partitioning to the droplet surface was considered, results showed slightly soluble organic compounds dissolve at an earlier stage of droplet growth.[70] Consequently, critical supersaturation values for CCN-activity can be underestimated if surfactant partitioning is neglected.[70] Researchers also concluded surfactants

will not only affect solubility-activity relationships, but will also affect the Kelvin equation terms in Köhler theory.[70]

Lowering of surface tension due to the presence of surfactants will reduce the magnitude of the Kelvin effect as depicted in Figure 1.10, which shows the same Köhler curves plotted in Figure 1.9 for 5 nm, 20 nm, and large (∞) droplets with two considerations of surface tension for 5 nm and 20 nm droplets. Solid lines for 5 nm and 20 nm droplets have a surface tension represented by empirical formulations of NaCl weight percent $\sigma_{aq}(w_t(a_w))$ (roughly 82 mN m^{-1} at saturation)[56] whereas dotted lines have a constant surface tension of 30 mN m^{-1}. As can be seen in Figure 1.10, even without considering surfactant effects on solubility-activity relationships, the surface tension effect by surfactants on the Kelvin effect increases GF_m for nanoparticles. Thus, hygroscopic growth measurements for surfactant/NaCl nanoparticles are desirable to elucidate how solubility-activity relationships are affected in the nanometer size regime.

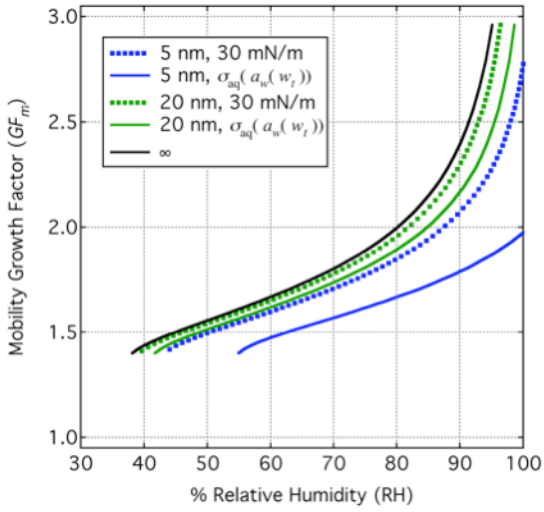

Figure 1.10: Hygroscopic growth curves predicted by Köhler theory for large particles (∞) compared to 5 nm and 20 nm with considerations of surface tensions.

Section 1.5 – *Hygroscopic Growth of Inorganic Nanoparticles*

1.5.1 – Previous Measurements and Nano-size Effects on Deliquescence and Hygroscopic Growth

Only a few experimental and theoretical studies of hygroscopic growth of nanoparticles are currently available. Hämeri et al.[53,71,72] were the first to measure GF_m for 8-60 nm NaCl and $(NH_4)_2SO_4$ particles. They found that GF_m increases with increasing particle size, consistent with predictions of the Kelvin effect, and that the DRH for NaCl particles in this size range is higher than DRH for larger particles.[37] They also observed "non-prompt" (occurring over a range of RH) deliquescence, a concept first described in a theoretical study of deliquescence of small particles by Mirabel.[73] A modeling study by Russell and Ming[74] expanded on Mirabel's work and showed that the observed sign and magnitude of the DRH shift in small NaCl particles is consistent with deliquescence of NaCl nanoparticles pre-coated with a thin layer of water (as opposed to completely dry particles below DRH assumed by Mirabel et al.[73]

More recent measurements by Biskos et al.[55,75,76] challenged the non-promptness of the deliquescence, and showed that it can be attributed to the experimental artifacts in the operation of the tandem differential mobility analyzer used for these measurements. Contrary to the previous theoretical predictions,[73,74] they could only observe the nano-size effect on DRH for NaCl particles but not for $(NH_4)_2SO_4$ particles. Gao et al.[38] modeled the efflorescence of NaCl nanoparticles by combining the Köhler equation with homogeneous nucleation theory, and correctly predicted the increase in ERH values for smaller particle sizes observed by Biskos et al.[75]

As the particle size approaches molecular dimensions, the macroscopic description of phase transitions should become less meaningful. However, even for the smallest 6 nm particles of NaCl and $(NH_4)_2SO_4$ studied in Refs. 55, 71, 72, 75, and 76, the GF_m values observed

above DRH could still be accurately predicted using thermodynamic[71,72,75,76] parameters appropriate for bulk samples after accounting for particle shape effects.[55,76] The observed particle size dependence of the DRH could also be modeled using standard thermodynamics approaches (Köhler Theory) without having to resort to a molecular level description of the phase transitions.[74] It was possible to use a macroscopic description for the theoretical prediction of phase transitions in even smaller particles (down to 2 nm in size) by allowing for phenomenological size dependence of the surface tension.[77,78]

1.5.2 – Gibbs Equilibrium for a Phase Transition Revisited

Although nanoparticles (< 20 nm) are generally too small to activate cloud droplets, their hygroscopic properties are interesting for a number of fundamentally important reasons. In this size range, there is a non-trivial contribution of the surface energy to the constant temperature, constant pressure free energy expression of the particle:

$$G_{particle} = \sum_{i,j}\left(\mu_{i,j} n_{i,j} + \sigma_{i,j} A_{i,j}\right) \qquad (1.22)$$

where $G_{particle}$, μ, n, σ, and A stand for particle free energy (either wet or dry), chemical potential, molar amount, surface tension, and particle surface area, respectively, of each component i in phase j. In other words, the surface tension term in the free energy expression, which can be safely neglected for particles larger than 100 nm, starts to be comparable in magnitude to NaCl bulk chemical potential.[73,74]

Expanding on Gibbs equilibrium for a phase transition discussed in section 1.2, deliquescence is reached when the condition outlined in equation 1.23 is satisfied. Here G_{dry} and G_{wet} are the free energy expressions (equation 1.22) for each particle phase and when their free energies are equal, deliquescence will occur.

$$\Delta G_{deliq} = G_{dry} - G_{wet} \equiv 0 \qquad (1.23)$$

Figure 1.11 is an illustration of the nano-size effect on deliquescence from Gibbs condition of phase equilibria. In Figure 1.11, solid lines are stable phases, dashed lines are meta-stable phases, dotted lines are unstable phases, the black lines are free energy expressions for 100 nm NaCl particles, and the blue lines are free energy expressions for 14 nm NaCl particles. Deliquescence occurs at 75% RH for 100 nm NaCl particles because the free energy expression for the crystalline phase crosses the free energy expression for the aqueous phase. Above 75% RH, the crystalline phase is unstable and the aqueous phase is stable. Below 75% RH, the aqueous phase is meta-stable due to kinetic constraint. Non-trivial contributions ($\sigma_{I,j}A_{i,j}$) to free energy expressions are represented by $\delta_{wetted}(d_m)$ for the crystalline phase wetted with a thin film (3-4 ML) of water and by $\delta_{deliq}(d_m)$ for the aqueous phase. These contributions scale the free energy of deliquescence such that more RH above the dry particle surface is required to dissolve it, which occurs at 79% RH for 14 nm NaCl particles.[73-75]

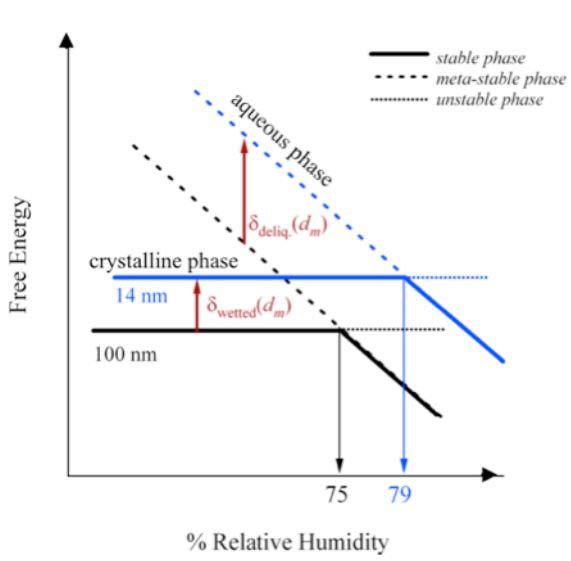

Figure 1.11: An illustration of the nano-size effect on deliquescence from Gibbs condition for phase equilibria.

Section 1.6 – *Goals and Motivations*

The goal of this research is to explore hygroscopic properties of NaCl nanoparticles coated with a model surfactant. Previous research in this laboratory[62] on 9 and 17 nm particles containing AOT and NaCl showed peculiar hygroscopic growth curves, which could not be explained. Deliquescence points were shifted to much lower values of humidity (up to 10% RH) than compared to studies with larger (> 70 nm) surfactant/NaCl nanoparticles. Mobility growth

factors were greatly suppressed, more so than would be expected when assuming the nanoparticles' composition is that of the solution from which they were generated. The ZSR model could be used to explain post-deliquescence growth of AOT/NaCl nanoparticles, but only when the composition was assumed to be enhanced in AOT. Further experimentation is needed to elucidate these peculiar results, which could provide a fundamental look at interactions pertinent to Earth's atmosphere that are poorly understood.

The surfactant SDS is chosen as a model single chain amphiphile to mix with NaCl nanoparticles. Greater detail in hygroscopic growth curves is also desired to explore the nature of the nanoparticles surface prior to deliquescence. For example, using our employed techniques described in Chapter 2, ML coverage of water on nanoparticles is quantifiable. Standard adsorption isotherms will be used to quantify the nature of these adsorbate-adsorbent interactions. A variety of Köhler theory treatments will also be applied to nanoparticle hygroscopic growth curves to explain the peculiar growth that Alshawa et al.[62] observed. Lastly, the composition of nanoparticles generated with techniques used is unknown; therefore an effective impactor for particles smaller than 50 nm is needed to collect nanoparticles on any substrate for chemical and morphological analysis. The main questions to answer are, (1) can a variety of theoretical and experimental techniques be employed to explore the effect of surfactant on hygroscopic growth of NaCl nanoparticles? (2) Are nanoparticles unique in their hygroscopic properties? (3) Or can their behavior be predicted by simple extrapolation of bulk properties?

References

(1) Gleick, P. H., U. S. G. S. Water Resources (http://water.usgs.gov/), 1996.
(2) Solomon, S.; Qin, D.; Manning, M.; Chen, Z.; Marquis, M.; Averyt, K. B.; Tignor, M.; Miller, H. L. "Climate Change 2007: The Physical Science Basis. Contribution of Working Group I to the Fourth Assessment Report of the Intergovernmental Panel on Climate Change.," IPCC, 2007.
(3) Shaw, G. E.; Slinn, W. G. N., **"Climate Cooled by Particles and Clouds"**. *Atmospheric Environment Part a-General Topics* **1992**, *26*, 522.
(4) Finlayson-Pitts, B. J.; Pitts, J. N., *Chemistry of the Upper and Lower Atmosphere: Theory, Experiments, and Applications*; Academic Press: San Diego, **2000**.
(5) NASA. Earth Observatory (http://earthobservatory.nasa.gov/IOTD/view.php?id=5484), 2009.
(6) Myhre, G., **"Consistency Between Satellite-Derived and Modeled Estimates of the Direct Aerosol Effect"**. *Science* **2009**, *325*, 187.
(7) Petters, M. D.; Prenni, A. J.; Kreidenweis, S. M.; DeMott, P. J.; Matsunaga, A.; Lim, Y. B.; Ziemann, P. J., **"Chemical Aging and the Hydrophobic-to-Hydrophilic Conversion of Carbonaceous Aerosol"**. *Geophysical Research Letters* **2006**, *33*, L24806.
(8) Broekhuizen, K.; Kumar, P. P.; Abbatt, J. P. D., **"Partially Soluble Organics as Cloud Condensation Nuclei: Role of Trace Soluble and Surface Active Species"**. *Geophysical Research Letters* **2004**, *31*, L01107.
(9) Svenningsson, B.; Rissler, J.; Swietlicki, E.; Mircea, M.; Bilde, M.; Facchini, M. C.; Decesari, S.; Fuzzi, S.; Zhou, J.; Moenster, J.; Rosenoern, T., **"Hygroscopic Growth and Critical Supersaturations for Mixed Aerosol Particles of Inorganic and Organic Compounds of Atmospheric Relevance"**. *Atmospheric Chemistry and Physics* **2006**, *6*, 1937.
(10) Rogers, C. F.; Hudson, J. G.; Hallett, J.; Penner, J. E., **"Cloud Droplet Nucleation by Crude Oil Smoke and Coagulated Crude Oil/Wood Smoke Particles"**. *Atmospheric Environment, Part A: General Topics* **1991**, *25A*, 2571.
(11) Novakov, T.; Penner, J. E., **"Large Contribution of Organic Aerosols to Cloud-Condensation-Nuclei Concentrations"**. *Nature* **1993**, *365*, 823.
(12) Novakov, T.; Corrigan, C. E., **"Cloud Condensation Nucleus Activity of the Organic Component of Biomass Smoke Particles"**. *Geophysical Research Letters* **1996**, *23*, 2141.
(13) Cruz, C. N.; Pandis, S. N., **"A Study of the Ability of Pure Secondary Organic Aerosol to Act as Cloud Condensation Nuclei"**. *Atmospheric Environment* **1997**, *31*, 2205.
(14) Cruz, C. N.; Pandis, S. N., **"The Effect of Organic Coatings on the Cloud Condensation Nuclei Activation of Inorganic Atmospheric Aerosol"**. *Journal of Geophysical Research* **1998**, *103*, 13111.
(15) Corrigan, C. E.; Novakov, T., **"Cloud Condensation Nucleus Activity of Organic Compounds: A Laboratory Study"**. *Atmospheric Environment* **1999**, *33*, 2661.
(16) Hegg, D. A.; Gao, S.; Hoppel, W.; Frick, G.; Caffrey, P.; Leaitch, W. R.; Shantz, N.; Ambrusko, J.; Albrechcinski, T., **"Laboratory Studies of the Efficiency of Selected Organic Aerosols as CCN"**. *Atmospheric Research* **2001**, *58*, 155.
(17) Mircea, M.; Facchini, M. C.; Decesari, S.; Fuzzi, S.; Charlson, R. J., **"The Influence of the Organic Aerosol Component on CCN Supersaturation Spectra for Different Aerosol Types"**. *Tellus, Series B: Chemical and Physical Meteorology* **2002**, *54B*, 74.
(18) Raymond, T. M.; Pandis, S. N., **"Cloud Activation of Single-Component Organic Aerosol Particles"**. *Journal of Geophysical Research* **2002**, *107*, 4787.
(19) Abbatt, J. P. D.; Broekhuizen, K.; Pradeep Kumar, P., **"Cloud Condensation Nucleus Activity of Internally Mixed Ammonium Sulfate/Organic Acid Aerosol Particles"**. *Atmospheric Environment* **2005**, *39*, 4767.
(20) Kumar, P. P.; Broekhuizen, K.; Abbatt, J. P. D., **"Organic Acids as Cloud Condensation Nuclei: Laboratory Studies of Highly Soluble and Insoluble Species"**. *Atmospheric Chemistry and Physics* **2003**, *3*, 509.
(21) van Reken, T. M.; Ng, N. L.; Flagan, R. C.; Seinfeld, J. H., **"Cloud Condensation Nucleus Activation Properties of Biogenic Secondary Organic Aerosol"**. *Journal of Geophysical Research* **2005**, *110*, D07206.

(22) Huff Hartz, K. E.; Tischuk, J. E.; Chan, M. N.; Chan, C. K.; Donahue, N. M.; Pandis, S. N., **"Cloud Condensation Nuclei Activation of Limited Solubility Organic Aerosol"**. *Atmospheric Environment* **2006**, *40*, 605.
(23) Lohmann, U.; Broekhuizen, K.; Leaitch, R.; Shantz, N.; Abbatt, J., **"How Efficient is Cloud Droplet Formation of Organic Aerosols?"**. *Geophysical Research Letters* **2004**, *31*, L05108.
(24) Petters, M. D.; Kreidenweis, S. M.; Snider, J. R.; Koehler, K. A.; Wang, Q.; Prenni, A. J.; Demott, P. J., **"Cloud Droplet Activation of Polymerized Organic Aerosol"**. *Tellus, Series B: Chemical and Physical Meteorology* **2006**, *58B*, 196.
(25) Sun, J.; Ariya, P. A., **"Atmospheric Organic and Bio-Aerosols as Cloud Condensation Nuclei (CCN): A Review"**. *Atmospheric Environment* **2006**, *40*, 795.
(26) Kanakidou, M.; Seinfeld, J. H.; Pandis, S. N.; Barnes, I.; Dentener, F. J.; Facchini, M. C.; Van Dingenen, R.; Ervens, B.; Nenes, A.; Nielsen, C. J.; Swietlicki, E.; Putaud, J. P.; Balkanski, Y.; Fuzzi, S.; Horth, J.; Moortgat, G. K.; Winterhalter, R.; Myhre, C. E. L.; Tsigaridis, K.; Vignati, E.; Stephanou, E. G.; Wilson, J., **"Organic Aerosol and Global Climate Modelling: A Review"**. *Atmospheric Chemistry and Physics* **2005**, *5*, 1053.
(27) Ellison, G. B.; Tuck, A. F.; Vaida, V., **"Atmospheric Processing of Organic Aerosols"**. *J. Geophys. Res. D* **1999**, *104*, 11633.
(28) Broekhuizen, K. E.; Thornberry, T.; Kumar, P. P.; Abbatt, J. P. D., **"Formation of Cloud Condensation Nuclei by Oxidative Processing: Unsaturated Fatty Acids"**. *Journal of Geophysical Research* **2004**, *109*, D24206.
(29) Rudich, Y.; Donahue, N. M.; Mentel, T. F., **"Aging of Organic Aerosol: Bridging the Gap between Laboratory and Field Studies"**. *Annual Review of Physical Chemistry* **2007**, *58*, 321.
(30) Rinaldi, M.; Facchini, M. C.; Decesari, S.; Carbone, C.; Finessi, E.; Mircea, M.; Fuzzi, S.; Ceburnis, D.; M., E.; Kulmala, M.; de Leeuw, G.; O'Dowd, C. D., **"Coastal and Open Ocean Aerosol Characterisitics: Investigating the Representativeness of Coastal Aerosol Sampling over the North-East Atlantic Ocean"**. *Atmospheric Chemistry and Physics Discussions,* **2008**, *8*, 19035.
(31) Martin, S. T., **"Phase Transitions of Aqueous Atmospheric Particles"**. *Chemical Reviews* **2000**, *100*, 3403.
(32) Cruz, C. N.; Pandis, S. N., **"Deliquescence and Hygroscopic Growth of Mixed Inorganic-Organic Atmospheric Aerosol"**. *Environmental Science and Technology* **2000**, *34*, 4313.
(33) Cziczo, D. J.; Abbatt, J. P. D., **"Infrared Observations of the Response of NaCl, $MgCl_2$, NH_4HSO_4, and NH_4NO_3 Aerosols to Changes in Relative Humidity from 298 to 238 K"**. *Journal of Physical Chemistry A* **2000**, *104*, 2038.
(34) Braban, C. F.; Carroll, M. F.; Styler, S. A.; Abbatt, J. P. D., **"Phase Transitions of Malonic and Oxalic Acid Aerosols"**. *Journal of Physical Chemistry A* **2003**, *107*, 6594.
(35) Ge, Z.; Wexler, A. S.; Johnston, M. V., **"Deliquescence Behavior of Multicomponent Aerosols"**. *Journal of Physical Chemistry A* **1998**, *102*, 173.
(36) Liu, Y.; Yang, Z.; Desyaterik, Y.; Gassman, P. L.; Wang, H.; Laskin, A., **"Hygroscopic Behavior of Substrate-Deposited Particles Studied by micro-FT-IR Spectroscopy and Complementary Methods of Particle Analysis"**. *Analytical Chemistry* **2008**, *80*, 633.
(37) Tang, I. N.; Munkelwitz, H. R., **"Composition and Temperature Dependence of the Deliquescence Properties of Hygroscopic Aerosols"**. *Atmospheric Environment, Part A: General Topics* **1993**, *27A*, 467.
(38) Gao, Y.; Yu, L. E.; Chen, S. B., **"Theoretical Investigation of Substrate Effect on Deliquescence Relative Humidity of NaCl Particles"**. *Journal of Physical Chemistry A* **2007**, *111*, 633.
(39) Raff, L. M., *Principles of Physical Chemistry*; Prentice Hall: Upper Saddle River, NJ, **2001**.
(40) Carper, J., **"The CRC Handbook of Chemistry and Physics"**. *Library Journal* **1999**, *124*, 192.
(41) Tang, I. N.; Tridico, A. C.; Fung, K. H., **"Thermodynamic and Optical Properties of Sea Salt Aerosols"**. *Journal of Geophysical Research-Atmospheres* **1997**, *102*, 23269.
(42) Adamson, A. W.; Gast, A. P., *Physical Chemistry of Surfaces*; John Wiley & Sons, **1997**; Vol. 6th.
(43) Hemminger, J. C., **"Heterogeneous Chemistry in the Troposphere: A Modern Surface Chemistry Approach to the Study of Fundamental Processes"**. *International Review of Physical Chemistry* **1999**, *18*, 387.

(44) Finlayson-Pitts, B. J.; Hemminger, J. C., **"Physical Chemistry of Airborne Sea Salt Particles and Their Components"**. *Journal of Physical Chemistry A* **2000**, *104*, 11463.
(45) Wingen, L. M.; Moskun, A. C.; Johnson, S. N.; Thomas, J. L.; Roeselová, M.; Tobias, D. J.; Kleinman, M. T.; Finlayson-Pitts, B. J., **"Enhanced Surface Photochemistry in Chloride-Nitrate Ion Mixtures "**. *Physical Chemistry Chemical Physics* **2008**, *10*, 5668
(46) Saliba, N. A.; Yang, H.; Finlayson-Pitts, B. J., **"Reaction of Gaseous Nitric Oxide with Nitric Acid on Silica Surfaces in the Presence of Water at Room Temperature"**. *Journal of Physical Chemistry A* **2001**, *105*, 10339.
(47) Knipping, E. M.; Lakin, M. J.; Foster, K. L.; Jungwirth, P.; Tobias, D. J.; Gerber, R. B.; Dabdub, D.; Finlayson-Pitts, B. J., **"Experiments and Simulations of Ion-Enhanced Interfacial Chemistry on Aqueous NaCl Aerosols"**. *Science* **2000**, *288*, 301.
(48) Laskin, A.; Gaspar, D. J.; Wang, W.; Hunt, S. W.; Cowin, J. P.; Colson, S. D.; Finlayson-Pitts, B. J., **"Reactions at Interfaces as a Source of Sulfate Formation in Sea-Salt Particles"**. *Science* **2003**, *301*, 340.
(49) Gebel, M. E.; Finlayson-Pitts, B. J., **"Uptake and Reaction of $ClONO_2$ on NaCl and Synthetic Sea Salt"**. *Journal of Physical Chemistry A* **2001**, *105*, 5178.
(50) *International Critical Tables of Numerical Data of Physics, Chemistry, and Technology*; Washburn, E. W., Ed.; published for National Research Council by McGraw-Hill Book Company: New York, 1926.
(51) Foster, M. C.; Ewing, G. E., **"Adsorption of Water on the NaCl(001) Surface. II. An Infrared Study at Ambient Temperatures"**. *Journal of Chemical Physics* **2000**, *112*, 6817.
(52) Gregg, S. J.; Sing, K. S. W., *Surface Area and Porosity*, 2 ed.; Academic Press: London, **1997**.
(53) Romakkaniemi, S.; Haemeri, K.; Vaekevae, M.; Laaksonen, A., **"Adsorption of Water on 8-15 nm NaCl and $(NH_4)_2SO_4$ Aerosols Measured using an Ultrafine Tandem Differential Mobility Analyzer"**. *Journal of Physical Chemistry A* **2001**, *105*, 8183.
(54) Cinkotai, F. F., *Aerosol Science* **1971**, *2*, 325.
(55) Biskos, G.; Russell, L. M.; Buseck, P. R.; Martin, S. T., **"Nanosize Effect on the Hygroscopic Growth Factor of Aerosol Particles"**. *Geophys. Res. Lett.* **2006**, *33*, L07801.
(56) Pruppacher, H. R.; Klett, J. D., *Microphysics of Clouds and Precipitation*; Kluwer Academic Boston, 1997, **1997**.
(57) Hansson, H. C.; Rood, M. J.; Koloutsou-Vakakis, S.; Hameri, K.; Orsini, D.; Wiedensohler, A., **"NaCl Aerosol Particle Hygroscopicity Dependence on Mixing with Organic Compounds"**. *Journal of Atmospheric Chemistry* **1998**, *31*, 321.
(58) Choi, M. Y.; Chan, C. K., **"The Effects of Organic Species on the Hygroscopic Behaviors of Inorganic Aerosols"**. *Environmental Science and Technology* **2002**, *36*, 2422.
(59) Woods, E., III; Kim, H. S.; Wivagg, C. N.; Dotson, S. J.; Broekhuizen, K. E.; Frohardt, E. F., **"Phase Transitions and Surface Morphology of Surfactant-Coated Aerosol Particles"**. *Journal of Physical Chemistry A* **2007**, *111*, 11013.
(60) Chen, Y.-Y.; Lee, W.-M. G., **"Hygroscopic Properties of Inorganic-Salt Aerosol with Surface-Active Organic Compounds"**. *Chemosphere* **1999**, *38*, 2431.
(61) Chen, Y.-Y.; Lee, W.-M. G., **"The Effect of Surfactants on the Deliquescence of Sodium Chloride"**. *Journal of Environmental Science and Health* **2001**, *A36*, 229.
(62) Alshawa, A.; Dopfer, O.; Harmon, C. W.; Nizkorodov, S. A.; Underwood, J. S., **"Hygroscopic Growth and Deliquescence of NaCl Nanoparticles Coated with Surfactant AOT"**. *Journal of Physical Chemistry A* **2009**.
(63) Iyota, H.; Krastev, R., **"Miscibility of Sodium Chloride and Sodium Dodecyl Sulfate in the Adsorbed Film and Aggregate"**. *Colloid Polymer Science* **2008**.
(64) Peterson, M. D.; Harmon, C. W.; Nizkorodov, S. A., **"Effects of Surfactants on the Deliquescence of Bulk and Nanocrystalline Salt"**. *UCI Undergraduate Journal* **2009 submitted**.
(65) Dick, W. D.; Saxena, P.; McMurry, P. H., **"Estimation of Water Uptake by Organic Compounds in Submicron Aerosols Measured During the Southeastern Aerosol and Visibility Study"**. *Journal of Geophysical Research* **2000**, *105*, 1471.
(66) Wise, M. E.; Surratt, J. D.; Curtis, D. B.; Shilling, J. E.; Tolbert, M. A., **"Hygroscopic Growth of Ammonium Sulfate/Dicarboxylic Acids"**. *Journal of Geophysical Research* **2003**, *108*, 4638.

(67) Varutbangkul, V.; Brechtel, F. J.; Bahreini, R.; Ng, N. L.; Keywood, M. D.; Kroll, J. H.; Flagan, R. C.; Seinfeld, J. H.; Lee, A.; Goldstein, A. H., **"Hygroscopicity of Secondary Organic Aerosols formed by Oxidation of Cycloalkenes, Monoterpenes, Sesquiterpenes, and Related Compounds"**. *Atmospheric Chemistry and Physics* **2006**, *6*, 2367.
(68) Stokes, R. H.; Robinson, R. A., **"Interactions in Aqueous Nonelectrolyte Solutions. I. Solute-Solvent Equilibriums"**. *Journal of Physical Chemistry* **1966**, *70*, 2126.
(69) Shulman, M. L.; Jacobson, M. C.; Carlson, R. J.; Synovec, R. E.; Young, T. E., **"Dissolution Behavior and Surface Tension Effects of Organic Compounds in Nucleating Cloud Droplets"**. *Geophysical Research Letters* **1996**, *23*, 277.
(70) Sorjamaa, R.; Svenningsson, B.; Raatikainen, T.; Henning, S.; Bilde, M.; Laaksonen, A., **"The role of surfactants in Köhler Theory Reconsidered"**. *Atmospheric Chemistry Physics* **2004**, *4*, 2107.
(71) Hameri, K.; Laaksonen, A.; Vakeva, M.; Suni, T., **"Hygroscopic Growth of Ultrafine Sodium Chloride Particles"**. *Journal of Geophysical Research* **2001**, *106*, 20749.
(72) Hameri, K.; Vakeva, M.; Hansson, H.-C.; Laaksonen, A., **"Hygroscopic Growth of Ultrafine Ammonium Sulphate Aerosol Measured Using an Ultrafine Tandem Differential Mobility Analyzer"**. *Journal of Geophysical Research* **2000**, *105*, 22231.
(73) Mirabel, P.; Reiss, H.; Bowles, R. K., **"A Theory for the Deliquescence of Small Particles"**. *Journal of Chemical Physics* **2000**, *113*, 8200.
(74) Russell, L. M.; Ming, Y., **"Deliquescence of Small Particles"**. *Journal of Chemical Physics* **2002**, *116*, 311.
(75) Biskos, G.; Malinowski, A.; Russell, L.; Buseck, P.; Martin, S., **"Nanosize Effect on the Deliquescence and the Efflorescence of Sodium Chloride Particles"**. *Aerosol Science and Technology* **2006**, *40*, 97.
(76) Biskos, G.; Paulsen, D.; Russell, L. M.; Buseck, P. R.; Martin, S. T., **"Prompt Deliquescence and Efflorescence of Aerosol Nanoparticles"**. *Atmospheric Chemistry and Physics* **2007**, *6*, 4633.
(77) Bahadur, R.; Russell, L. M.; Alavi, S., **"Surface Tensions in NaCl-Water-Air Systems from MD Simulations"**. *Journal of Physical Chemistry B* **2007**, *111*, 11989.
(78) Bahadur, R.; Russell, L. M., **"Effect of Surface Tension from MD Simulations on Size-Dependent Deliquescence of NaCl Nanoparticles"**. *Aerosol Science and Technology* **2008**, *42*, 369.

Chapter 2 – Experimental Approach for Studying Hygroscopic Growth of Amphiphilic Nanoparticles

Section 2.1 – *Nanoparticle Aerodynamics and Physical Properties*

2.1.1 – Particle Mobility

Mobility of a particle is defined as a proportionality constant between the particle's velocity of motion through a medium and the force responsible for this motion. There are many types of forces and physical parameters, such as particle shape, density, and size, just to name a few examples, which give rise to the observed mobility of a particle suspended in air.

Particles quickly reach terminal velocity in air due to their small mass.[1] This occurs when the force of drag (F_D) on the particle equals the force of gravity whereby particles achieve a constant velocity, called settling velocity v_{TS}.[1]

$$v_{TS} = \frac{\rho_p d^2 g}{18\eta} \qquad (2.1)$$

Equation 2.1 is the definition of settling velocity, where d is the particle diameter, η is the viscosity of air, ρ_p is the particle density, and g is acceleration due to gravity. Stoke's law, derived from the Navier-Stoke's equations, gives the force due to drag for sufficiently small spherical objects such as atmospheric particles.[1] The density of the surrounding fluid, in this case gas (ρ_g), should be considered with settling velocity only when its magnitude is comparable to the density of the particle.[1] Ergo, for most atmospheric particles this can be neglected as $\rho_p / \rho_g = 800$ for a water droplet suspended in air.[1] Equation 2.1 is accurate for predicting particle settling velocity for $d > 1\ \mu m$.[1] The mobility coefficient is by definition the ratio of the applied force to the settling velocity (equation 2.2). The type of force applied gives rise to different types of mobility, such as electrical mobility ($^{*}Z_p$) when an electric field is applied (F_E) or mechanical mobility (B) for particles settling in air.[1]

$$B = \frac{F_D}{v_{TS}} = 3\pi\eta d$$
$$^{*}Z_p = \frac{F_E}{v_{TS}} \qquad (2.2)$$

In Stoke's law it is assumed the relative velocity of the gas is zero at the particle's surface. When a particle's size approaches that of the mean free path of air (λ), 66 nm at 298 K,[1] this condition is no longer met.[1] Small particles (<< λ) essentially "slip" through air as their settling velocities are much larger than those predicted by equation 2.1.[1] In 1910, Cunningham[2] derived a correction factor, called the Cunningham slip correction factor $C_c(Kn)$, to correct the drag on a particle predicted by Stoke's law (equation 2.3).[1]

$$F_D = \frac{3\pi\eta v_{TS} d}{C_c(Kn)} \qquad (2.3)$$

$$C_c(Kn) = 1 + Kn\left[\alpha + \beta\, exp\left(\frac{-\gamma}{Kn}\right)\right] \qquad (2.4)$$

$$Kn = \frac{2\lambda}{d} \qquad (2.5)$$

The empirical parameters in equation 2.4 α, β, and γ are 1.142, 0.558, and 0.999, and are suitable for aqueous droplets.[3] The Cunningham slip correction factor is a function of Knudsen number, Kn, which is a ratio of the mean free path of air to the particle diameter (equation 2.5). This factor is a numerical metric of whether a particle is in the free molecular flow regime (v, Kn > 10), transition regime (t, 10 > Kn > 0.1), or continuum flow regime (c, Kn < 0.1).[1]

Particle shape can also have an influence on particle mobility, as a principal underlying assumption in Stoke's law is that the particles are spherical. While assuming particles are spherical for liquid droplets is accurate,[1] the same is not true for solid particles as they may have a fairly ordered crystalline structure, such as NaCl, which is typically cubic in shape.

One can still "rescue" the equations derived for spherical particles by introduction of an appropriate shape correction. Particle shape factor (χ) is used to account for irregularly shaped particles and its influence on mobility. Shape factor is defined as the ratio of the force of drag on the irregular particle to that of the force of drag on a spherical particle of the same volume (equation 2.6). In equation 2.7, d_e is the envelope equivalent diameter (often referred to as volume equivalent diameter) and is the diameter of a sphere which as the same aerodynamic properties and density as the irregularly shaped particle.[4] Shape factor χ is always greater than 1 for irregular particles and is 1 for spherical particles.[1] The reader is encouraged to review Figure 1 of DeCarlo et al.[4] and Table 3.2 of *Aerosol Technology*[1] for a list of various shape factors. Consequently, settling velocity is also affected by shape as can be seen in equation 2.8.[1]

$$\chi = \frac{F_D}{F_D^{sphere}} \tag{2.6}$$

$$\chi = \frac{F_D}{3\pi\eta v_{TS} d_e} \tag{2.7}$$

$$v_{TS} = \frac{\rho_p {d_e}^2 g}{18\eta\chi} \tag{2.8}$$

The mobility diameter (d_m) of a particle is the diameter derived from electrical mobility using Stoke's Law. Figure 2.1 demonstrates how mobility diameter is typically measured, whereby a particle only with the proper diameter to charge (typically ±1 charge state)[1] ratio will exit the electric field provided by a high voltage (HV) source in the mobility analyzer column. An irregular particle will have a smaller settling velocity in the electric field than a spherical particle of the same mass and charge state.[1,4] Consequently, the envelop equivalent diameter is always smaller than the mobility diameter for irregular particles.[1,4]

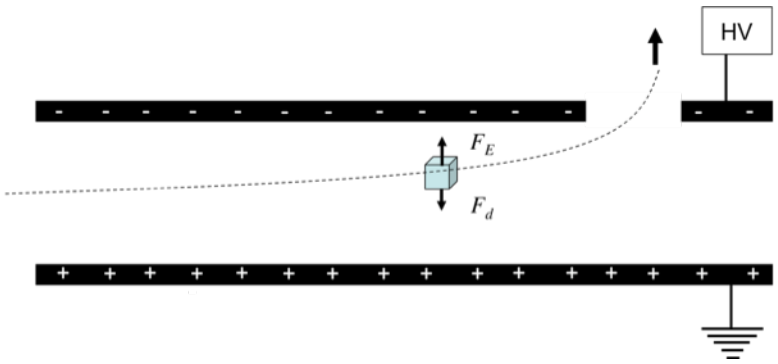

Figure 2.1: Demonstration of an electrical mobility measurement of particle diameter. Key: HV = high voltage

Equation 2.9 demonstrates the relationship between mobility diameter and envelop equivalent diameter, which is related to shape factor. Shape factor is 1.08 for sufficiently large cubic particles;[1] however, can be different when particles are sufficiently small (d < 100 nm). Furthermore, the Cunningham slip correction factor must also be considered for small particles. Equation 2.10 shows how to calculate the envelope equivalent diameter for d < 100 nm.

$$d_e \cdot \chi = d_m \tag{2.9}$$

$$\frac{d_e \cdot \chi_{c,t,v}}{C_c(d_e)} = \frac{d_m}{C_c(d_m)} \tag{2.10}$$

Because the Cunningham slip correction factor depends on diameter, solving equation 2.10 can be difficult with only knowledge of the mobility diameter and expected shape factor in the appropriate flow regime (for example, free molecular v). This relationship has been calculated iteratively in a previous publication of ours[5] and those results are presented in TABLE 2.1.

TABLE 2.1: Envelope Equivalent Diameter Calculations

d_m (nm)	Kn	$\chi(Kn)$	d_e (nm)
9.0	14.7	1.25 [a]	8.1
10.8	12.2	1.25	9.7
10.9	12.1	1.25	9.8
14.0	9.43	1.23 [b]	12.5
14.1	9.36	1.23	12.7
17.0	7.76	1.23	15.2

[a] Calculated from Dahneke et al.[6-8]

[b] Calculated by methods of DeCarlo et al.[4]

2.1.2 – Particle Size Statistics

Often a population of particles is not monodisperse in size; rather, it is polydisperse. In other words, there is a distribution of diameters characterized by a mean size and some measure of width.[1] Because of the large dependence of particle mobility on diameter, it is important to characterize particle diameters with statistical treatments. Furthermore, particle measurements are often made that are only sensitive to a range, albeit narrow, of diameters, which are binned into size batches. The reader is encouraged to read sections 4.1-4.3 of *Aerosol Technology*[1] for a detailed review of statistical distributions.

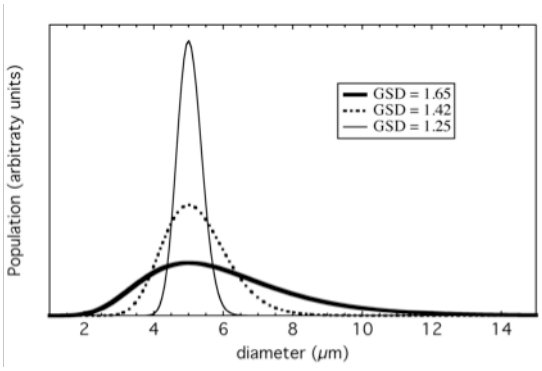

Figure 2.2: The lognormal distribution of identical particle populations with varying GSD.

The lognormal distribution is a commonly used distribution for empirically fitting measured particle size bins, or distributions. The normal distribution is not used for particle size statistics because most aerosol have populations that have an asymmetrical distribution skewed toward larger sizes.[1] The lognormal distribution df and geometric standard deviation (GSD) $\ln\sigma_p$ are shown in equations 2.11 and 2.12, respectively below. In equation 2.12, $\bar{d}_p$ is the geometric mean diameter.[1] Figure 2.2 shows a lognormal distribution for three particle populations with identical diameters, identical populations, and different GSD.

$$df = \frac{1}{\sigma_p\sqrt{2\pi}} exp\left(-\frac{\left(\ln d_p - \ln\bar{d}_p\right)^2}{2\left(\ln\sigma_p\right)^2}\right) d\ln d_p \qquad (2.11)$$

$$\ln\sigma_p = \left(\frac{\sum\left(\ln d_i - \ln\bar{d}_p\right)^2}{N-1}\right)^{1/2} \qquad (2.12)$$

Section 2.2 – *Electrospray as a Source of Nanoparticles*

2.2.1 – Electrospray Overview

Even though electrospray ionization is generally used to produce gas phase ions for mass spectrometric analysis,[9] it also has other applications. Electrospray ionization-atomization has been shown to generate aerosol particles from highly conductive, concentrated ($c > g\ L^{-1}$) solutions in the nanometer-size range.[5,10-18] The size of the particle generated is a strong function of electrospray conditions.[5,10] Rulisen et al.[10] were the first to use electrospray, operating in the jet-cone mode, as a means of atomizing solutions of sodium iodide in n-proply alcohol to make particles with mobility-equivalent diameters between 20 and 100 nm.[10] Researchers found as the concentration of the solutions were increased, the mobility-equivalent diameter decreased.[10]

In electrospray ionization, a conductive solution is forced through a thin capillary (typically 100-250 μm I.D.) at a certain volumetric flow rate v_f (typically ~1 μL min^{-1}) with an applied high voltage (HV) potential V_{apply} (typically 3 kV, positive or negative).[19] At a specific flow rate, applied potential, solution conductivity and surface tension a Taylor jet-cone forms,[19] seen in Figure 2.3. In the Taylor jet-cone, $\theta = 49.3°$, the current on the capillary is typically 10^{-8} to 10^{-6} A, the diameter (D_d) of the droplet is 1-10 μm, and the charge on initial, or primary, droplets is 10^{-13} to 10^{-17} C.[19] Solution surface tension can also make a difference in electrospray atomization of liquids.[19] For example, if the solution is neat water, which has a high surface tension, the applied potential required to overcome the surface tnesion will exceed the break down potential of air and resultantly will arc across the syringe before a Taylor jet-cone forms.[19] Various alcohols, though

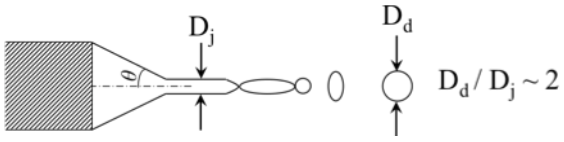

Figure 2.3: A Taylor jet-cone illustration of electrospray atomization.

mostly methanol, are typically used as an electrospray solvent because they have relatively low surface tensions and most analytes, or solutes, are quite soluble in alcohol.[19] They can be sprayed directly in air without electric breakdown.

Figure 2.4 shows an overview of the entire electrospray process. After the formation of the Taylor jet-cone and primary drop formation (1), shrinkage of droplets by solvent evaporation and disintegration occurs (2). This is known as Rayleigh evaporation, whereby the Coulombic repulsion of surface charges is enough to overcome the surface tension of the liquid. Highly charged droplets consequently disintegrate due to electrostatic repulsion into smaller secondary droplets once they pass the Rayleigh limit charge state q_{Ry}.

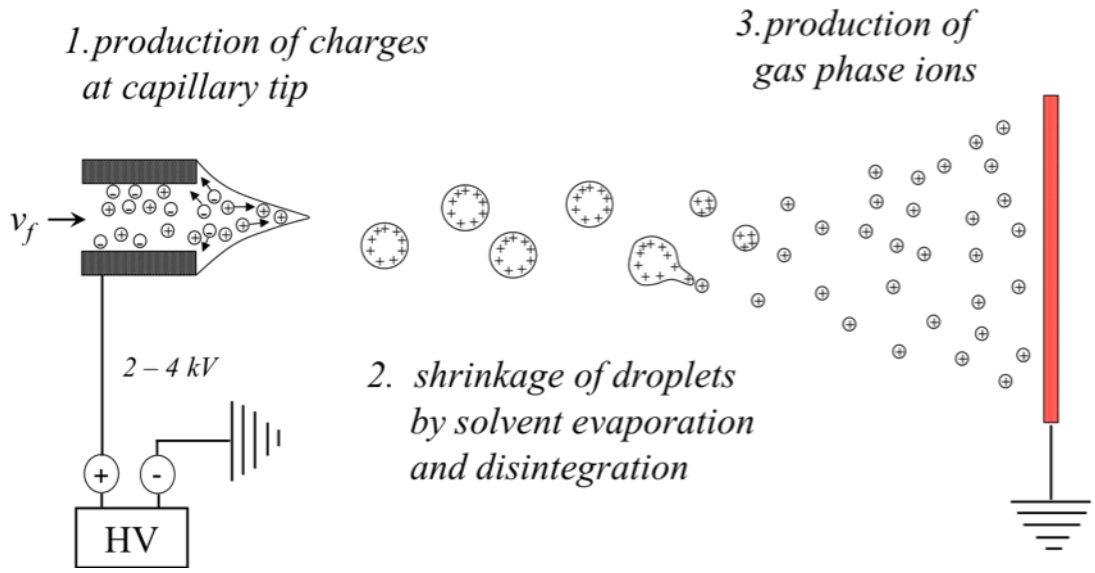

Figure 2.4: An overview of the electrospray ionization-atomization process.

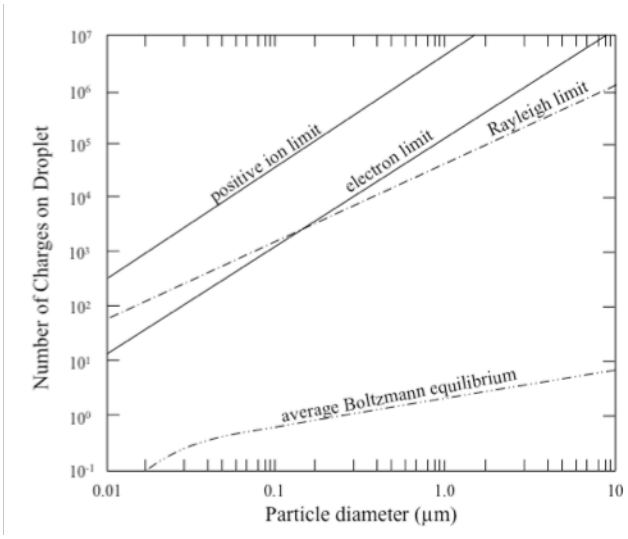

Figure 2.5: Number of charges on a droplet vs. size.

Figure 2.5 is adapted from *Aerosol Technology*[1] and shows the number of charges on a droplet vs. droplet diameter for a positive ion being ejected from the droplet, an electron ejected from the droplet and the Rayleigh limit. The Rayleigh limit is much less than the positive ion or electron limit for a given particle diameter in the micron regime. For example, a 2 μm droplet would have roughly 10^5 charges stabilized on the surface (such as in a Gaussian object) as predicted by the Rayleigh limit.[19] As the droplet flies down the trajectory shown in Figure 2.4, solvent evaporates and consequently the droplet charge state increases. When it increases past the Rayleigh limit several smaller secondary droplets are ejected from the primary droplet, which are under the Rayleigh limit. Subsequently, as they fly down field lines and evaporate they too will reach the Rayleigh limit and generate even smaller droplets. This process will continue until either a single gas phase ion (3) is produced or a dry, solid, nanoparticle if the solution concentration is large enough.[19]

2.2.2 – Neutralization and the Average Boltzmann Distribution of Charge States

In electrospray ionization-atomization production of nanoparticles a grounded radioactive neutralizer is typically used as a means to enhance the throughput efficiency of nanoparticle production.[10] Beta-sources of radiation are typically used, which produce a weak plasma containing positrons and electrons.[1] This allows for rapid neutralization of highly charged droplets (of either a positive or negative charge state) from collisional neutralization of

the surrounding charged carrier gas.[1,10] The resulting particle population is typically monodisperse in diameter and is believed to have an average Boltzmann distribution of charge states.[1] Figure 2.6 shows an average Boltzmann distribution of charge states for 10, 20, 50 and 100 nm particles. As can be seen in the figure, the majority of the particles for any size are predicted to be neutral; however, as the size of the particle decreases the charge state becomes more monodisperse. Larger diameter particle populations are therefore predicted to have a higher concentration of multiply charged particles, which has been confirmed by measurements.[1] In the size range of interest to this work (< 20 nm) all particles are either neutral or singly charged.

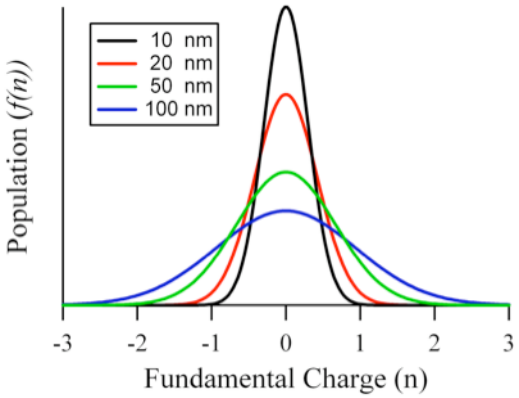

Figure 2.6: Average Boltzmann distribution of charge states for 10, 20, 50 and 100 nm particles.

Section 2.3 – *Hygroscopicity Experimental Schematic*

2.3.1 – Electrospray Source of NaCl and SDS/NaCl Nanoparticles

Figure 2.7 shows the experimental schematic for the in-house designed electrospray nanoparticle generator (ENG). Variable amounts of NaCl (Sigma-Aldrich, 99.999%) and SDS (Fluka, ≥ 99.0%) were dissolved in deionized HPLC grade water (OmniSolv, < 8 μΩ·cm) to achieve a combined concentration of ~2 g L^{-1}. A small amount (< 5%) of methanol (Sigma-Aldrich, HPLC grade, > 99.9%) was added to each solution in order to enhance the electrospray jet-cone stability. The solutions were pushed through a 5 cm long, 100 μm I.D. quartz capillary with a syringe pump (780100 KD Scientific) at a typical flow rate of 30-100 μL hr^{-1}. High voltage (2-4 kV) (positive) was applied directly to the stainless steel union connecting the capillary to the

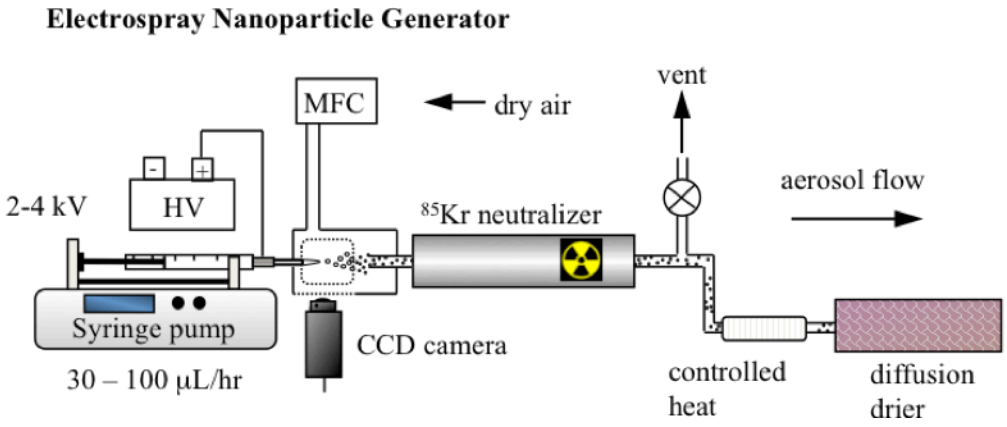

Figure 2.7: Experimental schematic of the electrospray nanoparticle generator. Key: HV = high voltage and MFC = mass flow controller.

syringe(Hamilton GT, 500 μL). The capillary entered a small (~5 cm^3) chamber equipped with transparent windows for easy viewing of the electrospray jet with a microscope objective and CCD camera. The end of the capillary was positioned (electrospray distance, l_s) 3-6 mm away from the electrically grounded 6 mm O.D. entrance tube of a bipolar neutralizer (^{85}Kr, 10 mCi, TSI Model 3054). A mass flow controller (MFC) sent a ~600 SCCM (standard cubic centimeter per minute) flow of dry, filtered air into the chamber to help with carrying the aerosol into the neutralizer. Roughly 50% of this flow was vented to keep the system at atmospheric pressure. In some experiments, the nanoparticle flow was sent into a controlled heater followed by diffusion drier. Particle mobility diameter as a function of applied temperature was monitored and this analysis revealed diameters did not change between 25-300°C, indicating the particles were void of solvent after neutralization.[5] Figure 2.8 at the end of this section shows a photograph of the electrospray nanoparticle source and in an inset is a photograph of the Taylor jet-cone taken from the CCD camera.

TABLE 2.2 shows the electrospray conditions for nanoparticle production that resulted from the various solutions of SDS and NaCl. These conditions represent optimized electrospray protocols for sustaining the cone-jet mode over long periods of time (~6 hours). The employed

electrospray protocols presented in TABLE 2.2 also generated reproducible particle size characteristics. The GSD was always ~1.3 and the geometric mean mobility diameter was always between 15-25 nm depending on the solution that was electrosprayed. In the higher SDS containing solutions, the geometric mean mobility diameter was always larger than the lower SDS containing solutions. Varying the electrospray distance l_s had a dramatic effect on the particle size characteristics. When l_s was decreased (i.e. when the capillary was pushed closer to the neutralizer) the GSD of the particle distribution typically increased and the geometric mean mobility diameter changed. In some cases it increased, in other cases it decreased. Though as long as the conditions presented in TABLE 2.2 were employed, those particle size characteristics resulted. Ergo, during hygroscopicity experiments it was very necessary to reproduce the particle size characteristics and electrospray protocols and maintain them throughout the course of experimentation.

TABLE 2.2: Electrospray Conditions and Particle Size Characteristics of Various SDS/NaCl solutions

wt % SDS[a]	χ_{NaCl}[b]	total solution concentration (g/L)	applied potential (kV)	flow rate (μL/hr)	l_s (mm)[c]	d_m (nm)[d]	particle concentration (x10^5 cm^{-3})	GSD[e]
0.0	1.00	1.52	3.4	109	4.0	15.2	0.67	1.29
5.0	0.99	1.98	3.2	83	4.0	15.2	0.57	1.27
11	0.98	2.05	3.1	81	5.0	15.5	0.67	1.26
23	0.94	1.93	3.2	81	4.0	17.9	1.04	1.36
50	0.83	2.03	3.1	81	6.0	24.5	1.43	1.33

[a] dry weight percent of SDS in solution
[b] dry mol fraction of NaCl in solution
[c] electrospray distance from capillary tip to neutralizer entrance
[d] geometric mean mobility diameter of electrosprayed nanoparticles prior to size selection
[e] geometric standard deviation (GSD)

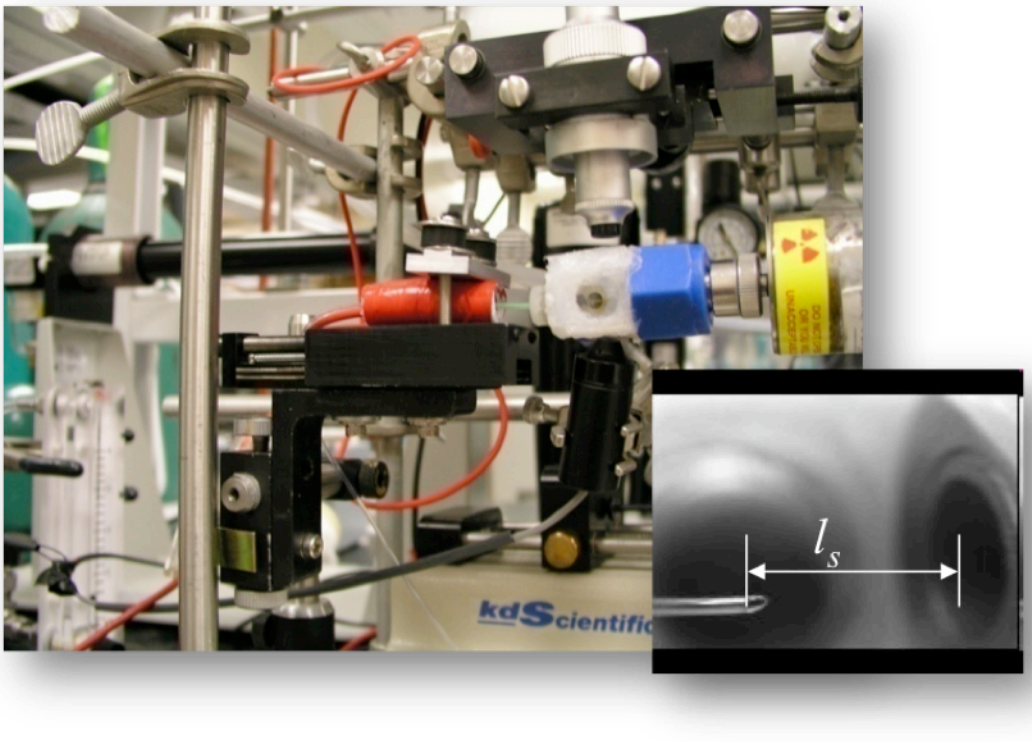

Figure 2.8: The electrospray nanoparticle generator. In an inset is a CCD image of the Taylor jet-cone, which is a distance l_s from the grounded neutralizer entrance.

In the photograph in Figure 2.8, the stainless steel union that connects the syringe to the capillary and provides electrical contact for electrospraying is covered in red electrical tape for safety. The electrospray house, which contains the Taylor jet-cone presented in the inset and taken from the CCD camera, can be seen with a blue Teflon™ union connecting it to the ^{85}Kr bipolar neutralizer. The stainless steel union and capillary rests on a linear translator, which provides the movement for varying the electrospray distance l_s.

2.3.2 – Size Selection and the Tandem Nano-Differential Mobility Analyzer Technique

The electrospray nanoparticle generator produced fairly monodisperse (GSD ~1.3) nanoparticle populations; however, size selection using tandem nano-differential mobility analyzer (DMA) techniques has been shown to make even more monodisperse populations of particles (GSD ~1.05).[11-16,20] Before demonstrating the tandem nano-DMA technique, the TSI

Model 3085 DMA will be reviewed briefly, which is the prototype of mobility analyzers used in this work.

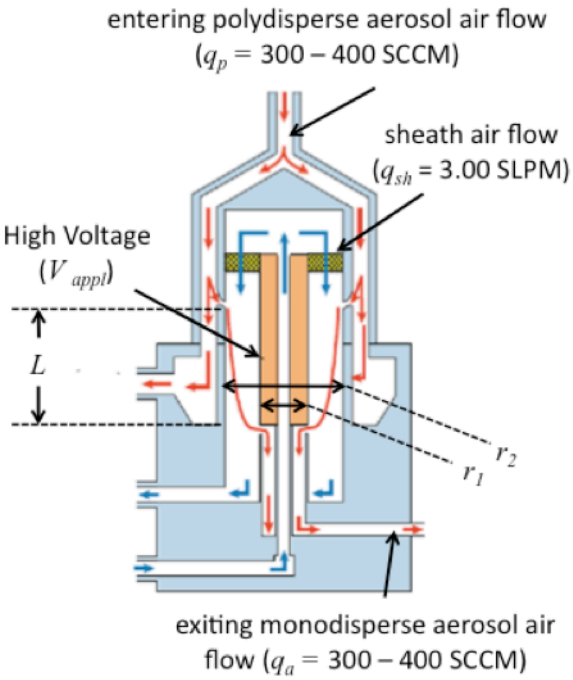

Figure 2.9: The TSI 3085 nano-Differential Mobility Analyzer. The figure is adapted from the TSI 3080 operations manual. Key: SCCM = standard cubic centimeter per minute, L = length, r_1 = inner radius, r_2 = outer radius

Figure 2.9 is a schematic of the TSI 3085 nano-DMA.[21] A flow of polydisperse particles q_p from a source, in this case the ENG, is sent though the top of the DMA at 300-400 SCCM. An applied voltage V_{appl} (10-10,000 VDC) provides a steady electric field, which particles drift through, as depicted in the illustration (Figure 2.1) presented earlier in section 2.1.1. Only particles with the proper diameter-charge ratio (as predicted from the average Boltzmann charge distribution) for 5-300 nm particles will exit the DMA at a certain V_{appl} at the aerosol flow rate q_a, which is set to match q_p described below. The sheath airflow rate q_{sh} is set to 3.00 SLPM (standard liters per minute) and functions as a carrier gas for exiting particles as well as a means to prevent particle build-up on the inner pole. L is the length of the mobility region (10.5 cm),

r_1 is the inner radius of the mobility region (4.5 cm) and r_2 is the outer radius of the mobility region (7.9 cm).

Electrical mobility ($^*Z_p$) is calculated by equation 2.17, which is inversely proportional to the applied voltage. From Stoke's law, electrical mobility diameter is seen in equation 2.18 and is inversely proportional to electrical mobility. Therefore, as the applied voltage increases the size of the particle which exits the DMA increases. There is also an experimental bandwidth associated with measuring particle mobility, and is shown in equation 2.19 as the ratio of the aerosol flow rate to sheath airflow rate.[21]

$$^*Z_p = \frac{q_{sh}}{2\pi V_{appl} L} \ln\left(\frac{r_2}{r_1}\right) \quad (2.17)$$

$$d_m = \frac{neC_c}{3\pi\eta\, ^*Z_p} \quad (2.18)$$

$$\Delta^*Z_p = \frac{q_a}{q_{sh}} {}^*Z_p \quad (2.19)$$

There are two modes that a DMA can operate in. When the applied voltage is increased rapidly per increment time (typically a few V sec^{-1}), which can be done with the electrostatic classifier (TSI Model 3080) or even an in-house computer program and hardware, this is called the scanning mode. This is the most utilized mode of operation and when a DMA is connected to a particle detector (discussed below) a size distribution for a polydisperse population of particles can be measured over the course of a few hundred seconds or less. Longer scan times give higher precision in measuring a polydisperse population of particles. When the applied voltage is fixed, this is called the selection mode. A narrow distribution of geometric mean mobility diameters of any choosing can be selected from a polydisperse population of particles in the selection mode by empirically adjusting the applied voltage. Note, 2 DMAs must be used in this mode: i.e. DMA 1 for selecting, which is upstream from DMA 2 (connected to a detector)

for quantifying the selected monodisperse particle population. This selection mode of operation, when combined with a second DMA for detection, is called the tandem nano-DMA technique.

Figure 2.10 shows two measured mobility histograms of nanoparticles from the ENG, which have been fitted with lognormal curves. Panel (a) is the nanoparticle distribution directly after the bipolar neutralizer. Panel (b) is the nanoparticle distribution directly after DMA 1, where a size selection was made. To generate this figure, DMA 2 (scanning mode) was used to measure the particle distribution from the ENG. After obtaining this histogram, DMA 1 (selecting mode) is connected directly downstream from the ENG, followed by DMA 2, which is connected to the detector. As can be seen in panel (b), when a size selection is made a narrow distribution (GSD = 1.05) of particles can be selected. In this case, the measured mobility diameter in panel (b) is identical to the mobility diameter selected from DMA 1 because nothing has happened to the particles. If particles were exposed to water vapor after being size selected for example, DMA 2 would quantify this growth after measurement of the initial dry mobility diameter.

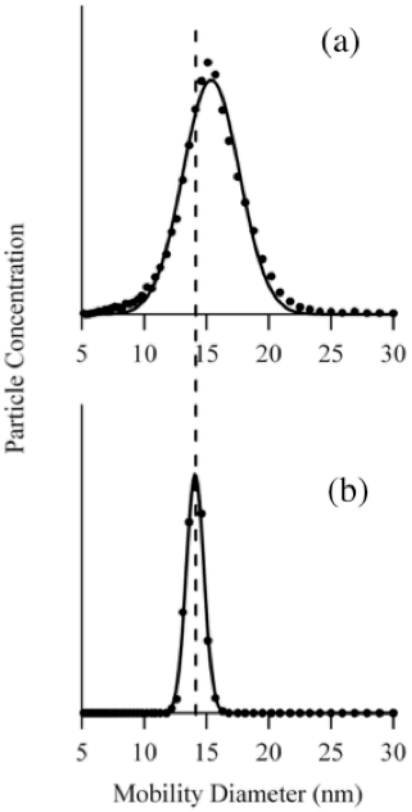

Figure 2.10: **(a)** Initial nanoparticle distribution of ENG, **(b)** nanoparticle distribution after size selection.

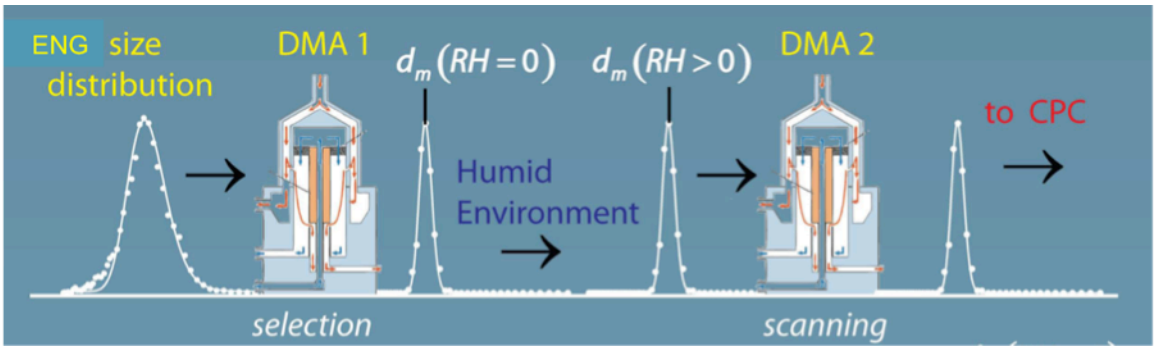

Figure 2.11: The tandem nano-differential mobility analyzer technique. Key: CPC = condensation particle counter, DMA = differential mobility analyzer, ENG = electrospray nanoparticle generator.

Figure 2.11 is an illustration of the tandem nano-DMA technique. The detector shown in this illustration is a condensation particle counter (CPC), which is a commonly used particle detector. In measurements made in this laboratory the TSI 3025A ultrafine CPC is used and is capable of detecting particles as small as 2.5 nm. The operation of this device will not be discussed, although the reader is encouraged to visit the TSI Inc. website at www.tsi.com for a review of the condensation particle counter technique.[22-31]

2.3.3 – Generating and Measuring Relative Humidity

Before discussing the details of the hygroscopicity experiment, as depicted in Figure 2.11, it is necessary to outline how RH is generated and measured. Size selected particles are brought to a desired RH by using a Nafion humidifier (Perma Pure, MD-110-48E-F) which consists of a 2 mm wide, 120 cm long Nafion tube carrying the aerosol flow placed inside a 6 mm plastic tube carrying humidified air in the opposite direction. The Nafion humidifier is a permeable membrane that allows for stable mixing of RH. A rapid and stable adjustment of a desired RH inside the Nafion humidifier is achieved by mixing highly humidified air (RH > 95%) and dry air in different proportions from two independently operated MFCs. Figure 2.12 is a schematic of the aerosol humidity-conditioning region.

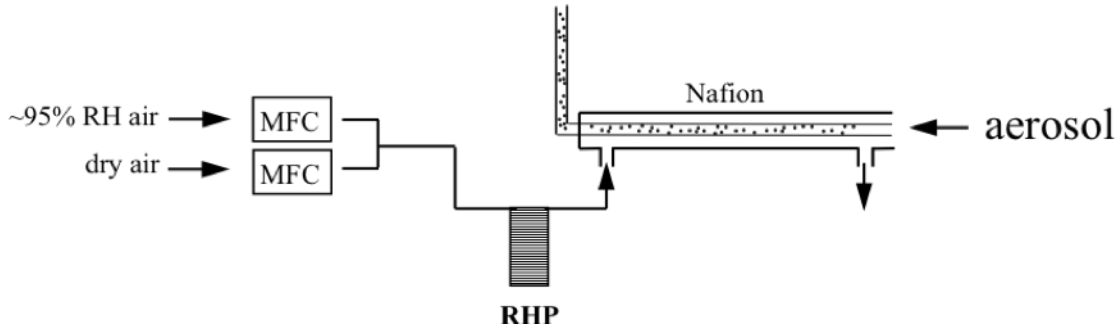

Figure 2.12: The aerosol humidity conditioning region. Key: MFC = mass flow controller, RHP = relative humidity probe.

Humidified air is sent in the opposite direction of the aerosol flow to ensure the maximum RH aerosol experience is just before exiting the humidified region, which is where a relative humidity probe (RHP) is located. A mixing region (not shown) is located just before the RHP, which consisted of a coiled 6 mm Teflon™ tube approximately one meter in length. The Nafion humidifier will burst with flows in excess of 3.0 SLPM; therefore flows were mixed so as not to exceed this value. A constant flow of dry air, roughly 0.50 SLPM, was used and the flow of highly humidified air was increased intermittently to achieve a desired RH.

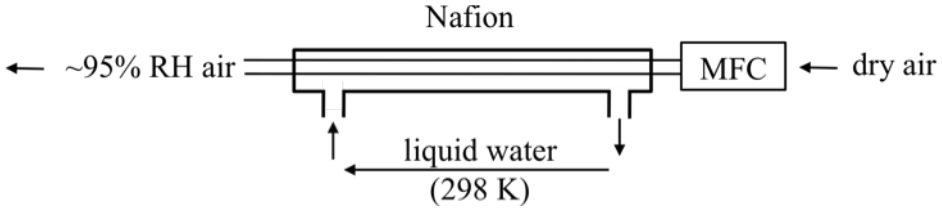

Figure 2.13: The humid air generation region. Key: MFC = mass flow controller

Highly humidified air (~95% RH) was generated in a similar manner (Figure 2.13); however liquid water (295 K) from a temperature-controlled circulator flowed over a coiled 2 mm wide, 240 cm long Nafion humidifier (Perma Pure, MD-110-96E-F) incased in a 6 mm hard plastic tube. Dry, filtered air flowed through the Nafion humidifier line whereas liquid water flowed over the Nafion humidifier line in the opposite direction. The air exiting the Nafion

humidifier is expected to be ~95% RH and is then sent to mix with dry air to provide humidities between 5-95% RH depending on the programmed flow rates.

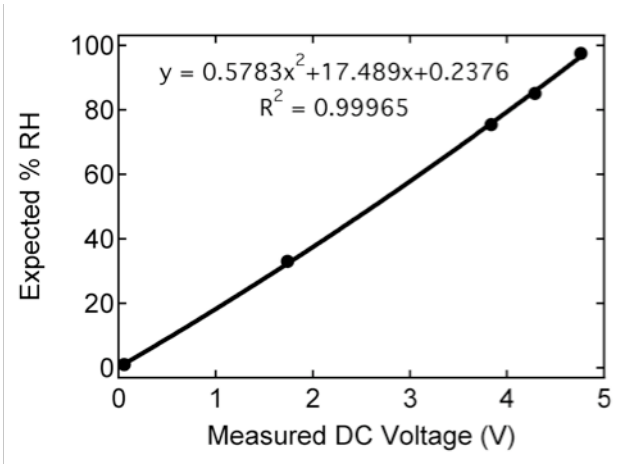

Figure 2.14: Sample calibration curve of Vaisala HMP237 humidity probes.

RH was monitored by Vaisala HMP237 probes, which were periodically calibrated against RH above standard saturated salt solutions. For calibrations, solutions were prepared in a 280 cm^3 Vaisala HMK15 humidity calibrator chamber and allowed to equilibrate for 24 hours before measurement with Vaisala HMP237 humidity probes. The chamber consisted of ports matching the O.D. of the RHP with an o-ring seal to isolate the chamber from the outside environment. Figure 2.14 shows a sample calibration curve using salts $MgSO_4$ (33% RH), NaCl (75% RH), KCl (85% RH), and K_2SO_4 (97.5% RH) at 295K. The zero point is measured from the dry air source shown in Figure 2.12, which was flowed over the RHP for 24 hours in an o-ring sealed, isolated environment. The best achievable accuracy and precision of the probes were ± 1.0% RH and ± 0.1% RH, respectively, in the 0-90% RH range and ± 2.0% RH and ± 0.1% RH, respectively, in the 90-98% RH range.

A 2^{nd} order polynomial fit is used for the calibration of Vaisala HMP237 humidity probes because their response was observed to become non-linear in the high humidity range. A LabView™ program is used to monitor the analog signal from Vaisala HMP237 humidity probes during experimentation, which was constantly updated with the most recent calibration curve shown in Figure 2.14. The first derivative with respect to time of RH signal for all probes is also

monitored during experimentation. When these values are constant and close to zero (~10^4 RH s^{-1}), over a ~20 min interval, the system is regarded as well mixed. In Appendix I a LabView™ block diagram and screen shot of the Vaisala HMP237 humidity probe program is shown.

2.3.4 – Hygroscopicity Experimental Schematic

Figure 2.15 shows a schematic of the entire hygroscopicity experiment. A 0.30–0.40 SLM flow coming from the electrospray source was directed into the first differential mobility analyzer (DMA1, TSI 3085). The applied DC voltage in DMA1 was fixed to allow a narrower distribution (GSD ~1.05) of particle mobility diameters to pass through (at the expense of losing ~99% of the uncharged particles). The DMA1 sheath flow (3.0–4.0 SLM) was operated with a closed loop configuration in which the excess air was filtered twice, dried with a Nafion dryer (PermaPure, MD-110), and re-circulated. The resulting RH of the sheath flow was approximately 1-3% and a vent maintained the flow of the exiting monodisperse particles.

Size selected particles were brought to a desired RH as described above in the conditioning region. Humidified particles were sized in the second nano-DMA (DMA2, TSI 3085) operated in a scanning mode, and counted by a condensation particle counter (CPC, TSI 3025A). The estimated residence time of particles in the humidified flow (Nafion tube + RH probe + DMA2) was ~7 seconds. The sheath air of DMA2 (3.0–4.0 SLM) had a closed loop configuration with an independent control of RH, which was adjusted by mixing humid (RH > 95%) and dry air in different proportions. The excess air was filtered twice and heat exchanged to match the sheath air temperature, which was typically 22 °C.

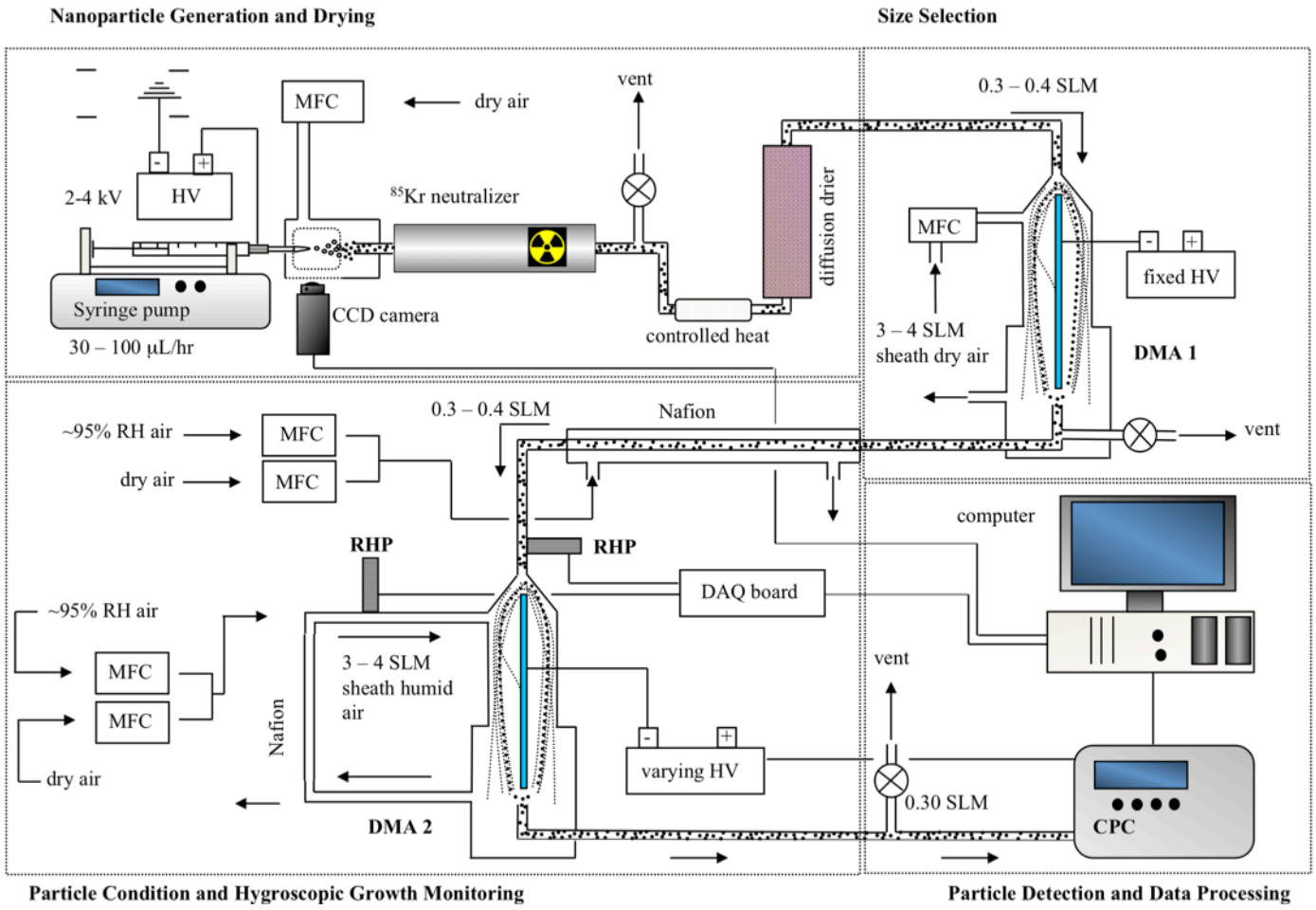

Figure 2.15: The nanoparticle hygroscopicity experimental schematic. Key: DAQ = data acquisition, MFC = mass flow controller, RHP = relative humidity probe, DMA = differential mobility analyzer, CPC = condensation particle counter, SLPM = standard liter per minute, HV = high voltage.

As a matter of experimental convenience to range the humidity exposure time, the DMA2 sheath flow was maintained at a level that was slightly higher than that of the aerosol flow, typically by 0-3% RH. When the difference between the DMA2 sheath flow and the aerosol flow RH was larger than zero, the final particle growth took place inside the DMA2 sheath air region. All growth factors measured in this work are presented as a function of the sheath flow RH encountered by the particles in DMA2. This had the effect of exposing particles to ~1 second of RH. When the RH of the DMA2 sheath air was matched to the RH of the conditioning region, RH exposure time was ~ 7 seconds. In some experiments, a longer and wider tube was placed between the conditioning region and DMA2, which made the humidity exposure time ~70 seconds.

In most measurements, the RH of the aerosol and DMA2 flows were slowly increased in parallel. The electrospray source was operated continuously, and the final particle size distributions were measured several times after the RH values stabilized at a desired level as determined from the LabView™ program. It took approximately two to three days to record each growth curve over a 5-95% RH range. After a 12-hour period it was usually necessary to stop the electrospray source and clean the neutralizer from solid SDS/NaCl deposits forming at its entrance tube. In order to achieve reproducibility in the measured GF_m, it was critical to keep both DMAs and all aerosol tubing free of contamination by volatile organics, especially for measurements on pure NaCl particles.

Section 2.4 – *Equilibrium Vapor Pressure over Bulk Mixtures*

2.4.1 – Measurements above Bulk Mixtures

Equilibrium vapor pressures over bulk solutions containing NaCl and SDS were measured to compare to nanoparticle experiments. Equilibrium vapor pressures over bulk solutions containing NaCl and Na_2SO_4 were also conducted and have previously been reported.[32] Solutions were prepared in the same 280 cm^3 Vaisala HMK15 humidity calibrator chamber as described previously and allowed to equilibrate for 24 hours before measurement with Vaisala HMP237 humidity probes. RH probes were calibrated as previously described for nanoparticles experiments.

In these bulk mixture studies, 3.00 grams of total material (NaCl and SDS or NaCl and Na_2SO_4) mixed in varying proportions and ground to a fine powder were immersed in 5.00 mL of HPLC grade water (OmniSolv, < 8 μΩ·cm) followed by sonication. After equilibration for 24 hours, RH probes were placed in the o-ring sealed chamber ports and humidities were reported after 1 hour probe exposure when the humidity was less than 90 % RH and after 12 hours when the humidity was greater than 90 % RH.

Undergraduate research assistant Mark Peterson, who is now a graduate student at Northwestern University, conducted these experiments. The author is very grateful for Mark's contribution to the project.

Section 2.5 – *Jet Impaction of Nanoparticles for Morphological and Chemical Characterization*

2.5.1 – Inertial Impaction of Nanoparticles

Nanoparticle diffusion coefficients for < 20 nm are relatively high; collecting them on a substrate for morphological and chemical characterization is thus difficult. Inertial, or mechanical, impaction is by far the most utilized and reviewed method of impaction for aerosol particles in general, although electrostatic precipitation of charged particles on a substrate is also common.[1] When a gas-particle beam is impinged normal to a surface a division of particle sizes occurs based on inertia and only those with some critical diameter will continue its straight line motion and impact on the surface.[33]

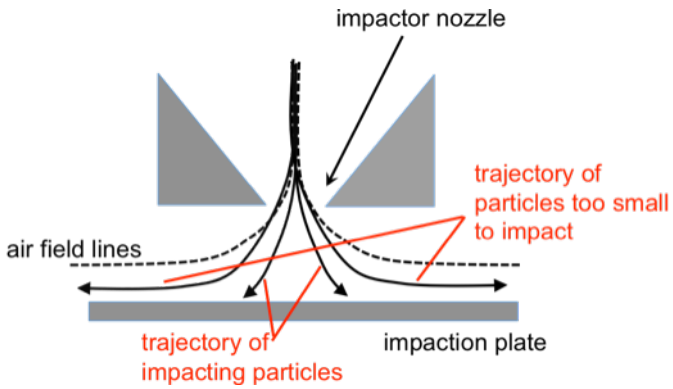

Figure 2.16: Illustration of an inertial particle impactor.

Figure 2.16 shows an illustration of an inertial impactor with two particle trajectories. The smaller particle does not impact on the plate because it is more mobile and thus has a smaller settling velocity toward the plate.[1] If the plate is moved closer than both the smaller and larger particle will impact. When studying monodisperse populations of particles, this is not an issue. However, often particles are not monodisperse and size segregation in impaction for chemical and morphological analysis can be desirable. Cascade impactors are often used for size segregation, which are very similar to the impactor illustrated in Figure 2.16. In a cascade impactor, several stages with different plate to nozzle distances are used to collect a plethora of particle sizes. Typically the smallest particle collection stage, i.e. the smallest plate to nozzle distance, is at the bottom of the impactor and larger particle collection stages increase monotonically up the length of the cascade impactor.

Impactor efficiency is a sharp function of diameter, which have an abrupt "cutoff" region corresponding to a critical diameter for impaction.[1] Impactor stages are usually quantified by their cutoff size, or cutoff diameter d_{50}, which is a diameter that corresponds to 50% collection efficiency.

Most commercial impactors have cutoff diameters in the micron to hundreds of nanometer range,[1] although this threshold is being pushed into the tens of nanometer range. Applied Physics Inc. has recently introduced the Nano-MOUDI (multi orifice uniform deposition impactor) cascade impactor; Model 125 B has a minimum cutoff diameter of 10 nm.[34] TSI Inc. also offers a nano-electrostatic precipitator, Nanometer Aerosol Sampler Model 3089, capable of impacting charged (Boltzmann distribution of charge states) particles between 2-100 nm on any substrate.[35] Commercial devices are reliable, although generally expensive; for example, the two previously mentioned devices cost in the $20,000 range. Thus, it was desirable to construct an in-house device capable of impacting 10-20 nm particles on any substrate for chemical and morphological analysis of SDS/NaCl nanoparticles.

Due to the highly mobile nature of nanoparticles, inertial impactors operating in the supersonic and hypersonic flow regimes have proven to be quite effective. [33,36-38] Under normal impaction conditions, nanoparticles will follow gas streamlines and miss the impaction plate altogether.[38] In a supersonic or hypersonic impactor, a gas-particle beam is expanded through a pinhole (typically microns in diameter) into an evacuated region (typically a few torr). The expanding jet accelerates supersonically (or hypersonically depending on the pressure drop across the pinhole) into a region of considerably lower pressure where a plate for impaction is located downstream.[33] Consequently, the mean free path of gas increases considerably near the plate and the force of drag acting on the nanoparticle decreases, which allows nanoparticles to be trapped on the impactor plate.[38] The expanding jet interacting with the plate downstream

leads to the formation of a bow shock.[38] Due to the complicated nature of supersonic flow fields, stagnation pressure, backpressure and the formation of a bow shock, theoretical treatments of supersonic and hypersonic impactors are rare.[38]

2.5.2 – Nanoparticle Jet Impactor Experimental Schematic

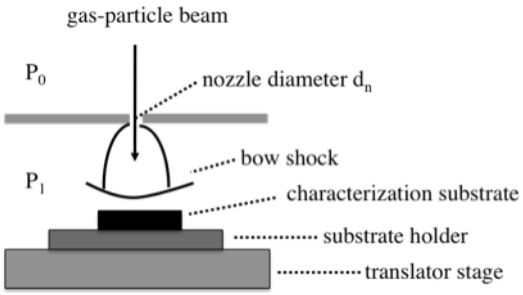

Figure 2.17: Nanoparticle jet impactor. P_0 is ambient pressure while P_1 is ~25 torr.

Figure 2.17 shows a detailed schematic of the in-house designed nanoparticle jet impactor, which is based on the design of De La Mora et al.[33] The gas-particle beam is expanded into an evacuated region (P_1 ~25 torr) through a (d_n = 200 μm) pinhole where a substrate for impaction is located 5 mm downstream. The particle beam is directed into the jet impactor at 400 SCCM and a fraction of this flow is vented before encountering the pinhole. The jet impactor pump rate is determined by the pinhole size, which was measured to be 330 SCCM. The characterization substrate is attached to the substrate holder via carbon tape and can easily be removed from the translator stage for analysis of impacted nanoparticle material. Figure 2.18 shows an operational schematic of the ENG with the nanoparticle jet impactor. Figure 2.19 is a photograph of the nanoparticle jet impactor.

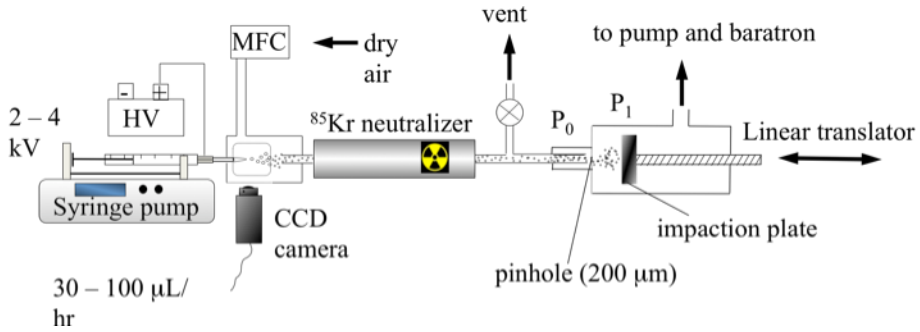

Figure 2.18: Operational schematic of the electrospray nanoparticle source and nanoparticle het impactor. Key: MFC = mass flow controller, HV = high voltage, P_0 = ambient pressure, P_1 = ~25 torr.

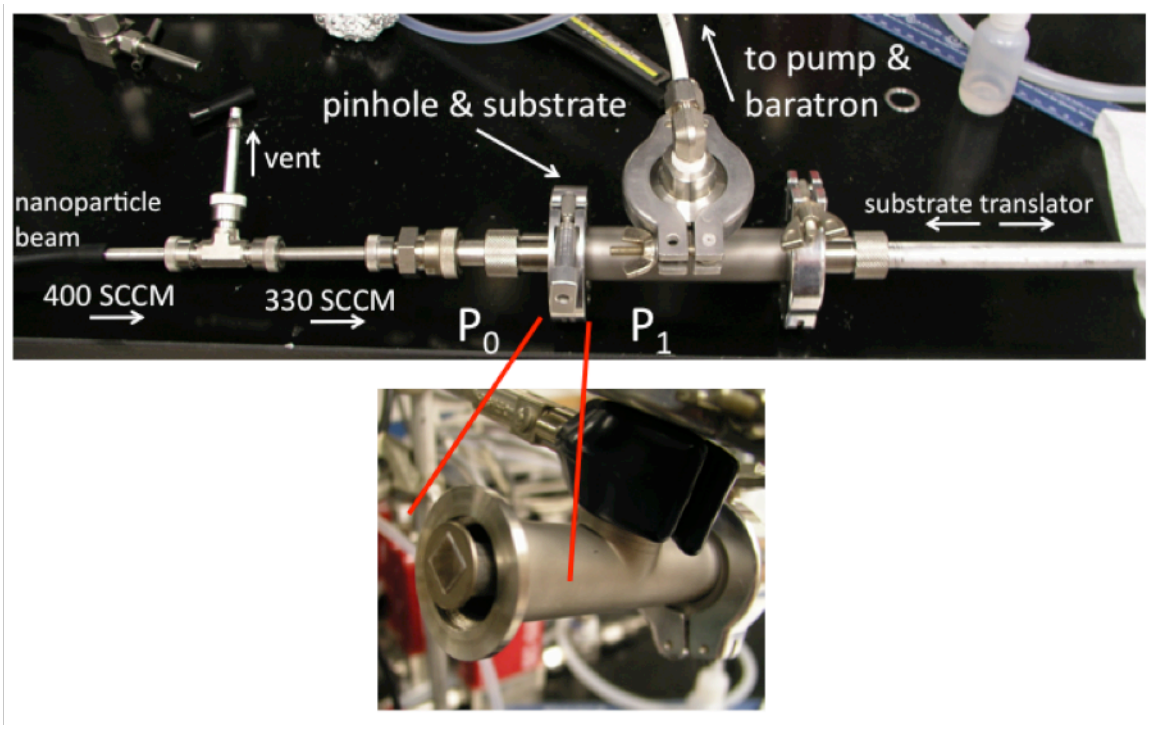

Figure 2.19: A photograph of the nanoparticle jet impactor.

Section 2.6 – *Analytical Tools and Methodologies for Morphological and Chemical Characterization of SDS/NaCl Nanoparticles*

2.6.1 – X-ray Photoelectron Spectroscopy

X-ray photoelectron spectroscopy (XPS) analysis (VG Scientific LTD) was carried out on the full particle distribution (see Table 2.2) emerging directly from the electrospray particle source as depicted in Figure 2.18 for each composition to maximize XPS signal. Nanoparticles were impacted on highly ordered pyrolytic graphite (HOPG) for roughly 6 hours, after which time a ring approximately 0.5 mm in diameter was visible on the substrate surface. Figure 2.20 shows a photograph of a ring of impacted nanoparticle material on a HOPG substrate in the load lock compartment of the XPS chamber.

In XPS, a sample is irradiated with high-energy x-ray photons, which are energetic enough to expel core level electrons from chemical moieties in a molecule. Core level electrons are chemically sensitive to environment, thus a metallic sulfur atom will look much different

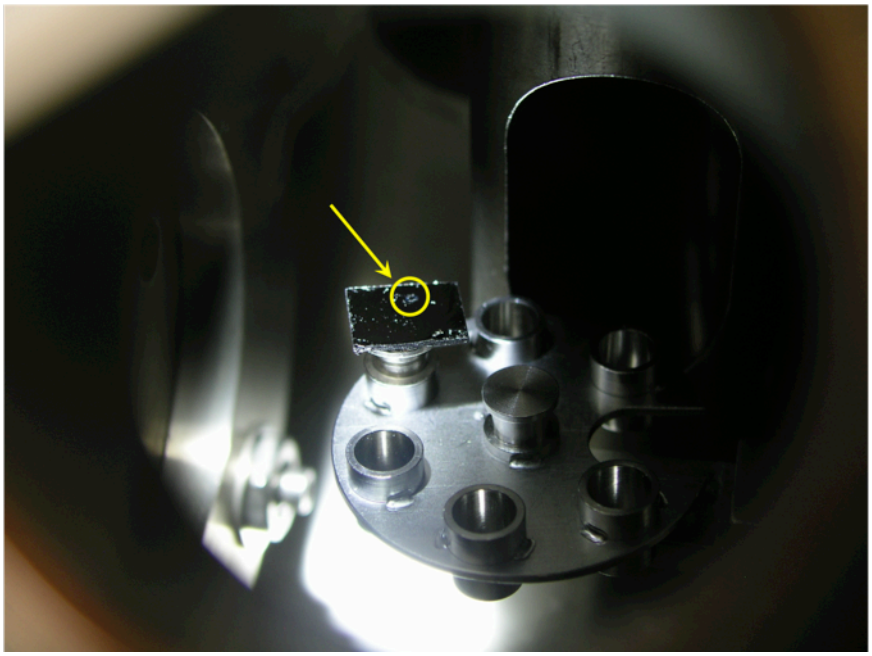

Figure 2.20: A ring of impacted nanoparticle material on a graphite substrate in the load lock compartment of the XPS chamber.

than an oxidized sulfur atom in XPS. After a sample absorbs an x-ray, a core level electron (sometimes called a photoelectron) is expelled into a vacuum (typically nano-torr) with a certain amount of kinetic energy. The energy of the x-ray photon ($E_{h\nu}$) is equal to the binding energy of the core electron plus the kinetic energy that it leaves the sample with. Equation 2.20 demonstrates this, where $V_{electron}$ is potential energy of the core electron (or binding energy) and $T_{electron}$ is kinetic energy of the photoelectron.

$$E_{h\nu} = V_{electron} + T_{electron} \qquad (2.20)$$

The XPS experiments were carried out under ultra-high vacuum conditions (1-4 nano-torr) and incident photons were generated from an Al source operating at 14 kV and 34 mA. The HOPG substrate was attached to an XPS stub via carbon tape and translated such that the nanoparticle ring was centered directly under the optimized position of the energy analyzer. An energy analyzer pass energy of 20 eV was used for all experiments. This essentially forces electrons into a tighter path in the hemispherical energy analyzer region, which reduces

resolution but enhances sensitivity. Sulfur S(2p) photoelectrons and chlorine Cl(2p) photoelectrons were analyzed as proxies for SDS and NaCl respectively.

XPS is a surface sensitive technique. X-rays irradiate the entire depth of sample; however, photoelectrons are collected from a small depth in the sample due to inelastic scattering of photoelectrons. The inelastic mean free path (IMFP) of an electron through NaCl with 1300 eV kinetic energy is roughly 3.5 nm.[39] The Al source produced 1456 eV photons and the binding energy of Cl(2p) is ~200 eV, thus the majority of electrons collected for NaCl would originate roughly 3.5 nm deep into the sample if no SDS existed on the surface of the NaCl nanoparticles. IMFP through aliphatic chains is roughly 4.0 nm for an electron which has 1300 eV kinetic energy.[40] The binding energy of S(2p) is ~170 eV; therefore photoelectrons could be collected through an SDS film thickness of ~4.0 nm.

2.6.2 – Transmission Fourier Transform Infrared Spectroscopy

Samples of SDS/NaCl nanoparticle material were impacted on ZnSe windows and were monitored using standard transmission Fourier transform infrared (FTIR) spectroscopy, which will not be reviewed herein. Infrared spectra were collected over the spectral range of interest, 4000 – 650 cm^{-1}, as single beam spectra at 4 cm^{-1} resolution using 2560 scans for both background and sample spectra, respectively, using a Nicolet AVATAR FTIR (now Thermo Electron Corp. Madison, WI). Infrared absorbance spectra were obtained by ratioing the single beam spectra of the deposited nanoparticle material to the background spectrum of a clean ZnSe window. The entire particle distribution was used (TABLE 2.2, Figure 2.18) and impaction time for FTIR analysis was also ~6 hours, after which time a visible ring was present on the ZnSe window. A slightly different substrate holder was used to collect nanoparticles for FTIR analysis. This holder is a metallic ring, which allowed the substrate to be placed on the translator stage without contaminating the backside of the ZnSe window. Impacted nanoparticle material sat in

the FTIR chamber for several days under dry conditions (<1% RH @ 295K) until rotational water bands were no longer visible and degassing of water had thus stopped.

2.6.3 – Atomic Force Microscopy Imaging

Atomic focrce microscopy (AFM), which will not be reviewed herein, was used to characterize the morphology of SDS/NaCl nanoparticles. Samples of SDS/NaCl nanoparticle material impacted on HOPG or mica were imaged at ambient pressure and humidity using a Park Scientific Instruments AutoProbe CP Research (now Veeco Metrology Inc., Santa Barbara, CA) scanning probe microscope in intermittent contact mode. Impaction time was much shorter than samples prepared for XPS and FTIR analysis; where collection times of 30 – 45 minutes were typically employed. AFM images were acquired using highly doped silicon tips (BudgetSensors) with a force constant of 3 N/m in intermittent contact mode. The piezoelectric scanner (5 mm) was calibrated using a grating in the *xy* directions and in the *z* direction using several conventional height standards. Topographs were obtained as 256 × 256 pixels and were flattened line-by-line and analyzed using AutoProbe image processing software supplied by the manufacturer of the AFM.

References

(1) Hinds, W. C., *Aerosol Technology*, 2 ed.; John Wiley & Sons, Inc., **1998**.

(2) Cunningham, E., **"On the Velocity of Steady Fall of Spherical Particles Through Fluid Medium."**. *Proceedings of the Royal Society of London Series a-Containing Papers of a Mathematical and Physical Character* **1910**, *83*, 357.

(3) Allen, M. D.; Raabe, O. G., **"Slip Correction Measurements of Spherical Solid Aerosol Particles in an Improved Millikan Apparatus"**. *Aerosol Science and Technology* **1985**, *4*, 269.

(4) DeCarlo, P.; Slowik, J.; Worsnop, D.; Davidovits, P.; Jimenez, J., **"Particle Morphology and Density Characterization by Combined Mobility and Aerodynamic Diameter Measurements. Part 1: Theory"**. *Aerosol Science and Technology* **2004**, *38*, 1185.

(5) Alshawa, A.; Dopfer, O.; Harmon, C. W.; Nizkorodov, S. A.; Underwood, J. S., **"Hygroscopic Growth and Deliquescence of NaCl Nanoparticles Coated with Surfactant AOT"**. *Journal of Physical Chemisry A* **2009**.

(6) Dahneke, B. E., **"Slip Correction Factors for Nonspherical Bodies—I: Introduction and Continuum Flow"**. *Journal of Aerosol Science* **1973**, *4*, 139.

(7) Dahneke, B. E., **"Slip Correction Factors for Nonspherical Bodies—II: Free Molecule Flow"**. *Journal of Aerosol Science* **1973**, *4*, 147.

(8) Dahneke, B. E., **"Slip Correction Factors for Nonspherical Bodies—III the Form of the General Law"**. *Journal of Aerosol Science* **1973**, *4*, 163.

(9) Fenn, J. B.; Mann, M.; Meng, C. K.; Wong, S. F.; Whitehouse, C. M., **"Electrospray Ionization for Mass Spectrometry of Large Biomolecules"**. *Science* **1989**, *246*, 64.

(10) Rulison, A.; Flagan, R. C., **"Electrospray Atomization of Electrolytic Solutions"**. *Journal of Colloid and Interface Science* **1994**, *167*, 135.

(11) Biskos, G.; Malinowski, A.; Russell, L.; Buseck, P.; Martin, S., **"Nanosize Effect on the Deliquescence and the Efflorescence of Sodium Chloride Particles"**. *Aerosol Science and Technology* **2006**, *40*, 97.

(12) Biskos, G.; Paulsen, D.; Russell, L. M.; Buseck, P. R.; Martin, S. T., **"Prompt Deliquescence and Efflorescence of Aerosol Nanoparticles"**. *Atmospheric Chemistry and Physics* **2007**, *6*, 4633.

(13) Biskos, G.; Russell, L. M.; Buseck, P. R.; Martin, S. T., **"Nanosize Effect on the Hygroscopic Growth Factor of Aerosol Particles"**. *Geophys. Res. Lett.* **2006**, *33*, L07801.

(14) Romakkaniemi, S.; Haemeri, K.; Vaekevae, M.; Laaksonen, A., **"Adsorption of Water on 8-15 nm NaCl and $(NH_4)_2SO_4$ Aerosols Measured Using an Ultrafine Tandem Differential Mobility Analyzer"**. *Journal of Physical Chemistry A* **2001**, *105*, 8183.

(15) Hameri, K.; Vakeva, M.; Hansson, H.-C.; Laaksonen, A., **"Hygroscopic Growth of Ultrafine Ammonium Sulphate Aerosol Measured Using an Ultrafine Tandem Differential Mobility Analyzer"**. *Journal of Geophysical Research* **2000**, *105*, 22231.

(16) Hameri, K.; Laaksonen, A.; Vakeva, M.; Suni, T., **"Hygroscopic Growth of Ultrafine Sodium Chloride Particles"**. *Journal of Geophysical Research* **2001**, *106*, 20749.

(17) Hameri, K.; Charlson, R. J.; Hansson, H.-C.; Jacobson, M., **"Hygroscopic Properties of Ammonium Sulfate Aerosols Mixed with Slightly Soluble Organic Compound"**. *Journal of Aerosol Science* **1997**, *28*, S153.

(18) Hameri, K.; Charlson, R.; Hansson, H.-C., **"Hygroscopic Properties of Mixed Ammonium Sulfate and Carboxylic Acids Particles"**. *Aiche Journal* **2002**, *48*, 1309.

(19) Cole, R. B., *Electrospray Ionization Mass Spectrometry* John Wiley & Sons Inc: New York, NY, **1997**.

(20) Rader, D. J.; McMurry, P. H., **"Application of the Tandem Differential Mobility Analyzer to Studies of Droplet Growth or Evaporation"**. *Journal of Aerosol Science* **1986**, *17*, 771.

(21) Chen, D. R.; Pui, D. Y. H.; Hummes, D.; Fissan, H.; Quant, F. R.; Sem, G. J., **"Design and Evaluation of a Nanometer Aerosol Differential Mobility Analyzer (Nano-DMA)"**. *Journal of Aerosol Science* **1998**, *29*, 497.

(22) Agarwal, J. K.; Sem, G. J., **"Continuous-Flow, Single-Particle-Counting Condensation Nucleus Counter"**. *Journal of Aerosol Science* **1980**, *11*, 343.

(23) Mcdermott, W. T.; Ockovic, R. C.; Stolzenburg, M. R., **"Counting Efficiency of an Improved 30-a Condensation Nucleus Counter"**. *Aerosol Science and Technology* **1991**, *14*, 278.
(24) Stolzenburg, M. R.; Mcmurry, P. H., **"An Ultrafine Aerosol Condensation Nucleus Counter"**. *Aerosol Science and Technology* **1991**, *14*, 48.
(25) Liu, B. Y. H.; Pui, D. Y. H., **"Submicron Aerosol Standard and Primary, Absolute Calibration of Condensation Nuclei Counter"**. *Journal of Colloid and Interface Science* **1974**, *47*, 155.
(26) Kesten, J.; Reineking, A.; Porstendorfer, J., **"Calibration of a Tsi-Model-3025 Ultrafine Condensation Particle Counter"**. *Aerosol Science and Technology* **1991**, *15*, 107.
(27) Iida, K.; Stolzenburg, M. R.; McMurry, P. H.; Smith, J. N.; Quant, F. R.; Oberreit, D. R.; Keady, P. B.; Eiguren-Fernandez, A.; Lewis, G. S.; Kreisberg, N. M.; Hering, S. V., **"An Ultrafine, Water-Based Condensation Particle Counter and its Evaluation Under Field Conditions"**. *Aerosol Science and Technology* **2008**, *42*, 862.
(28) Hering, S. V.; Stolzenburg, M. R.; Quant, F. R.; Oberreit, D. R.; Keady, P. B., **"A Laminar-Flow, Water-Based Condensation Particle Counter (WCPC)"**. *Aerosol Science and Technology* **2005**, *39*, 659.
(29) Wiedensohler, A.; Hansson, H. C.; Keady, P. B.; Caldow, R., **"Experimental-Verification of the Particle-Detection Efficiency of Tsi-3025 Ucpc"**. *Journal of Aerosol Science* **1990**, *21*, S617.
(30) Ensor, D. S.; Viner, A. S.; Johnson, E. W.; Donovan, R. P.; Keady, P. B.; Weyrauch, K. J., **"Measurement of Ultrafine Aerosol-Particle Size Distributions at Low Concentrations by Parallel Arrays of a Diffusion Battery and a Condensation Nucleus Counter in Series"**. *Journal of Aerosol Science* **1989**, *20*, 471.
(31) Bartz, H.; Fissan, H.; Helsper, C.; Kousaka, Y.; Okuyama, K.; Fukushima, N.; Keady, P. B.; Kerrigan, S.; Fruin, S. A.; Mcmurry, P. H.; Pui, D. Y. H.; Stolzenburg, M. R., **"Response Characteristics for 4 Different Condensation Nucleus Counters to Particles in the 3-50 Nm Diameter Range"**. *Journal of Aerosol Science* **1985**, *16*, 443.
(32) Tang, I. N.; Tridico, A. C.; Fung, K. H., **"Thermodynamic and Optical Properties of Sea Salt Aerosols"**. *Journal of Geophysical Research-Atmospheres* **1997**, *102*, 23269.
(33) De La Mora, J. F.; Hering, S. V.; Rao, N.; Mcmurry, P. H., **"Hypersonic Impaction of Ultrafine Particles"**. *Journal of Aerosol Science* **1990**, *21*, 169.
(34) Turner, J. F. http://www.appliedphysicsusa.com/nano_moudi_impactor.html; API, Ed. Newit, CO.
(35) Dixkens, J.; Fissan, H., **"Development of an Electrostatic Precipitator for off-line Particle Analysis"**. *Aerosol Science and Technology* **1999**, *30*, 438.
(36) Rao, N. P.; Tymiak, N.; Blum, J.; Neuman, A.; Lee, H. J.; Girshick, S. L.; McMurry, P. H.; Heberlein, J., **"Hypersonic Plasma Particle Deposition of Nanostructured Silicon and Silicon Carbide"**. *Journal of Aerosol Science* **1998**, *29*, 707.
(37) Ude, S.; Fernandez de la Mora, J., **"Hypersonic Impaction with Molecular Mass Standards"**. *Journal of Aerosol Science* **2003**, *34*, 1245.
(38) Abouali, O.; Ahmadi, G., **"A Model for Supersonic and Hypersonic Impactors for Nanoparticles"**. *Journal of Nanoparticle Research* **2005**, *7*, 75.
(39) Tanuma, S., **"Calculations of Electron Inelastic Free Paths in Au-Cu and Au-Ag Alloys"**. *Bunseki Kagaku* **1991**, *40*, 667.
(40) Cumpson, P. J., **"Estimation of Inelastic Mean Free Paths for Polymers and other Organic Materials: use of Quantitative Structure-Property Relationships"**. *Surface and Interface Analysis* **2001**, *31*, 23.

Chapter 3 – Hygroscopic Growth and Deliquescence of NaCl Nanoparticles

Section 3.1 – *Size Effects on Deliquescence Relative Humidity and Mobility Growth Factor*

3.1.1 – Hygroscopic Growth Curves

Sodium chloride was used as a test case to evaluate the tandem nano-DMA experimental apparatus due to the numerous studies on NaCl nanoparticles, aerosols, and surfaces.[1-10]

Figure 3.1(a)-(d) shows the mobility hygroscopic growth curves for NaCl nanoparticles with mobility diameters of 9, 11, 14, and 17 nm, respectively for 1 s humidity exposure. The dashed lines in Figure 3.1 indicate the predicted DRH values from the empirical power law determined by Biskos et al.[1] The observed values of DRH are in good agreement with the previous measurements; the deviations are within the accuracy of the RH probes. We were also able to confirm the discrete nature of deliquescence of NaCl nanoparticles (reported in Figure 2 of Ref. 2), wherein a bimodal particle size distribution is observed in the immediate vicinity of the deliquescence transition (discussed further below). Humidity exposure time did not make a difference for DRH determination of NaCl nanoparticles.

Figure 3.1(e)-(h) shows the shape corrected growth factors for d_m = 9, 11, 14, and 17 nm NaCl particles, respectively, with special attention paid to the region immediately before the deliquescence point. GF_m were converted into effective coverage of water (Θ_w) by using equation 1.12 and assuming water coverage layers are spherical shells (discussed further below).

Present measurements also confirm that post-deliquescence GF_m (that is, GF_m measured above the DRH point) decrease with decreasing dry diameter as a consequence of the Kelvin effect.[3] TABLE 3.1 shows the mobility GF_m for NaCl nanoparticles at 80% RH, when

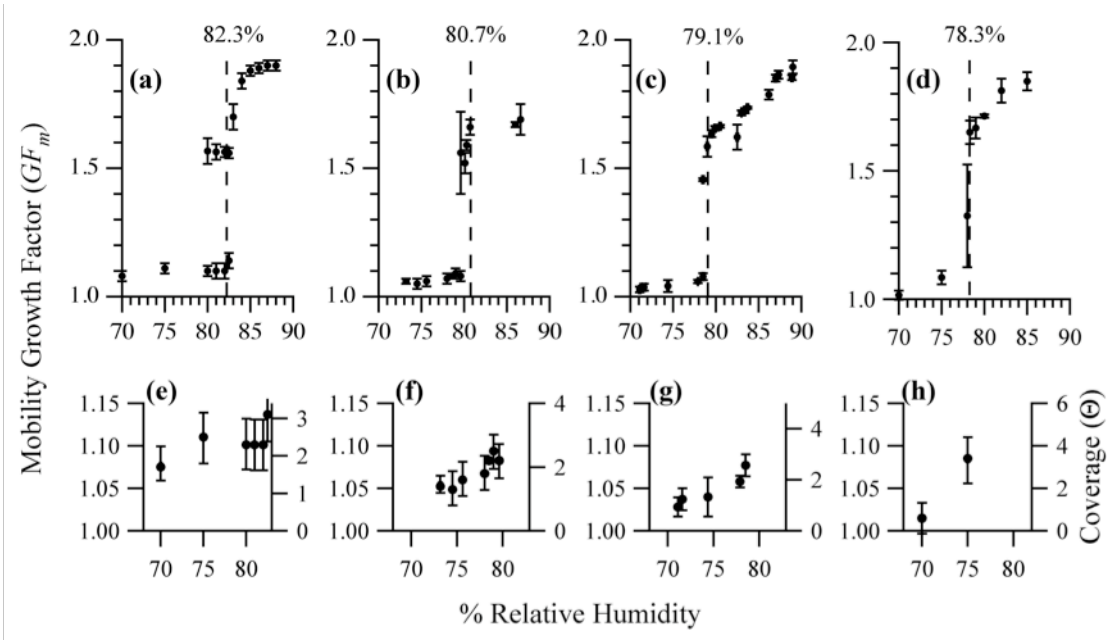

Figure 3.1: Hygroscopic growth curves (2σ errors from repeat measurements) of pure NaCl nanoparticles: d_m = **(a)** 9 nm; **(b)** 11 nm; **(c)** 14 nm; **(d)** 17 nm. Special attention is given to the region before deliquescence for d_m = 9, 11, 14, 17 nm particles in panels **(e**), **(f), (g), (h),** respectively. Water monolayer coverage was calculated from the GF values as described in the text. The dashed lines are calculated DRH from Ref. 1. RH exposure time is 1 s.

TABLE 3.1: Nanosize Effects on GF_m of NaCl Nanoparticles at 80% RH

d_m (nm)	GF_m [a]	GF_m [b]
6		1.45[c]
8		1.55[c]
9	1.57 ± 0.05	
10		1.55[c]
11	1.52 ± 0.04	
14	1.66 ± 0.01	
15		1.68
17	1.71 ± 0.01	
20		1.71
30		1.74
40		1.76
60		1.75
∞		1.84

[a] This work; 2σ error bars result from averaging repeated measurements

[b] From Biskos et al.[3]

[c] Growth factor on the efflorescence branch measured in vicinity of 80% RH[3]

particles are already deliquesced. Within the experimental uncertainties, the GF values measured in this work for 9, 11, 14, and 17 nm particles, and in Ref. 3 for 6, 8, 10, 15, 20, 30, 40,

and 60 nm particles, increase monotonically with the particle mobility diameter. In summary, our tandem nano-DMA instrument correctly reproduces the shapes of the growth curves and the GF_m values for NaCl nanoparticles. Humidity exposure time did not affect the GF_m determination of NaCl nanoparticles.

3.1.2 – Mobility Histograms

Figure 3.2 shows representative mobility histograms of size selected NaCl nanoparticles at various levels of humidity for 1 s exposure. The dashed line in Figure 3.2 indicates the initial dry size selected diameter at 7.0% RH, which is 14.0 ± 0.2 nm. Mobility histograms have been fit

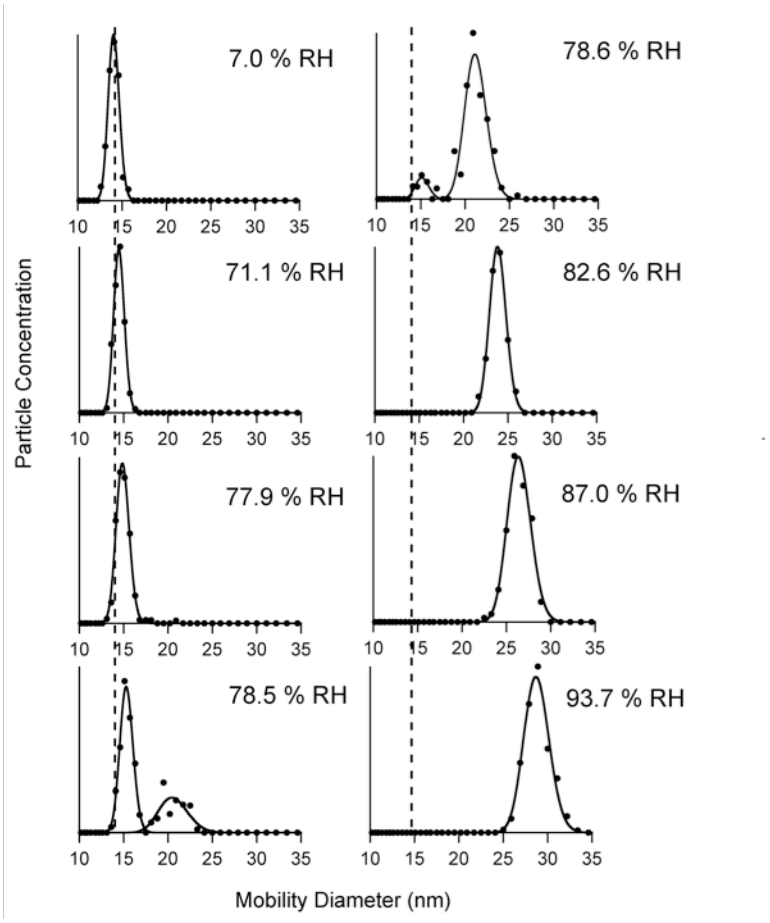

Figure 3.2: Mobility histograms of size selected 14.0 ± 0.2 nm NaCl particles corresponding to the growth curve in Figure 3.1(c). Mobility histograms have been fit with lognormal curves.

with lognormal distributions. As 14 nm NaCl particles take on a thin film of water prior to deliquescence, they grow slightly past the dashed line indicated in mobility histograms. In the vicinity of 14 nm NaCl DRH, 79.1 ± 1.0% RH,[1] a bimodal distribution of particle sizes is observed. This corresponds to the co-existence of a wetted, crystalline population of particles and a dissolved, aqueous droplet population of particles, which are both thermodynamically stable at the deliquescence point. Once the ambient humidity is increased slightly, the dissolved, aqueous nanodroplets prevail and grow expansively in size as they take up more water due to humidity exposure. Figure 3.1(c) shows the corresponding hygroscopic growth curve from the mobility histograms presented in Figure 3.2(a), where the dashed line indicates 14 nm NaCl DRH.[3] As can be seen in Figure 3.1(c) and 3.2, hygroscopic growth increases considerably after the deliquescence point.

Section 3.2 – *Pre-Deliquescent Wetting of NaCl Nanoparticles*

3.2.1 – Converting Mobility Growth Factor into Water Coverage Layer

Crystalline NaCl (bulk) is known to uptake 3.5-4.0 MLs of water at humidities just below 75.4% RH at room temperature and pressure.[5-7] The same should hold true for NaCl particles larger than 100 nm; however the GF_m of a 100 nm particle with 3.5-4.0 MLs of water is roughly 1.01 under the same experimental DMA conditions employed in this work. Quantification of ML coverage on large (> 100 nm) NaCl particles is therefore difficult in a tandem DMA experiment as mobility diameter bandwidths are proportional to the ratio of the aerosol flow and sheath flow (~0.1d_m). The GF_m of a 10 nm particle with 3.5-4.0 ML is roughly 1.10, which is well above the threshold for repeat measurements in experimental conditions employed in this work (GF_m ± 0.02). ML coverage on particles smaller than 100 nm is expected to be less than bulk NaCl due to the Kelvin effect; however, few measurements are available which support this.

Mobility growth factors were converted into water coverage layer by using equation 1.12. Surface concentration of adsorbed water, S_w, can be calculated from d_m.

$$S_w = \frac{N_w}{\pi\, d_m{}^2} = \frac{\rho_w \Delta V_m}{\pi\, d_m{}^2} = \frac{1}{6}\rho_w d_m\left(GF_m^3 - 1\right) \qquad (3.1)$$

In equation 3.1, N_w is the total number of adsorbed water molecules, ρ_w is the density of adsorbed water (33 molec nm^{-3}), and ΔV_m is the particle volume change due to the water adsorption.

Dry NaCl particles have a cubic shape,[4] whereas the deliquesced NaCl particles are spherical. It is unclear what kind of shape a crystalline NaCl nanoparticle with a few MLs of adsorbed surface water will have. As an approximation, particles are regarded as spherical and consequently water coverage layers are the addition of spherical shells. The measured mobility diameters of dry NaCl particles (d_m) were converted into diameters of envelope-equivalent spheres (d_e) using equation 3.2. The parameter $A(Kn,\chi)$ is a function of Knudsen number (Kn) and shape factor (χ) in the appropriate flow regime, which is the same solution to equation 2.12 and the results presented in TABLE 2.1. Parameter $A(Kn,\chi)$ is a collection of all the iterative steps taken to solve equation 2.12.

$$d_e(0) = d_m(0)\cdot A(Kn,\chi) \qquad (3.2)$$

Thus, rearrangement of equation 3.1, including the definition of a water coverage layer (eq. 1.12), and incorporating equation 3.2 for mobility diameter leads to equation 3.3.

$$GF_m(RH) = \left[\left(\frac{6\cdot S_{NaCl}\cdot A^3(Kn,\chi)}{\rho_w \cdot d_e(0)}\right)\cdot \Theta_w(S) + 1\right]^{1/3} \qquad (3.3)$$

3.2.2 – Comparison of Data to Standard Adsorption Isotherms

Equation 3.3 is a means for plotting any standard adsorption isotherm in growth space. Using equations 1.13-1.15 for $\Theta(S)$ in equation 3.3, one can plot the BET isotherm in growth

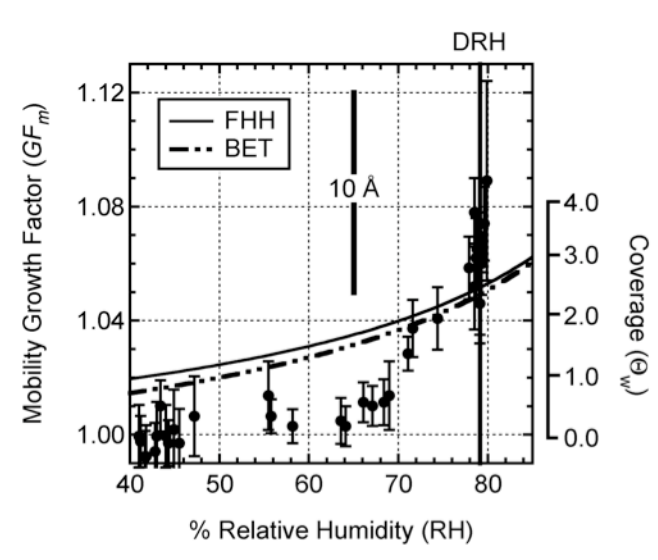

Figure 3.3: Standard adsorption isotherms compared to measured mobility growth factors of 14 nm NaCl particles. Error bars are 2σ from repeat measurements.

space and using equations 1.14, 1.16 and 1.17 for $\Theta(S)$ in equation 3.3 will plot the FHH isotherm in growth space. Figure 3.3 shows the BET and FHH isotherm plotted in growth space in comparison to measured mobility growth factors of 14 nm NaCl particles. In Figure 3.3 the envelope equivalent diameter is $d_e(0)$ = 12.6 nm and shape correction is $A(Kn,\chi_v)$ = 0.898. Appropriate FHH (A = 0.96, B = 1) and BET (c = 1.5) constants are used for water adsorption on NaCl(001).[7,8,11,12] The bulk density of water (997.1 g cm^{-3}) is converted to the molecular scale (33 nm^{-3}) for ρ_w^{molec}.

As can be seen in Figure 3.3, there is reasonable agreement in measured GF_m of 14 nm NaCl particles with equation 3.3 in the region corresponding to $3.0 > \Theta_w > 1.5$ ($1.06 > GF_m > 1.02$) occurring at roughly 70% RH. This is not surprising as $GF_m > 1.02$ represents measurements just above the threshold for repeat measurements under the

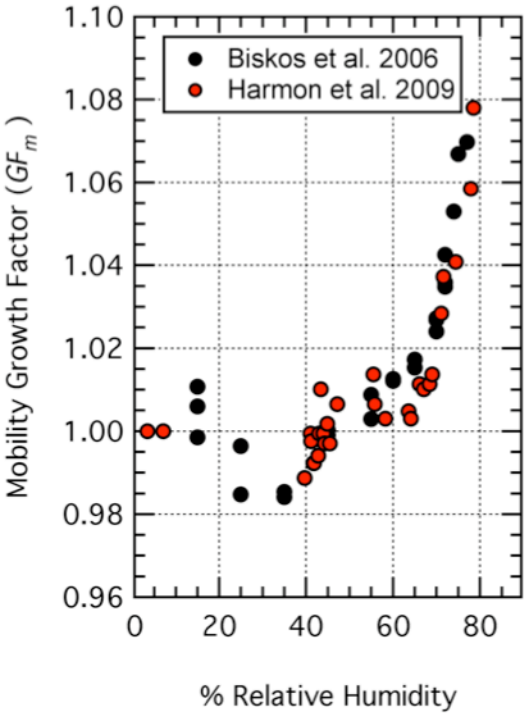

Figure 3.4: Pre-deliquescent growth of 14 nm NaCl particles compared to 15 nm NaCl particles from Biskos et al.[1] Error bars have been removed for clarity.

employed experimental conditions in this work. In the case of NaCl, measured GF_m are less than 1.00 under conditions near ~40% RH. This is attributed to dynamic reshaping of NaCl nanoparticles upon interaction of initially adsorbed surface water where Θ_w << 1.0 ML. Figure 3.4 shows a more detailed view of the pre-deliquescent growth region of 14 nm NaCl particles, where error bars have been removed for clarity and data provided from Biskos et al.[1] of 15 nm NaCl particles are shown for comparison. There is excellent agreement between our data and that of Biskos et al.[1].

Recent in situ ambient pressure XPS and Kelvin probe microscopy (KPM) studies[13] have revealed near ~40% RH the insulating NaCl(001) surface becomes slightly discharged due to induced ion mobility on the surface. KPM images reveal step-edge mobility and terrace ionic solvation occurs at RH > 35% and this is attributed to the onset of large scale restructuring of the NaCl(001) surface upon interaction with adsorbed water.[14] At ~50% RH the surface is smooth and completely discharged.[13] Measurements of hygroscopic growth in the vicinity of this region (~40% RH) in this work are not reliably quantifiable; however, the lack of agreement between measured GF_m and those predicted by the model in equation 3.3 is not surprising. The parameter $A(Kn,\chi_v)$ assumes a direct reshaping of NaCl nanoparticles at constant RH, which is a mobility conversion of a cube to a sphere. Measurements from Ref. 13 reveal this is a dynamic reshaping as a function of RH, therefore when the measured GF_m are less than the predicted GF_m by equation 3.3 the particle can be thought of as a cube with rounded edges. When the measured data converge to agreement with the theory, the particles can be regarded as spherical, containing a multilayer of adsorbed surface water prior to deliquescence.

Equation 3.3 reveals at the DRH (79.1 % RH)[1] of 14 nm NaCl, the predicted coverage should be 2.4 MLs of adsorbed surface water according to the FHH isotherm and 2.3 MLs according to the BET isotherm. Measured GF_m (1 and 67 s RH exposure) are plugged into the

left hand side of equation 3.3 at the DRH (average of values between DRH ± 1% RH) and this analysis reveals an estimated surface coverage of Θ_w = 3.1 ± 0.5 MLs (propagation of 2σ error in measured GF_m) of adsorbed surface water on 14 nm NaCl particles. This result is quantitatively accurate from what would be predicted by the Kelvin effect when comparing equilibrium vapor pressures over bulk crystalline NaCl[7] and 14 nm NaCl aerosols (see equations 1.7 and 1.11). For example, 79.1% RH above a 14 nm particle surface is equivalent to 67.3% RH (20.0 mbar at 297K) above a bulk NaCl crystalline surface, which has roughly 3 MLs of adsorbed surface water.[7] The data points seen above Θ_w > 3.0 MLs (GF_m > 1.06) for NaCl nanoparticles are from mobility histograms which contained two mode diameters. Consequently, the error of Θ_w calculation is large in this region of the deliquescence point due to fluctuations of particles co-existing in a wetted crystalline state and dissolved droplet state. This detailed analysis provides a molecular picture of the NaCl nanoparticle surface, which is a particle containing a uniform multilayer of water prior to deliquescing.

Section 3.3 – *Post-Deliquescence Measurements and Modified Köhler Theory*

3.3.1 – Modified Köhler Theory

Köhler theory was derived and reviewed in Section 1.3.3 for sub-saturation situations. As demonstrated in Figure 1.9 and TABLE 3.1, the Kelvin effect works against hygroscopic growth. In other words, nanoparticles (< 100 nm) do not take up as much water as large (> 100 nm) particles do. Furthermore, NaCl particles are cubic[4] and upon uptake of water reshaping will also work against hygroscopic growth. Biskos et al.[3] constructed four Models of sub-saturation Köhler theory for NaCl nanoparticles and these models will be compared to 14 nm NaCl hygroscopic growth curves. Equation 3.4 shows modified Köhler Theory (MKT) and TABLE 3.2 summarizes what each MKT model entails.

$$GF_m = \left(\frac{100\rho_s}{w_t(a_w) \cdot \rho_{aq}(w_t(a_w))} \right)^{1/3} \cdot A(Kn, \chi) \qquad (3.4)$$

TABLE 3.2: Modified Köhler Theory Models

Model [a]	$a_w(w_t)$	$A(Kn, \chi)$
1	Eq. 1.6 & 1.7	1.000
2	Eq. 1.7 & 1.11 [b]	1.000
3	Eq. 1.7 & 1.11 [b]	0.960 [c]
4	Eq. 1.7 & 1.11 [b]	0.898 [d]

[a] from Biskos et al.[3]
[b] Kelvin effect considerations for 14 nm NaCl
[c] continuum regime flow considerations
[d] free molecular regime flow considerations (14 nm)

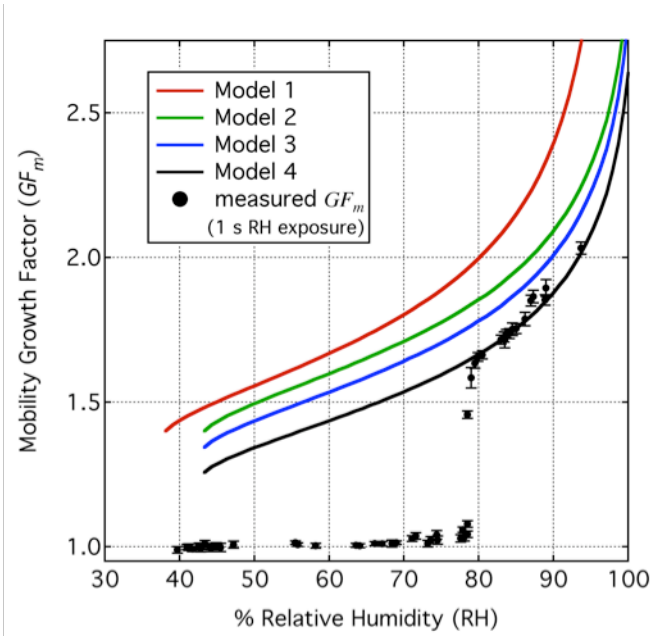

Figure 3.5: Models 1-4 from Biskos et al.[3] compared to measured 14 nm NaCl hygroscopic growth factors, 1 sec humidity exposure.

In Model 1, the shape correction parameter $A(Kn,\chi)$ is not considered nor is the Kelvin effect. Model 1 is the same plot as Figure 1.8 provided by equation 1.19 (deliquescence mode GF_m), which is relevant for very large spherical particles. Model 2 considers the Kelvin effect (14 nm NaCl); however, does not include a shape correction. Just as in the adsorption isotherm analysis, Models 3 and 4 both consider the Kelvin effect and shape correction. Model 3 uses continuum regime flow considerations and Model 4 uses free molecular regime flow considerations (14 nm). Figure 3.5 is a plot of Models 1-4 as well as measured 14 nm NaCl

hygroscopic GF_m for 1 second humidity exposure. As can be seen in Figure 3.5, there is excellent agreement with measured growth factor data and Model 4, which is expected given the prevailing considerations of the Kelvin effect and particle shape considerations in the free molecular flow regime. From this point forward, Model 4 from Biskos et al.[3] will be referred to as modified Köhler theory (MKT).

TABLE 3.1 demonstrates growth factors at 80% RH monotonically decrease with initial dry diameters. A more expansive analysis of MKT with varying nanoparticle diameter is shown in Figure 3.6, where MKT for d_m = 11, 14, and 17 nm is plotted along with measured GF_m data for the same sizes. It is clear from Figure 3.6 that the measured growth factor data monotonically decreases with initial dry mobility diameter. The differences in growth factors as predicted by MKT for varying size are very slight, smaller than the error bars in repeat measurements. From this, we are able to accurately measure the nanosize effect with respect to hygroscopic mobility growth factor for NaCl nanoparticles.

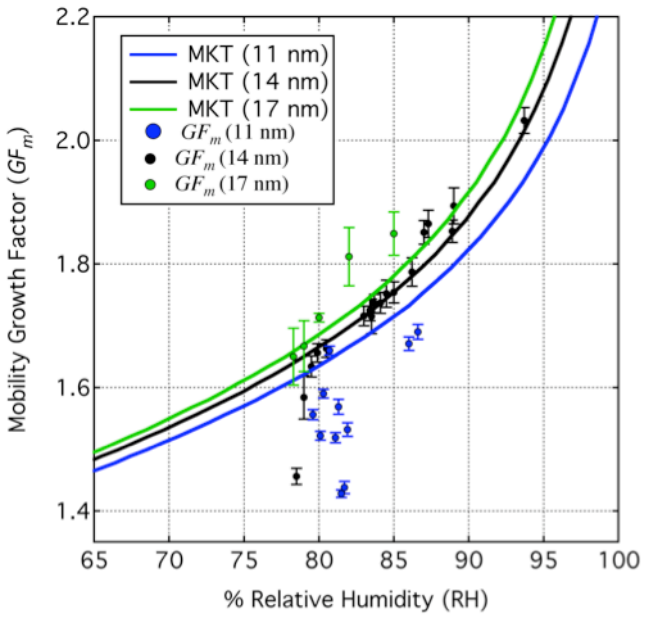

Figure 3.6: MKT for d_m = 11, 14 and 17 nm NaCl particles compared to measured GF_m data for d_m = 11, 14, and 17 nm NaCl particles.

3.3.2 – Nanosize effect on Activity-Solubility Relationships

The role of the Kelvin effect is often regarded as an increase in vapor pressure over a curved surface relative to a flat surface. There is also another consequence of the Kelvin effect, which are the relationships associated with activity-solubility presented in Section 1.2.4 and in

Figure 1.7. A saturated NaCl solution has a concentration of 26.5 w_t in water at 295 K,[15] which is also the concentration of a large (> 100 nm) NaCl droplet at the deliquescence point. Because nanoparticles take on less water overall as compared to large particles, upon deliquescence their saturation concentration should be greater. Figure 3.7 demonstrates this, which is a comparison of bulk activity-solubility (eq. 1.7) and calculated dissolved NaCl weight percent in 14 nm droplets from measured mobility growth factor data. Weight percent in 14 nm droplets was calculated by using equation 3.4 and solving for $w_t(a_w)$ with measured GF_m.

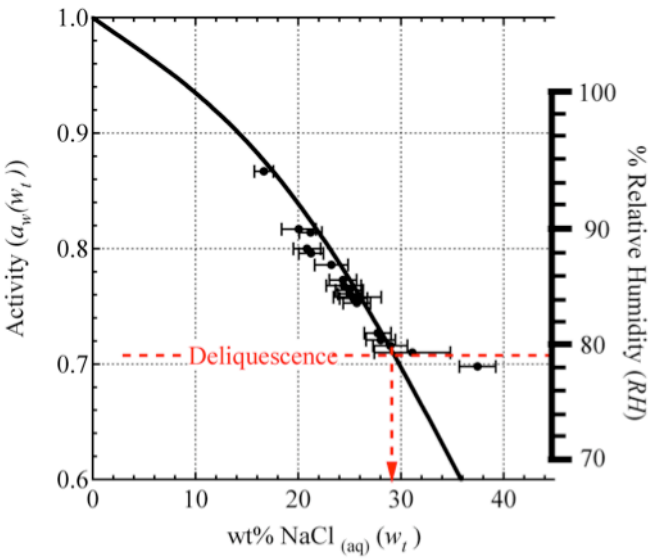

Figure 3.7: Bulk NaCl activity-solubility (eq. 1.7) compared to calculated dissolved NaCl weight percent in 14 nm droplets from measured mobility growth factors. The DRH (79.1% RH)[1] is indicated by the red dashed line.

The dashed line indicates the DRH of 14 nm NaCl particles[1] occurs at 79.1% RH, which is an equivalent activity of a_w = 0.71 over a bulk NaCl solution. Correspondingly, because an activity of 0.71 is less than the bulk equilibrium vapor pressure of a NaCl saturated solution (a_w = 0.75), 14 nm NaCl droplets have deliquescence compositions that are equivalent to a super saturated bulk NaCl solution. The red dashed arrow indicates this composition is 29.6 w_t in water at 295 K. A similar analysis for 11 and 17 nm NaCl droplets was also carried out and TABLE 3.3 shows those results. The error reported in dissolved NaCl weight percent is propagated from 2σ error in repeat measurements of growth factor. As can be seen in TABLE 3.3, deliquescence compositions are different for 11, 14, and 17 nm NaCl particles; however,

these differences are slight as the errors of calculations are similar in magnitude to the overall difference in composition for a given size.

TABLE 3.3: Activity-solubility Relationships of Dissolved NaCl Droplets at 295 K

Size	GF_m (DRH) [a]	DRH (% RH) [a]	w_t (%)	M (mol L^{-1})
∞	1.81 [b]	75.4 [b]	26.5 [b]	6.19 [b]
17 nm	1.65 ± 0.05	78.3 ± 1.0	28.7 ± 2.6	6.91 ± 0.63
14 nm	1.63 ± 0.02	79.5 ± 1.0	29.6 ± 1.1	7.22 ± 0.27
11 nm	1.59 ± 0.02	80.3 ± 1.0	31.7 ± 1.2	7.96 ± 0.30

[a] measured data in this work
[b] from Refs. 3, 15, and 16

Section 3.4 – *Conclusions of NaCl Nanoparticle Hygroscopic Growth*

A tandem nano-DMA apparatus was constructed and it was confirmed that it correctly captures the details of the hygroscopic growth curve of pure NaCl nanoparticles. The NaCl nanoparticles are observed to adsorb 1-4 MLs of water below DRH. At the DRH of 14 nm NaCl particles, there are 3.1 ± 0.5 ML of adsorbed surface water, which is consistent with the Kelvin effect when comparing a bulk NaCl surface to a 14 nm NaCl particle.[7] The deliquescence transitions in NaCl nanoparticles occur at well-defined DRH values. Two mode diameters are observed in the vicinity of NaCl DRH, which corresponds to the co-existence of a wetted nano-crystal and dissolved nano-droplet. Above NaCl DRH, the dissolved state prevails and nanoparticles take up water as predicted by MKT[3,16] with good agreement. The measured DRH values and growth factors are in quantitative agreement with previously published data.[1]

Interestingly, as the size of the particle decreases its deliquescence composition and DRH increases. Vapor pressure lowering is a colligative property; therefore as the amount of dissolved components increases in solution the equilibrium vapor pressure of the solution should decrease.[17] Quite the contrary, it is well accepted in our laboratory and others[1,3,8-10,18] as the size of the particle decreases, its equilibrium vapor pressure (or deliquescence point)

increases, despite the fact that the deliquescence composition increases with decreasing size. This is a consequence of the Kelvin effect which in itself is a consequence of the surface energy contributions to the Gibbs free energy of deliquescence.[10] These results demonstrate the importance of surface interactions when studying nano-scale objects, such as NaCl nanoparticles.

References

(1) Biskos, G.; Malinowski, A.; Russell, L.; Buseck, P.; Martin, S., **"Nanosize Effect on the Deliquescence and the Efflorescence of Sodium Chloride Particles"**. *Aerosol Science and Technology* **2006**, *40*, 97.

(2) Biskos, G.; Paulsen, D.; Russell, L. M.; Buseck, P. R.; Martin, S. T., **"Prompt Deliquescence and Efflorescence of Aerosol Nanoparticles"**. *Atmospheric Chemistry and Physics* **2007**, *6*, 4633.

(3) Biskos, G.; Russell, L. M.; Buseck, P. R.; Martin, S. T., **"Nanosize Effect on the Hygroscopic Growth Factor of Aerosol Particles"**. *Geophysical Research Letters* **2006**, *33*, L07801.

(4) Wise, M.; Biskos, G.; Martin, S.; Russell, L.; Buseck, P., **"Phase Transitions of Single Salt Particles Studied Using a Transmission Electron Microscope with an Environmental Cell"**. *Aerosol Science and Technology* **2005**, *39*, 849.

(5) Finlayson-Pitts, B. J.; Hemminger, J. C., **"Physical Chemistry of Airborne Sea Salt Particles and Their Components"**. *Journal of Physical Chemistry A* **2000**, *104*, 11463.

(6) Hemminger, J. C., **"Heterogeneous Chemistry in the Troposphere: A Modern Surface Chemistry Approach to the Study of Fundamental Processes"**. *International Review Physical Chemistry* **1999**, *18*, 387.

(7) Foster, M. C.; Ewing, G. E., **"Adsorption of Water on the NaCl(001) Surface. II. An Infrared Study at Ambient Temperatures"**. *Journal of Chemical Physics* **2000**, *112*, 6817.

(8) Romakkaniemi, S.; Haemeri, K.; Vaekevae, M.; Laaksonen, A., **"Adsorption of Water on 8-15 nm NaCl and $(NH_4)_2SO_4$ Aerosols Measured Using an Ultrafine Tandem Differential Mobility Analyzer"**. *Journal of Physical Chemistry A* **2001**, *105*, 8183.

(9) Hameri, K.; Laaksonen, A.; Vakeva, M.; Suni, T., **"Hygroscopic Growth of Ultrafine Sodium Chloride Particles"**. *Journal of Geophysical Research* **2001**, *106*, 20749.

(10) Russell, L. M.; Ming, Y., **"Deliquescence of Small Particles"**. *Journal of Chemical Physics* **2002**, *116*, 311.

(11) Adamson, A. W.; Gast, A. P., *Physical Chemistry of Surfaces*; John Wiley & Sons, **1997**; Vol. 6th.

(12) Gregg, S. J.; Sing, K. S. W., *Surface Area and Porosity*, 2 ed.; Academic Press: London, **1997**.

(13) Verdaguer, A.; Segura, J. J.; Fraxedas, J.; Bluhm, H.; Salmeron, M., **"Correlation between Charge State of Insulating NaCl Surfaces and Ionic Mobility Induced by Water Adsorption: A Combined Ambient Pressure X-ray Photoelectron Spectroscopy and Scanning Force Microscopy Study"**. *Journal of Physical Chemistry C* **2008**, *112*, 16898.

(14) Peters, A.; Wichmann, H. E.; Tuch, T.; Heinrich, J.; Heyder, J., **"Respiratory Effects are Associated with the Number of Ultrafine Particles"**. *American Journal of Respiratory and Critical Care Medicine* **1997**, *155*, 1376.

(15) Carper, J., **"The CRC Handbook of Chemistry and Physics"**. *Library Journal* **1999**, *124*, 192.

(16) Tang, I. N.; Tridico, A. C.; Fung, K. H., **"Thermodynamic and Optical Properties of Sea Salt Aerosols"**. *Journal of Geophysical Research-Atmospheres* **1997**, *102*, 23269.

(17) Raff, L. M., *Principles of Physical Chemistry*; Prentice Hall: Upper Saddle River, NJ, **2001**.

(18) Hameri, K.; Vakeva, M.; Hansson, H.-C.; Laaksonen, A., **"Hygroscopic Growth of Ultrafine Ammonium Sulphate Aerosol Measured Using an Ultrafine Tandem Differential Mobility Analyzer"**. *Journal of Geophysical Research* **2000**, *105*, 22231.

Chapter 4 – Hygroscopic Growth and Deliquescence of SDS/NaCl Nanoparticles

Section 4.1 – *Effect of SDS on Hygroscopic Properties of NaCl Nanoparticles and Bulk $NaCl_{(aq)}$ Mixtures*

4.1.1 – Hygroscopic Growth Curves of SDS/NaCl Nanoparticles

For the data on pure NaCl nanoparticles presented in Chapter 3, the present results corroborate the existing literature. The growth factors predicted by the MKT curve agree well with measured GF_m for pure NaCl particles following deliquescence at high RH. The DRH values predicted from an empirical DRH-size relationship for NaCl developed by Biskos et al.[1] are also in good agreement with the present observations of a sudden increase in GF_m attributed to deliquescence. As our tandem nano-DMA apparatus and humidity exposure/measurement setup is capable of reproducing previously established data, the next step is to study hygroscopic growth of SDS/NaCl particles. To the best of our knowledge, there is no data currently available on hygroscopic growth of SDS/NaCl nanoparticles smaller than 20 nm in diameter.

In the SDS/NaCl experiments, one mobility equivalent diameter (14.0 ± 0.2 nm) was chosen via mobility size selection for all of the SDS/NaCl compositions listed in TABLE 2.2. Each SDS/NaCl nanoparticle studied is therefore the same size, but should have a different SDS content. The final relative SDS/NaCl concentration in the nanoparticles is a function of the electrospray dynamics and is unknown a priori. Consequently, the various compositions of SDS/NaCl nanoparticles will be referred to by the solution composition from which they were generated and all values refer to the relative weight percents of SDS relative to NaCl. Following electrospray generation and size selection, nanoparticles are directed downstream for hygroscopic growth analysis.

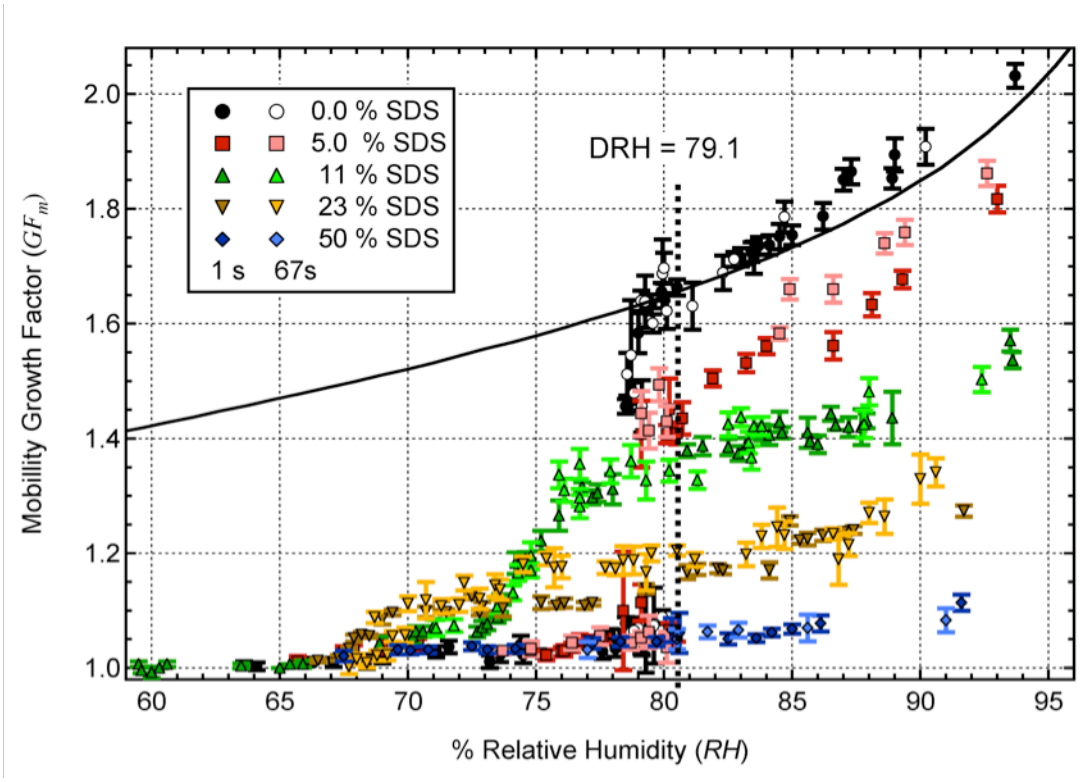

Figure 4.1: Hygroscopic growth curves of mobility equivalent diameter selected 14.0 ± 0.2 nm SDS/NaCl particles. The legend details wt/wt% of solutions that were electrosprayed. The DRH of 14 nm NaCl particles from reference 1 is indicated by the thick dotted line. The thick curve is a plot of the MKT Model 4. Labels 1 s and 67 s refer to the time the particles were exposed to RH before sizing. Error bars are 2σ from repeat measurements.

Figure 4.1 shows the measured hygroscopic growth curves for size selected 14.0 ± 0.2 nm particles containing variable amounts of SDS and NaCl. The legend details the composition of solutions that were electrosprayed (TABLE 2.2) as well as RH exposure time. The solid curve represents MKT (Model 4 in TABLE 3.2) and the dotted line shows the empirically determined DRH[1] of 14 nm NaCl particles. Figure 4.2(a-e) below shows each growth curve individually.

As the weight percent of SDS increases in the solutions used for making nanoparticles, GF_m are suppressed and the apparent location of DRH shifts to lower values of humidity in comparison to pure NaCl nanoparticles. Although growth factors are suppressed by the presence of SDS, the growth curves still have the same qualitative shape when compared to NaCl nanoparticles.

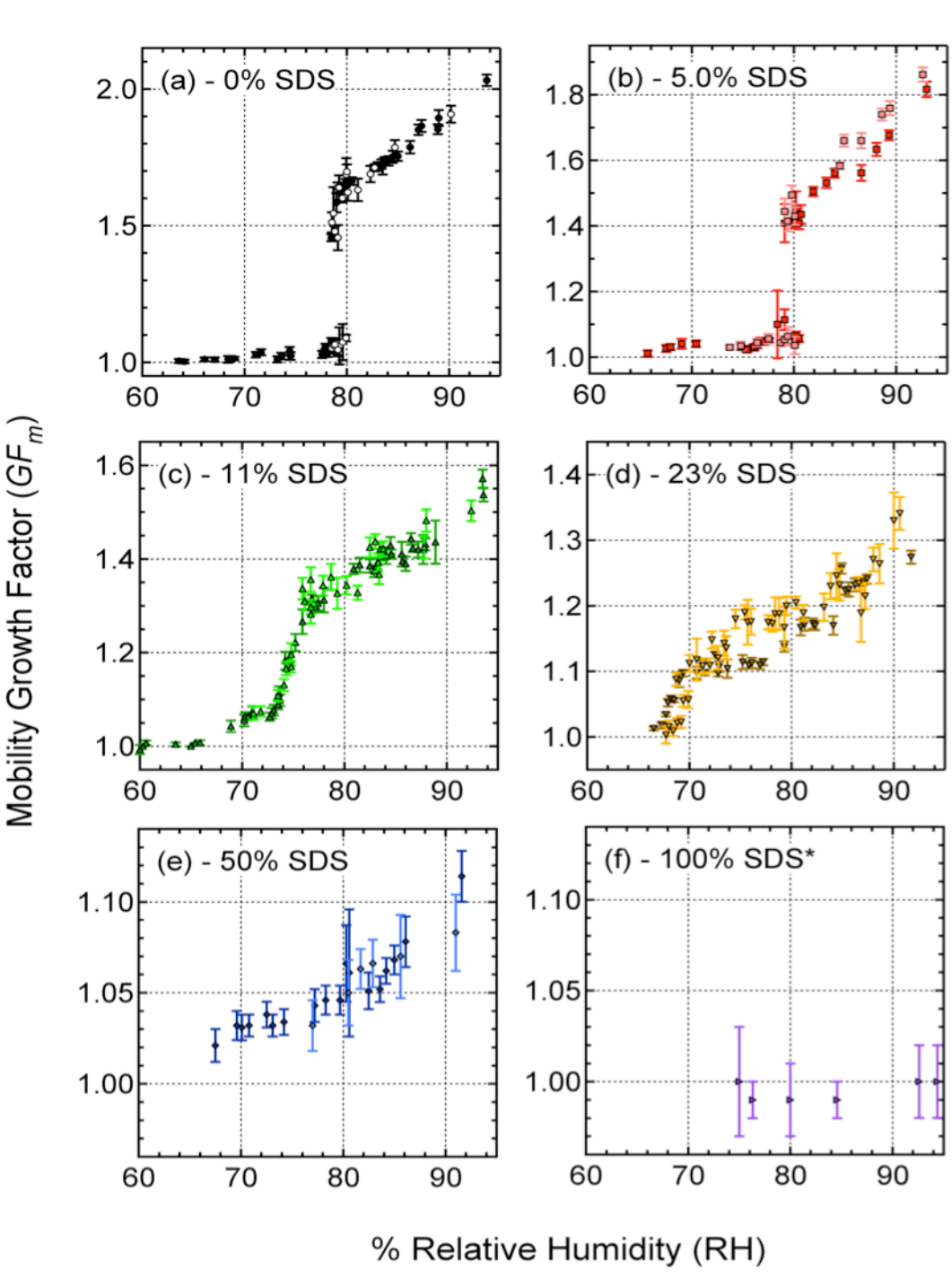

Figure 4.2: Individual hygroscopic growth curves of 14.0 ± 0.2 nm SDS/NaCl particles. See legend in Figure 4.1 for details. Error bars are 2σ calculated from repeat measurements. *Pure SDS data are not shown in Figure 4.1; humidity exposure time is 1 s and initial mobility equivalent diameter is 17.5 ± 0.1 nm.

Nanoparticles originating from the 5.0 wt/wt% SDS/NaCl solution display prompt deliquescence at the same RH value where pure NaCl nanoparticles deliquesce at 79.5 ± 1.0% RH. Prompt deliquescence is not observed for nanoparticles generated from solutions containing more than 5.0 wt/wt% SDS. Nanoparticles from the 11 wt/wt% SDS/NaCl system deliquesce between 73-77% RH and then display a growth curve that is qualitatively similar to pure NaCl nanoparticles, albeit at lower absolute GF_m. The nanoparticles from the 23 wt/wt% SDS/NaCl solution continue this trend but their growth curve has several unique features. For these nanoparticles, a fairly sharp growth region is observed between 68-71% RH, followed by a slower growth region until roughly 73% RH. Interestingly, there are indications of another sharp growth between 73-75% RH but only for the nanoparticles exposed to RH for 67 s. After that the particles appear to grow steadily with RH with the rate characteristic of fully deliquesced droplets. The nanoparticles from the 50 wt/wt% SDS/NaCl solution have greatly suppressed growth and the onset of deliquescence is difficult to discern. Pure SDS nanoparticles do not take up any measurable amount of water at humidities between 5-95% RH (GF_m < 1.02), which is consistent with measurements from this laboratory on pure AOT nanoparticles.[2] Nanoparticles from the 50 wt/wt% SDS/NaCl solution definitively take up more water in the 65-95% RH range than neat SDS nanoparticles do.

The differences in the growth curves obtained with different RH exposure times (1, 7, and 67 s) are either undetectable or very small. The hygroscopic growth for SDS/NaCl nanoparticles as well as NaCl nanoparticles must occur on time scales that are faster than experimentally measurable with a tandem nano-DMA setup. The differences observed are likely due to the range of analytical accuracy in measuring RH, which is ±1% between 0-90% RH and ±2 % RH between 90-100% RH.

4.1.2 – Mobility Histograms and Prompt Deliquescence in 5.0 wt/wt% SDS/NaCl Nanoparticles

Previously, "prompt" deliquescence was observed in studies of large NaCl particles (~100 nm) containing surfactants.[3,4] Here prompt deliquescence is defined as the co-existence of two thermodynamically stable phases, wetted crystalline and aqueous droplet, over a very narrow range of RH (≤ 1% RH). This co-existence manifests itself in a bimodal mobility equivalent diameter distribution in the vicinity of the DRH values, with the lower diameter corresponding to particles that have not yet deliquesced and larger diameter corresponding to the deliquesced aqueous droplets.[1] Once RH increases slightly the dry phase disappears in a very "prompt" manner, and only the aqueous particles remain.

Figure 3.2(a) demonstrates this bimodal size distribution in mobility histograms for 14 nm NaCl particles. Similarly, Figure 4.3 shows a representative bimodal mobility equivalent diameter distribution at 79.4% RH for the 5.0 wt/wt% SDS/NaCl nanoparticles exposed to 67 s of humidity. The data points shown in Figure 4.3 have been fit with two lognormal curves, which predict two mode diameters of 15.3 nm corresponding to the dry nanoparticles wetted with a few ML of water and 19.7 nm corresponding to the deliquesced nanoparticles. In this particular mobility histogram, the majority of the nanoparticles have deliquesced at 79.4% RH. Integration of each respective lognormal curve gives a good approximation of what fraction of the total amount of nanoparticles have deliquesced for a given mobility measurement. This analysis

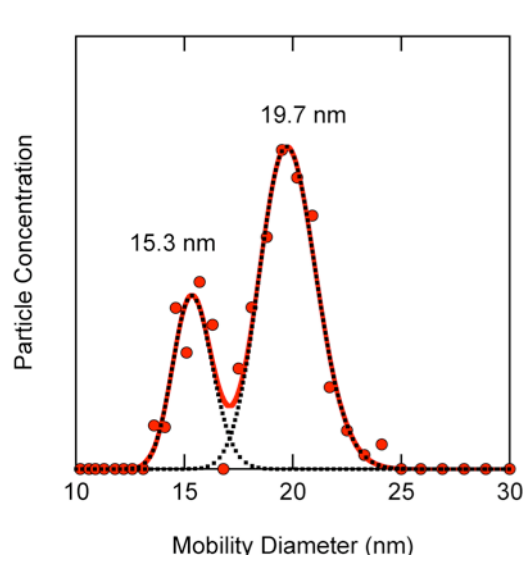

Figure 4.3: Bimodal size distribution in mobility histogram of 14.0 ± 0.2 nm 5.0 wt/wt% SDS at 79.4% RH. Data is fit with lognormal curves.

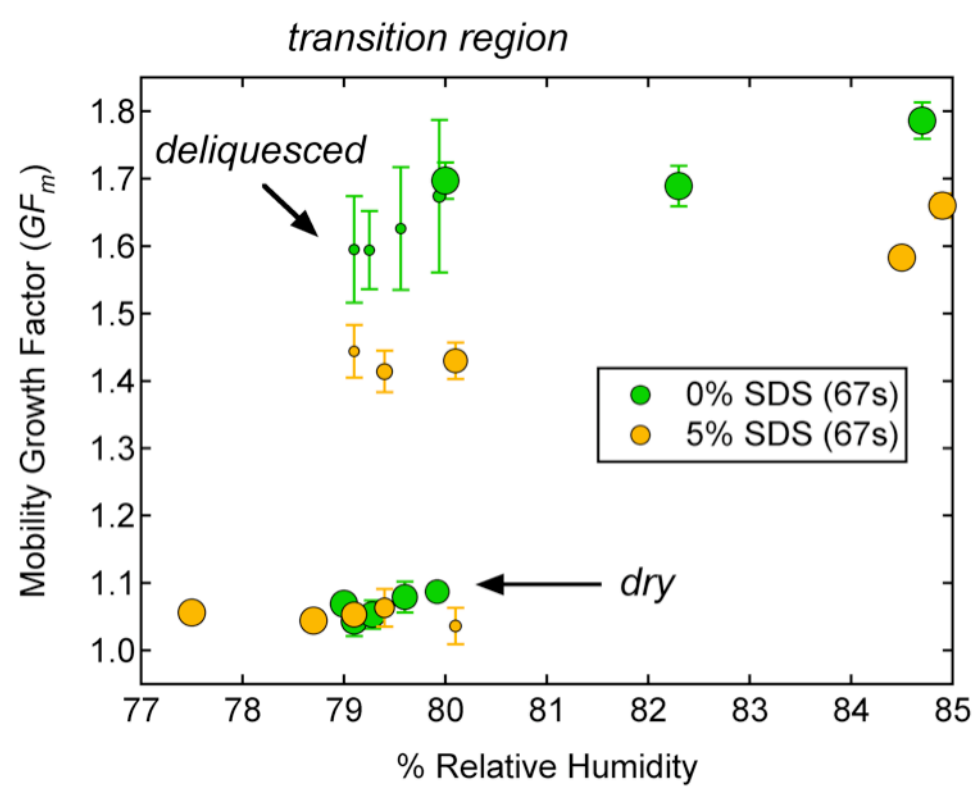

Figure 4.4: Bimodal particle distributions in growth space for 14 nm NaCl and 5.0 wt/wt% SDS/NaCl. The size of the marker indicates the relative fraction of particles in their respective size mode.

was carried out for 14 nm NaCl and 5.0 wt/wt% SDS/NaCl near the deliquescence point and those results are presented in Figure 4.4. In Figure 4.4, the size of the marker indicates the relative fraction of nanoparticles in each respective mode (i.e., dry or deliquesced). Each data point seen in Figures 4.1, 4.2, and 4.4 is an average value resulting from several mobility measurements at one value of RH. As can be seen in Figure 4.4, between 79% and 80% RH, majority of the nanoparticles for both NaCl and 5.0 wt/wt% SDS/NaCl are in the dry mode wetted with a few MLs of water. Above 80% RH, the majority of nanoparticles of both compositions very abruptly appear in the deliquesced mode corresponding to the completion of the phase transistion.

4.1.3 – Water Vapor Activity over Bulk Mixtures of NaCl/$Na_2SO_4$and NaCl/SDS

Figure 4.5 shows measured water vapor activity, a_w, as a function of dry NaCl mole fraction, χ_{NaCl}, in the NaCl/SDS (filled circles) and NaCl/Na_2SO_4 (open circles) mixtures submerged in H_2O. Since these are bulk measurements, activity is determined by eq. 1.6. There are no prior measurements for the NaCl/SDS mixture. The NaCl/Na_2SO_4 mixture, which was used for the validation of the measurements, has been examined previously.[5] The eutonic point of NaCl/Na_2SO_4, which corresponds to the composition of the mixture that minimizes water activity, 0.743 ± 0.015 (1σ deviation in repeat measurements) at χ_{NaCl} = 0.62, agrees well with previous studies.[5] Na_2SO_4 has a solubility of 21.9 w/w% in water that is comparable with the NaCl solubility of 26.5 w/w% at 298K. SDS is less soluble in water (2.8 wt/wt% in H_2O at 293K) and appears to have a eutonic point at χ_{NaCl} = 0.92 corresponding to a measured activity of 0.747 ± 0.010. This is very close to the measured activity of a saturated NaCl solution of 0.764 ± 0.010 in this laboratory. Above the eutonic point, measured activities are analogous to a saturated NaCl solution where the NaCl solubility is weakly affected by the presence of SDS or Na_2SO_4. However, below the eutonic point, activity goes up monotonically. Here activity is equivalent to that of an under-saturated NaCl solution. Measured activities of pure SDS and Na_2SO_4 solutions at χ_{NaCl} = 0 are close to unity, 0.982 ± 0.010 and 0.945 ± 0.011, respectively. As vapor pressure lowering is a colligative property, these measurements indicate that high concentrations of SDS reduce the apparent NaCl solubility.

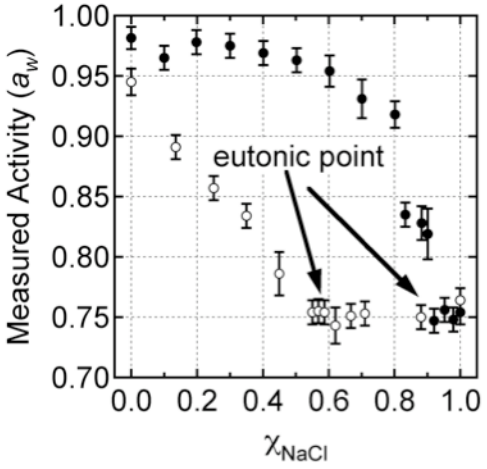

Figure 4.5: Measured water activities above saturated solutions of NaCl/Na_2SO_4 (open circles) and NaCl/SDS (filled circles) bulk solutions. Data are reported as a function of dry NaCl mole fraction (χ_{NaCl}) in the corresponding mixture.

Section 4.2 – *Pre-Deliquescent Wetting of SDS/NaCl Nanoparticles*

4.2.1 – Pre-Deliquescent Growth

Just as pure NaCl nanoparticles do, mixed SDS/NaCl nanoparticles also take up a few MLs of water prior to deliquescing. Figure 4.6 shows the pre-deliquescence region for NaCl and SDS/NaCl 14.0 ± 0.2 nm particles exposed to 1 s of humidity. The legend in Figure 4.1 details the data points in Figure 4.6 and the thick dotted line indicates the DRH of 14 nm NaCl.[1] As can be seen in Figure 4.6(a), 5.0 wt/wt% SDS/NaCl nanoparticles follow pure NaCl nanoparticle growth with excellent agreement in the pre-deliquescent region. Figure 4.6(b) shows nanoparticles containing 11, 23 and 50 wt/wt% SDS have GF_m reproducible larger than 1.00 near the DRH, although do not follow the pure NaCl nanoparticle pre-deliquescent growth trend. Interestingly, nanoparticles containing more than 5.0 wt/wt% SDS do not deliquesce promptly or agree with NaCl pre-deliquescent growth, whereas the 5.0 wt/wt% SDS/NaCl nanoparticles deliquesce promptly at NaCl DRH and follow NaCl pre-deliquescent growth with excellent agreement.

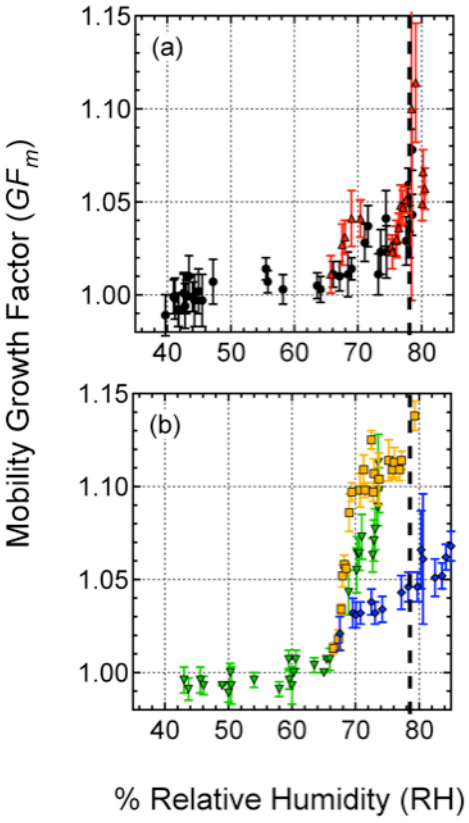

Figure 4.6: Pre-deliquescent growth of 14.0 ± 02 nm NaCl and SDS/NaCl nanoparticles exposed to 1 s of RH. See the legend in Figure 4.1 for details. The thick dotted line indicates 14 nm NaCl DRH. Error bars are 2σ from repeat measurements.

It is uncertain if the influence of particle shape on mobility is present in SDS/NaCl nanoparticles. Presumably these SDS/NaCl nanoparticles could be spherical if SDS existed in an outer shell on the NaCl surface, which would make shape considerations on mobility irrelevant. Previous research by Woods et al. [4] showed, using probe-molecule techniques, prior

to deliquescing 70-100 nm SDS/NaCl particles appear to have a mobile, soapy-like layer on their surface. This was described as a thin film of water (ML regime) on the NaCl surface with the polar head group of SDS sitting on top of the adsorbed water film.[4] Certainly, a wetted surfactant layer should be able to smooth the NaCl surface;[6-8] however, it is uncertain what shape this nanoparticle would take on. Standard adsorption isotherms will be evaluated below with and without considerations of shape correction for 5.0 wt/wt% SDS/NaCl nanoparticles.

4.2.2 – Comparison of Data to Standard Adsorption Isotherms

Figure 4.7 shows adsorption isotherms plotted in growth space (see section 3.2.1) compared to measured growth factor data of 14 nm 5.0 wt/wt% SDS/NaCl nanoparticles prior to deliquescence. The black family of curves is isotherms which have been corrected for the assumed cubic shape and are nominally the same adsorption isotherms as plotted for NaCl in Figure 3.3 (FHH values: A = 0.96, B = 1.0; BET value: c = 1.5); however, a constant value of 32 mN m^{-1} is used for surface tension in the Kelvin effect correction term as opposed to empirical formulations of surface tension as a function of weight fraction, $\sigma_{aq}(w_t)$, determined for concentrated NaCl aqueous solutions.[9] The blue family of curves have not been corrected for shape and also uses the same considerations of surface tension and isotherm parameters as the black family of curves. The red family of curves have been corrected for shape and includes the reduced value of surface tension; however, isotherm values have been parameterized for a best-fit with experimental data (FHH values: A = 0.75, B = 1.0; BET value: c = 1.1).

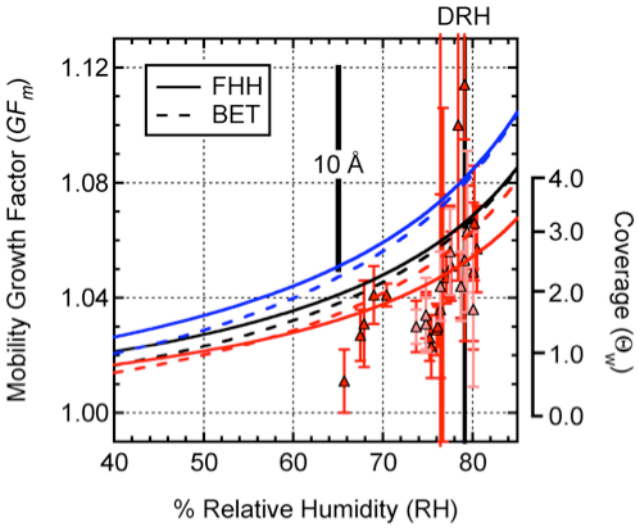

Figure 4.7: Standard adsorption isotherms compared to measured mobility growth factors of 14 nm 5.0 wt/wt% SDS/NaCl particles. Error bars are 2σ from repeat measurements. The blue family of curves represents isotherms that are not shape corrected whereas the black family of curves is shape corrected. The red family of curves has been shape corrected and isotherm values have been parameterized for a best-fit with experimental data.

As can be clearly seen in Figure 4.7, error bars near the deliquescence point are large; consequently, it is difficult to ascertain the influence of particle shape on mobility with the limited amount of data presented in Figure 4.7. Nevertheless, with the cubic shape there is more agreement with measured growth factor data and the black family of curves than compared to the blue family of curves. However, this agreement can also be brought around by other factors. For example, the red family of curves has the best agreement with experimental data due to best-fit parameterization. A BET c value of 1.1 for 5.0 wt/wt% SDS predicts the interaction between the 1st ML and multilayer region is less exothermic than interactions between the 1st ML and multilayer region for water adsorption on neat NaCl (c = 1.5).[10-12] BET c value greater than 1 is still adequate for describing interactions that are dominated by electrostatic NaCl-H_2O interactions in the 1st ML and H_2O-H_2O interactions in the multilayer.[11,12] Similar conclusions can be reached by comparison of the FHH isotherms fits.[11,12] In summary, pre-deliquescent wetting of 5.0 wt/wt% SDS/NaCl nanoparticles is very similar to pre-deliquescent wetting of pure NaCl nanoparticles.

The size of error bars in this region also indicates the heightened degree of variability in growth factor measurements for 5.0 wt/wt% SDS/NaCl could be related to the mobile, soapy layer Woods et al.[4] discussed on SDS/NaCl particle surfaces prior to deliquescence. Indeed, analysis similar to that done for NaCl nanoparticles in section 3.2.2 reveals 5.0 wt/wt% SDS/NaCl nanoparticles have 3.1 ± 0.5 ML of adsorbed surface water on their surface prior to deliquescing as well. The nature of this H_2O-SDS-NaCl surface layer is uncertain, and further investigation of how much SDS is on the surface of 5.0 wt/wt% SDS/NaCl nanoparticles prior to electrospray generation is necessary. It seems the SDS layer would have to be less than a ML or is fairly porous, facilitating the uptake of water through the hydrophobic chains and percolating in toward the hydrophilic NaCl core. The SDS surface layer and SDS content of mixed hybrid SDS/NaCl nanoparticles will be evaluated in Section 4.3.

Section 4.3 – *Estimating SDS content in Nanoparticles based on Hygroscopicity*

4.3.1 – Structure of SDS/NaCl Nanoparticles Inferred from their Hygroscopic Growth

Hygroscopic growth of SDS/NaCl nanoparticles can reveal details about the composition and morphology of SDS/NaCl nanoparticles produced in the electrospray process. SDS and NaCl are likely to phase segregate during the primary and progeny droplet evaporation in the electrospray source as bulk activity measurements showed SDS and NaCl are poorly miscible with each other in solution. Once the evaporation stage is complete nanoparticles should have a NaCl crystalline core decorated by a film of SDS molecules and possibly some residual water stuck in between SDS and NaCl (the evidence for the residual water will be discussed in Chapter 5). The sub-monolayer SDS film on NaCl is likely to have the $-O-SO_3^- Na^+$ head group of the SDS pointing toward the NaCl surface similar to an inverted micelle-like orientation. This is

consistent with the morphology of 70-100 nm SDS/NaCl particles deduced by Woods et al.[4] from probe molecule spectroscopy techniques.

When the amount of SDS exceeds the amount needed for one monolayer, the excess SDS can either accumulate in a "blob" attached to the particle or coat the surface more uniformly with a multi-layer film of SDS. The effective thickness of the SDS coating should increase with the SDS weight fraction from the solutions that were electrosprayed. This appears to be a good initial assumption as GF_m are monotonically suppressed in growth curves (Figure 4.1) as the weight percent of SDS increases. The actual thickness of the SDS film can be estimated using a simple model,[2] which assumes core-shell morphology and the volume of each component is represented by bulk densities (ρ_{NaCl} and ρ_{SDS}) and amounts of NaCl and SDS. Equation 4.1 shows how the core NaCl diameter (d_{NaCl}) is calculated, where w_t is NaCl weight percent and d_m is the overall particle diameter. The effective SDS film thickness (Δ_{SDS}) is then calculated as ($d_m - d_{NaCl}$)/2.

$$d_{NaCl} = \left(\frac{w_t \, \rho_{SDS} \, d_m^3}{\rho_{NaCl} - (\rho_{NaCl} - \rho_{SDS}) w_t} \right)^{1/3} \qquad (4.1)$$

It should be emphasized, however, that these calculations are rather approximate as the density of the surfactant layer is uncertain. For example, Tsai et al.[13] studied Au nanoparticles (10-60 nm) functionalized with alkanethiol self-assembled monolayers (SAMs) and showed the organic coating was quite "soft". The actual thickness of the organic coating, which was deduced from temperature programmed desorption and mobility diameter measurements, was found to be smaller than expected from purely geometric considerations.[13]

4.3.2 – Zdanovskii-Stokes-Robinson (ZSR) model

The ZSR model (Equation 4.2) can be used to estimate the relative volume fractions, ε_{SDS} and ε_{NaCl}, of SDS and NaCl in the SDS/NaCl nanoparticles.

$$GF_{particle}^3 = \varepsilon_{NaCl} GF_{NaCl}^3 + \varepsilon_{SDS} GF_{SDS}^3$$
$$GF_{particle}^3 \approx 1 + \varepsilon_{NaCl}\left(GF_{NaCl}^3 - 1\right) \quad (4.2)$$

Pure SDS nanoparticles do not adsorb any measurable amount of water in the range of 5-95% RH; therefore, it is assumed the ZSR model only depends on growth factors for NaCl (GF_{NaCl}). The right hand side of Equation 3.4 (the MKT Model 4) is substituted for GF_{NaCl} in Equation 4.2 and the NaCl volume fractions (ε_{NaCl}) expected from electrosprayed solutions (TABLE 2.2) are used as the initial guesses. ε_{NaCl} is then used as an adjustable parameter to get the best agreement between the ZSR predictions and experimental observations. Figure 4.8 shows the results for 14 nm (b) 5.0 wt/wt % SDS/NaCl, (c) 11 wt/wt % SDS/NaCl, (d) 23 wt/wt % SDS/NaCl, and (e) 50 wt/wt% SDS/NaCl. The ZSR model clearly fails with the assumption that the nanoparticle composition is identical to that of the electrosprayed solutions. The agreement improves significantly if one allows for the enhancement of SDS relative to NaCl in the electrosprayed droplets. The dotted lines in Figure 4.8 represent optimized dry NaCl volume fractions based on GF_m measurements of SDS/NaCl nanoparticles. There is excellent agreement in the shape of predicted GF_m in the parameterized ZSR model with measured GF_m. TABLE 4.1 summarizes the results of this analysis, where the SDS weight percent calculated from the ZSR model is compared to the composition of the initial solution as well as the SDS film thickness discussed above.

4.3.3 – Surfactant Enhancement in Nanoparticles

The shape of the growth curves predicted by the parameterized ZSR models matches the shape of the observed SDS/NaCl growth curves even at high SDS volume fractions, when NaCl is the minor component in the particle. This implies that SDS/NaCl nanoparticles contain well defined nanocrystals of NaCl embedded in the SDS matrix as opposed to small "nanoshards" of NaCl randomly distributed through the SDS matrix.

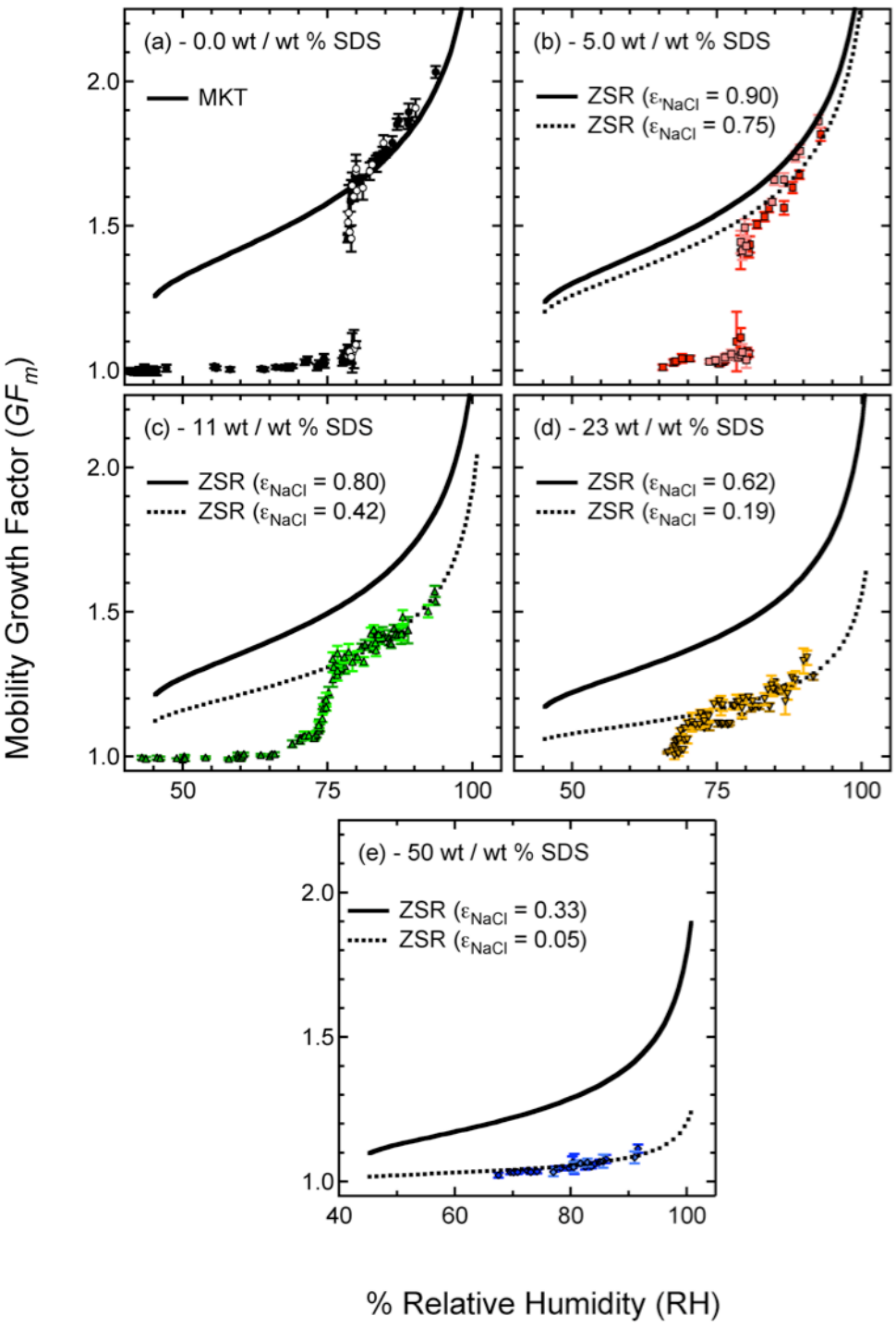

Figure 4.8: Predictions of MKT model 4 and the ZSR model (Eq. 4.2) compared to the experimental data for 14 nm **(a)** NaCl and **(b)-(e)** SDS/NaCl particles. Solid lines represent predictions that use NaCl volume fractions (ε_{NaCl}) expected from bulk solutions. Dotted lines represent ZSR model results with the NaCl volume fractions adjusted to fit the GF_m measurements. Both 1 s and 67 s RH exposure data sets are plotted (see legend in Figure 4.1)

TABLE 4.1: SDS/NaCl Nanoparticle Composition Results from ZSR Modeling

Expected Composition from Electrosprayed Solutions						Calculated Composition from ZSR model						
wt/wt % SDS	χ_{NaCl}	ε_{NaCl} [a]	d_{NaCl} (nm) [b]	Δ_{SDS} (nm) [c]	a_w [d]	wt/wt % SDS	χ_{NaCl}	ε_{NaCl} [a]	d_{NaCl} (nm) [b]	Δ_{SDS} (nm) [c]	a_w [d]	DRH (% RH) [e]
0	1.00	1.00	14.0	0.0	0.764	0	1.00	1.00	14.0	0.0	0.764	78.5
5.0	0.99	0.90	12.1	1.0	0.748	14	0.97	0.75	10.0	2.0	0.756	79.5
11	0.98	0.80	10.6	1.7	0.756	40	0.88	0.42	7.0	3.5	0.828	76.8
23	0.94	0.62	8.7	2.7	0.747	67	0.71	0.19	4.9	4.6	0.931	70.7
50	0.83	0.33	6.2	3.9	0.835	90	0.36	0.05	3.0	5.5	0.975	-

[a] NaCl volume fraction of a dry particle corresponding to wt/wt % SDS

[b] NaCl core diameter calculated from previous methods (Eq. 7).[2]

[c] thickness of SDS film: $(14.0 - d_{NaCl})/2$

[d] measured activity of a bulk solution corresponding to the listed composition

[e] measured deliquescence point of nanoparticles

The ZSR model predicts significant SDS enhancement in nanoparticles relative to the solutions from which they were electrosprayed. In our previous experiments with AOT/NaCl particles[2] an AOT enhancement was also observed; however, not to the extent as for SDS/NaCl nanoparticles. These differences likely reflect stronger surfactant properties of SDS relative to AOT.

The observation of surfactant enhancement in nanoparticles in this work and previously[2] is consistent with other studies involving electrospraying surface active materials. Tang and Smith[14] observed smaller satellite and progeny droplets generated by the spray formation and asymmetric fission processes to be enhanced in surfactants SDS and Flurad Carbon™ (FC-171, $C_8F_{17}SO_2N(C_2H_4O)_7CH_3$), a nonionic liquid surfactant. It is uncertain which generation of droplet fission in the electrospray process the SDS/NaCl nanoparticles originated from in this work. It was empirically found that the nanoparticle size characteristics changed dramatically when the electrospray protocols presented in TABLE 2.2 were altered. Specifically, variance of the electrospray distance l_s had the largest effect on the size distribution as well as measured hygroscopic properties of the resulting SDS/NaCl particles (this will be discussed in more detail in Chapter 6). This suggests different generations of droplets could likely contain a different SDS content, which is consistent with Tang and Smith's observations of surfactant enhancement in the progeny droplets.[14]

4.3.4 – SDS Coverage on NaCl Nanoparticles

The effective SDS coverage for $\Theta_{SDS} \leq 1.0$ ML can be calculated from the assumed values of ε_{NaCl} (either from the solution composition or from the ZSR fits) using equations 4.3 and 4.4.[2] N_{SDS} is the number of SDS molecules, N_A is Avogadro's number, and M_{SDS} is the molecular weight of SDS.

$$S_{SDS} = \frac{N_{SDS}}{\pi\, d_{NaCl}^2} = \frac{\rho_{SDS}\, N_A \left(d_m^3 - d_{NaCl}^3 \right)}{6\, M_{SDS}\, d_{NaCl}^2} \qquad (4.3)$$

$$\Theta_{SDS} = \frac{S_{SDS}}{S_{NaCl}} \quad (4.4)$$

This analysis reveals for the 5.0 wt/wt% SDS/NaCl nanoparticles Θ_{SDS} = 0.4 ML assuming the composition is that of the electrosprayed solution. The parameterized ZSR model composition of these nanoparticles predicts that the actual SDS fraction in these particles is roughly 14 wt/wt% SDS, translating to Θ_{SDS} = 1.0 ML. The true SDS coverage is likely to be in between these two values. The adsorption isotherm analysis presented above in section 4.2 shows that water forms a film of the same thickness on pure NaCl and on the 5.0 wt/wt% SDS/NaCl nanoparticles. This suggests that SDS does not greatly interfere with NaCl-H_2O interactions at $\Theta_{SDS} \leq$ 1.0 ML. The thickness of the SDS layer for the remaining SDS/NaCl compositions is expected to exceed 1.0 ML based on the parameterized ZSR model results.

4.3.5 – Non-prompt Deliquescence in Nanoparticles

Smaller NaCl particles appear to lose the ability to deliquesce promptly in the presence of sufficient amounts of SDS or AOT.[2] Prompt deliquescence is still observed with 5.0 wt/wt% SDS/NaCl nanoparticles at the same RH as pure NaCl nanoparticles. Per the above discussion, these particles are coated with a sub-monolayer of SDS. This promptness disappears in particles with higher SDS weight fractions, which correspond to the SDS coverage in excess of a monolayer. A non-prompt deliquescence transition can be clearly recognized when viewing the data plotted with the parameterized ZSR models in Figure 4.8. The ZSR model describes an aqueous phase and, therefore, a phase transition from crystalline to aqueous phase can be viewed as complete when the growth curve converges onto the respective ZSR model predictions. The 11 and 23 wt/wt% SDS/NaCl data sets converge to their respective ZSR models over several %RH units, with particles achieving fully deliquesced states at 76.8% RH and 70.7% RH, respectively. Only 1 mode diameter is observed in mobility histograms across the entire RH

range studied for both of these compositions. It is therefore concluded that the 11 and 23 wt/wt% SDS/NaCl nanoparticles are partially dissolved droplets during their observed non-prompt deliquescent growth. It is difficult to detect a deliquescence-like transition in the 50 wt/wt% SDS/NaCl nanoparticle growth curves. ZSR analysis reveals the NaCl volume fraction of these nanoparticles to be 0.05; therefore it is not surprising the nanoparticles barely grow, even at high humidities.

4.3.6 – Implications of SDS Content in Nanoparticles from Bulk Activity Measurements

Soluble multi-component particles display mutual deliquescence at the eutonic point (χ_{solute} , a_w) of the corresponding bulk mixture.[15] In Figure 4.5, the eutonic composition of NaCl/SDS occurs at $\chi_{NaCl} = 0.92$. At NaCl mole fractions exceeding this composition, the activity is nearly the same (±1% RH) as a pure NaCl solution. SDS/NaCl nanoparticles studied in this work should therefore display mutual deliquescence in the same vicinity (± 1% RH) as pure NaCl nanoparticles at compositions of $0.92 \leq \chi_{NaCl} < 1.00$. TABLE 4.1 implies that, if the composition of the nanoparticles is the same as the electrosprayed solutions, then the 5.0, 11 and 23 wt/wt % SDS/NaCl nanoparticles should have displayed mutual deliquescence at roughly the deliquescence point of pure NaCl nanoparticles. This is not the case as only the 5.0 wt/wt% SDS/NaCl nanoparticles displayed mutual deliquescence at the pure NaCl nanoparticle deliquescence point. This observation is more consistent with compositions from the ZSR model, which predicts that 5.0 wt/wt% SDS/NaCl nanoparticle is the only composition satisfying the condition $0.92 \leq \chi_{NaCl} < 1.00$.

The observations for the mutual deliquescence of the bulk NaCl/SDS mixtures and the corresponding nanoparticles are in serious disagreement at high SDS volume fractions (TABLE 4.1). SDS/NaCl nanoparticles that are at $\chi_{NaCl} < 0.92$ (assuming ZSR model composition) display mutual deliquescence at lower values of activity in comparison to pure NaCl

nanoparticles. On the contrary, NaCl/SDS bulk mixtures at $\chi_{NaCl} < 0.92$ result in greater water vapor activities relative to a pure saturated NaCl solution. Because vapor pressure lowering is a colligative property,[16] this would imply SDS is more miscible with NaCl in the nanometer regime as opposed to the bulk regime. A more likely interpretation is that presence of SDS greatly affects the values of surface tensions at the NaCl(solid)-H_2O(adsorbed) and H_2O(adsorbed)-H_2O(gas) interfaces, which are theoretically predicted to have a large effect on the deliquescence phase transition in NaCl nanoparticles.[17] Regardless of the explanation, this dramatic change in the deliquescence behavior is a clear manifestation of the importance of interfacial molecules in thermodynamic phase transitions experienced by nanoparticles.

Section 4.4 – *Modified Köhler Theory Analysis of SDS/NaCl Nanoparticles*

4.4.1 – Using NaCl Parameters as an Initial Guess

Based on bulk activity measurements and the presence of a prompt deliquescence transition in 5.0 wt/wt% SDS/NaCl nanoparticles, it would appear activity-solubility relationships of NaCl are weakly affected by the presence of SDS at low concentrations. Therefore, the observed reduction of GF_m in hygroscopicity experiments of 14 nm 5.0 wt/wt% SDS/NaCl particles is solely attributed to there being less NaCl in the nanoparticles (due to the presence of SDS) and MKT Model 4 should be amendable to predict this observed growth. It is worthwhile to note that use of the ZSR model and its ability to predict GF_m by allowing NaCl volume fraction to be parameterized is nominally the same analysis as amending MKT in this fashion. In other words, SDS and NaCl are assumed to segregate in nanoparticles and the solution core is a saturated NaCl solution with free SDS monomers partitioned to the droplet surface. MKT Model 4 is shown again for clarity in equation 4.5.

$$GF_m = \left(\frac{100\rho_s}{w_t(a_w)\rho_{aq}(w_t)} \right)^{1/3} A(Kn,\chi) \qquad (4.5)$$

The results of MKT analysis for 5 wt/wt% SDS/NaCl nanoparticles are presented in Figure 4.9. This analysis is also conducted for the other SDS/NaCl nanoparticle compositions as a proof of principle. The black curves represent MKT calculated with no shape correction considerations ($A(Kn,\chi) = 1$), a constant surface tension of 32 mN m^{-1} in the Kelvin effect correction term, and d_{NaCl} from ZSR model results (TABLE 4.1) are used to calculate weight

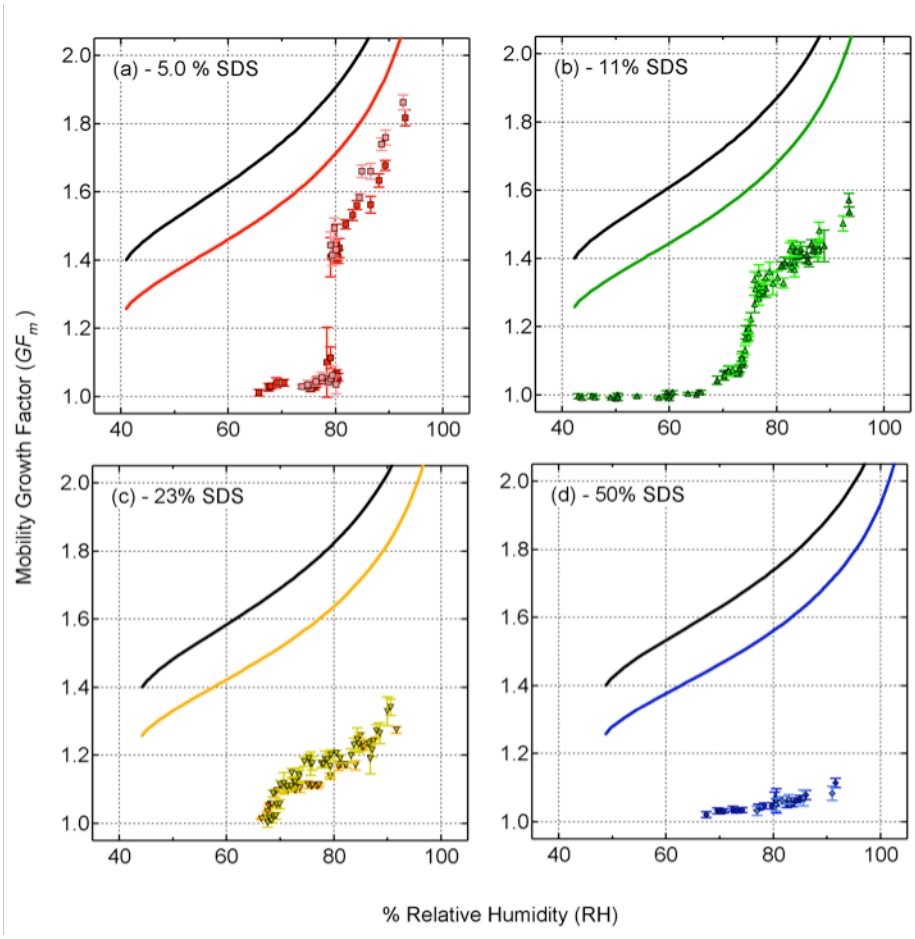

Figure 4.9: MKT amendments for surface-active molecules compared to measured GF_m of 14.0 ± 0.2 nm SDS/NaCl nanoparticles. The black curves have not been corrected for shape, use d_{NaCl} (TABLE 4.1) to calculate activity-solubility relationships of each composition, and use 32 mN m^{-1} as the surface tension in the Kelvin effect correction terms. A shape correction has been applied to the colored curves.

fraction as a function of activity, $w_t(a_w)$, for each respective composition. The colored curves (red in Figure 4.9(a), green in (b), yellow in (c), and blue in (d)) are similar to the black family or curves, where the only difference is a shape correction ($A(Kn,\chi)$ = 0.898) is used. In both the black and colored curves, the density of $NaCl_{(s)}$ and $NaCl_{(aq)}$ (as a function of aqueous weight fraction) are used for ρ_S and $\rho_{aq}(w_t)$ respectively; however, in reality the actual density (solid and aqueous) of the particle (SDS content + NaCl content, dry or in solution) should be used for these parameters instead.

As can be seen in Figure 4.9, GF_m are predicted to be too large in either amendment of MKT Model 4 for any composition of SDS/NaCl nanoparticles. Use of a shape correction reduces the magnitude of predicted growth factors; however, as will be shown in Chapter 5, 23 wt/wt% SDS/NaCl nanoparticles are spherical. Thus, a shape correction is not physically accurate in this analysis. The reasons for the lack of agreement in predicted versus measured GF_m are attributed solely to the misrepresentation of solid and aqueous densities of the mixed nanoparticles, which are a function of activity and are unknown a priori. Recall that activity-solubility relationships used in MKT Model 4 for neat NaCl nanoparticles in section 3.3.1 were from empirical determination.[5] To use MKT for proper comparison of measured GF_m in SDS/NaCl nanoparticles, the density and activity as a function of total solute weight fraction ($w_t^{SDS} + w_t^{NaCl}$) needs to be measured.

The density and particle shape of 296 and 500 nm SDS/NaCl particles has been studied experimentally by a single particle laser ablation time of flight (SPLAT) technique.[18] Researchers found the totally particle density dropped significantly as the weight fraction of SDS increased from 0.0 to 0.2. Interestingly, at high SDS weight fractions, the density of the dry particle was more representative of an SDS liquid-crystal-phase at 1.13 g cm^{-3} as opposed to a dry-crystalline-phase of SDS at 0.37 g cm^{-3}.[18] It is unclear how these physical properties will change

as a result of nano-size effects. For now, the combined SDS/NaCl nanoparticle density remains unknown a priori.

Interestingly, even though it would appear that 5.0 wt/wt% SDS/NaCl nanoparticles (more likely to be 14 wt/wt% SDS/NaCl according to the ZSR model) have remarkably similar hygroscopic properties to pure NaCl nanoparticles, amendments to MKT analysis in this work do not predict GF_m. The evidence for this statement comes from identical pre-deliquescent wetting, prompt deliquescence, and bulk water vapor activity. Once again, this demonstrates the importance of interfacial molecules in hygroscopic properties of nanoparticles and certainly merits further investigation.

References

(1) Biskos, G.; Malinowski, A.; Russell, L.; Buseck, P.; Martin, S., **"Nanosize Effect on the Deliquescence and the Efflorescence of Sodium Chloride Particles"**. *Aerosol Science and Technology* **2006**, *40*, 97.

(2) Alshawa, A.; Dopfer, O.; Harmon, C. W.; Nizkorodov, S. A.; Underwood, J. S., **"Hygroscopic Growth and Deliquescence of NaCl Nanoparticles Coated with Surfactant AOT"**. *Journal of Physical Chemisry A* **2009**.

(3) Chen, Y.-Y.; Lee, W.-M. G., **"The Effect of Surfactants on the Deliquescence of Sodium Chloride"**. *Journal of Environmental Science and Health* **2001**, *A36*, 229.

(4) Woods, E., III; Kim, H. S.; Wivagg, C. N.; Dotson, S. J.; Broekhuizen, K. E.; Frohardt, E. F., **"Phase Transitions and Surface Morphology of Surfactant-Coated Aerosol Particles"**. *Journal of Physical Chemistry A* **2007**, *111*, 11013.

(5) Tang, I. N.; Tridico, A. C.; Fung, K. H., **"Thermodynamic and Optical Properties of Sea Salt Aerosols"**. *Journal of Geophysical Research-Atmospheres* **1997**, *102*, 23269.

(6) Verdaguer, A.; Segura, J. J.; Fraxedas, J.; Bluhm, H.; Salmeron, M., **"Correlation between Charge State of Insulating NaCl Surfaces and Ionic Mobility Induced by Water Adsorption: A Combined Ambient Pressure X-ray Photoelectron Spectroscopy and Scanning Force Microscopy Study"**. *Journal of Physical Chemistry C* **2008**, *112*, 16898.

(7) Cabrera-Sanfelix, P.; Portal, D. S.; Verdaguer, A.; Darling, G. R.; Salmeron, M.; Arnau, A., **"Spontaneous Emergence of Cl- Anions from NaCl(100) at Low Relative Humidity"**. *Journal of Physical Chemistry C* **2007**, *111*, 8000.

(8) Ketteler, G.; Ashby, P.; Mun, B. S.; Ratera, I.; Bluhm, H.; Kasemo, B.; Salmeron, M., **"In situ Photoelectron Spectroscopy Study of Water Adsorption on Model Biomaterial Surfaces"**. *Journal of Physics-Condensed Matter* **2008**, *20*.

(9) Pruppacher, H. R.; Klett, J. D., *Microphysics of Clouds and Precipitation*; Kluwer Academic Boston, 1997, **1997**.

(10) Foster, M. C.; Ewing, G. E., **"Adsorption of Water on the NaCl(001) Surface. II. An Infrared Study at Ambient Temperatures"**. *Journal of Chemical Physics* **2000**, *112*, 6817.

(11) Adamson, A. W.; Gast, A. P., *Physical Chemistry of Surfaces*; John Wiley & Sons, **1997**; Vol. 6th.

(12) Gregg, S. J.; Sing, K. S. W., *Surface Area and Porosity*, 2 ed.; Academic Press: London, **1997**.

(13) Tsai, D. H.; Zangmeister, R. A.; Pease, L. F., III; Tarlov, M. J.; Zachariah, M. R., **"Gas-Phase Ion-Mobility Characterization of SAM-Functionalized Au Nanoparticles"**. *Langmuir* **2008**, *24*, 8483.

(14) Tang, K.; Smith, R. D., **"Physical/Chemical Separations in the Break-up of Highly Charged Droplets from Electrosprays"**. *Journal of the American Society for Mass Spectrometry* **2001**, *12*, 343.

(15) Tang, I. N.; Munkelwitz, H. R., **"Composition and Temperature Dependence of the Deliquescence Properties of Hygroscopic Aerosols"**. *Atmospheric Environment, Part A: General Topics* **1993**, *27A*, 467.

(16) Raff, L. M., *Principles of Physical Chemistry*; Prentice Hall: Upper Saddle River, NJ, **2001**.

(17) Russell, L. M.; Ming, Y., **"Deliquescence of Small Particles"**. *Journal of Chemical Physics* **2002**, *116*, 311.

(18) Zelenyuk, A.; Imre, D.; Cuadra-Rodriguez, L. A.; Ellison, B., **"Measurements and Interpretation of a Soluble Organic Surfactant on the Density, Shape, and Water-uptake of Hygroscopic Particles"**. *Journal of Aerosol Science* **2007**, *38*, 903.

Chapter 5 – Characterization of SDS/NaCl Nanoparticles

Section 5.1 – *Atomic Force Microscopy*

5.1.1 – 21 nm 23 wt/wt% SDS/NaCl Particles

Figure 5.1 shows representative AFM images of 23 wt/wt% SDS/NaCl nanoparticles impacted on HOPG at different resolutions. For these measurements, the particles were size selected (21 nm, GSD = 1.05) prior to impaction and Figure 5.2 shows a representative mobility histogram of these particles. AFM images reveal particles preferentially align with the graphite step edges, likely because graphite step edges are on par with the size of impacted nanoparticles. Line scan analysis of the observed particle heights (shown below in section 5.1.2) indicates the size selected mobility diameter was consistent with the AFM imaged diameter. Despite the size selection, some images (shown below in section 5.1.3) contained a number of very small particles (< 5 nm). Such small particles are not efficiently screened by the DMA due to diffusional limitations as the TSI nano-DMA has a lower cutoff size of 4.5 nm. Furthermore, uncharged nanoparticles can diffuse through the sheath flow of the DMA. This is especially important for smaller nanoparticles because of their large diffusion coefficient and small charge fraction (< 1%, Boltzmann).[1] Presence of these particles does not affect the results of the hygroscopic growth measurements, as the condensation particle counter is very insensitive to particles in this size range.

Interestingly, some images contained a very small amount of nanoparticles inconsistent with the size selected mobility diameter that could not have passed through the DMA column. Figure 5.1(c) shows such an example as this, where the AFM imaged diameter is roughly 8 nm and these nanoparticles were found on the same HOPG substrate as those nanoparticles imaged in Figures 5.1(a) and (b). It is uncertain where these particles could have originated from given

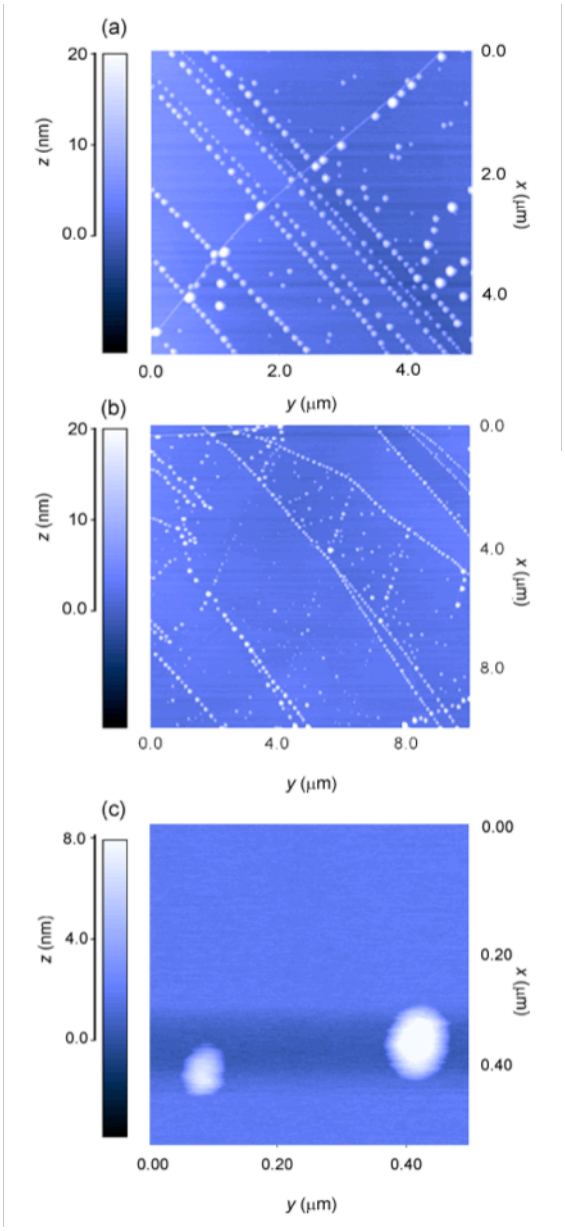

Figure 5.1: AFM images of size selected (21 nm, GSD = 1.05) 23 wt/wt% SDS/NaCl particles impacted on HOPG at different resolutions: **(a)** 5×5 μm **(b)** 10×10 μm **(c)** 0.5×0.5 μm.

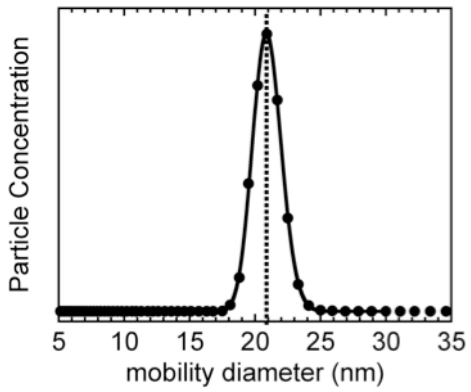

Figure 5.2: Representative mobility histogram of 23 wt/wt% SDS/NaCl nanoparticles imaged by AFM in Figure 5.1 prior to impaction on HOPG. The geometric mean mobility diameter is 20.9 nm and GSD = 1.05.

the mobility histogram in Figure 5.2 suggests the nanoparticle population is highly monodisperse. One possibility is particle restructuring upon interaction with RH conditions of the laboratory air,[2,3] which can be as high as 60% RH. Nevertheless, the AFM imaged diameter should be fairly accurate and reliable, ergo these results deserve further investigation.

AFM images of the sort shown in Figure 5.1 suggest indirectly that 23 wt/wt% SDS/NaCl nanoparticles are uniform and spherical. Higher resolution (0.5 × 0.5 μm) images were acquired, shown in Figure 5.1(c), to confirm that. Those images revealed no irregular or peculiar features on the nanoparticles, despite the lack of agreement in mobility diameter and

AFM imaged diameter for those particular nanoparticles seen in Figure 5.1(c). These images suggest that: i) both NaCl and SDS inclusions pack with similar geometry; ii) NaCl crystal is not expelled to the surface of SDS (or vice versa). It is also clear from the image in Figure 5.1(c) that some nanoparticles clump together, making them appear much wider in the x and y dimensions compared to the z dimension.

5.1.2 – Line Scan Analysis of AFM Imaged Nanoparticles

Figure 5.3(a) shows a representative AFM image of the same size selected 21 nm 23 wt/wt% SDS/NaCl particles impacted on HOPG as presented in Figure 5.1. The red line illustrates where line scan analysis using the PSI ProScan Image Processing™ software was conducted and those results are shown in Figure 5.3(b). As can be seen in Figure 5.3, while the majority of particles analyzed are consistent with the size selected mobility diameter of 21 nm, there are some particles that are inconsistent with the mobility diameter. One possibility could be related to particles crossing the edge of the line scan as opposed to the center. In the 10-20 nm regime, the majority (~99%) of particles are expected to be neutral and the remaining

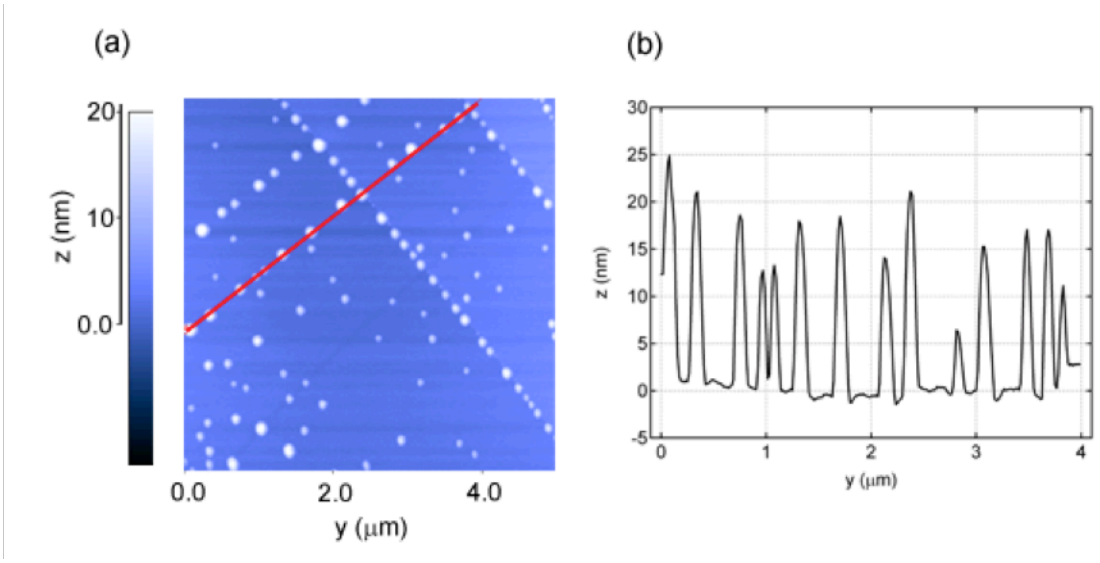

Figure 5.3: **(a)** Representative AFM image of the same size selected, impacted 23 wt/wt% SDS/NaCl nanoparticle on HOPG as presented in Figure 5.1. **(b)** Line scan analysis results of the red line illustrated in panel **(a)**.

fraction are expected to have a ±1 charge state.[1] The contribution of multiply charged nanoparticles to the total nanoparticle distribution is therefore expected to be minimal and thus is likely not a sufficient explanation to the peculiar results presented in this section and the next. However, diffusion of uncharged nanoparticles through the DMA could have resulted in their passage through the size selector as discussed above.

The discovery of very small (< 5 nm) nanoparticles generated from the electrospray source is a peculiar observation. Indeed, mobility histograms of the full nanoparticle distribution emerging from the electrospray and mobility histograms after size selection revealed no particles smaller than 5 nm. Of course, this observation is mediated by the fact that particles smaller than 5 nm can diffuse through the mobility analyzer. Furthermore, the condensation particle counter employed in this work cannot detect particles this small. Ergo, the nanoparticles smaller than 5 nm and shown below in Figure 5.4 could only be discovered by AFM imaging.

5.1.3 – Shapes of Very Small Nanoparticles

In Figure 5.4(a)-(f), various compositions of nanoparticles are shown impacted on HOPG in panels (a)-(e) and on mica in panel (f). These compositions are pure NaCl in panels (a) and (b), 5 wt/wt% SDS/NaCl in panels (c) and (d), and 11 and 50 wt/wt% SDS/NaCl in panels (e) and (f), respectively. It is uncertain if the morphology of these very small nanoparticles is similar to the morphology of the larger nanoparticles appearing in mobility histograms. These very small nanoparticles dominated the number count of imaged particles. In fact, whether a size selection was made prior to impaction or not, nanoparticles smaller than 5 nm were by far the most numerous. It should be noted that the nanoparticles imaged in Figures 5.1 and 5.3 were located right away, contrary to any other attempt, which pugnaciously involved several hours of

scanning the substrate surface only to find the tinniest nanoparticles unexpected in our attempts.

Despite these peculiar observations, as can be seen in Figure 5.4(a) and (b), imaged NaCl nanoparticles are not perfectly cubic, which is consistent with other observations of imaged NaCl particles.[4] This is likely due to the fact that nanoparticles were imaged under ambient conditions (~40% RH at 295K) and the presence of a few MLs of adsorbed water is contributing to imaged morphology. Nanoparticles containing SDS also appear to conglomerate which each other on the substrate surface as depicted in Figure 5.4(c), (d), and (e).

At present time it is impossible to make a clear distinction of nanoparticle morphology for the various SDS/NaCl compositions based on AMF imaging. Nevertheless, images of the sort shown in Figure 5.1 and 5.3 suggest nanoparticles containing a large amount of SDS are spherical and uniform. Further investigation and use of other imaging techniques, such as Environmental Transmission Electron Microscopy (ETEM), should certainly be employed. ETEM can image particles under near ambient conditions, which is desirable in this work and the reason for the initial use of AFM. Furthermore, it is much easier to zoom out and image a much larger area using electron microscopy as opposed to raster-scanning very small areas in AFM.

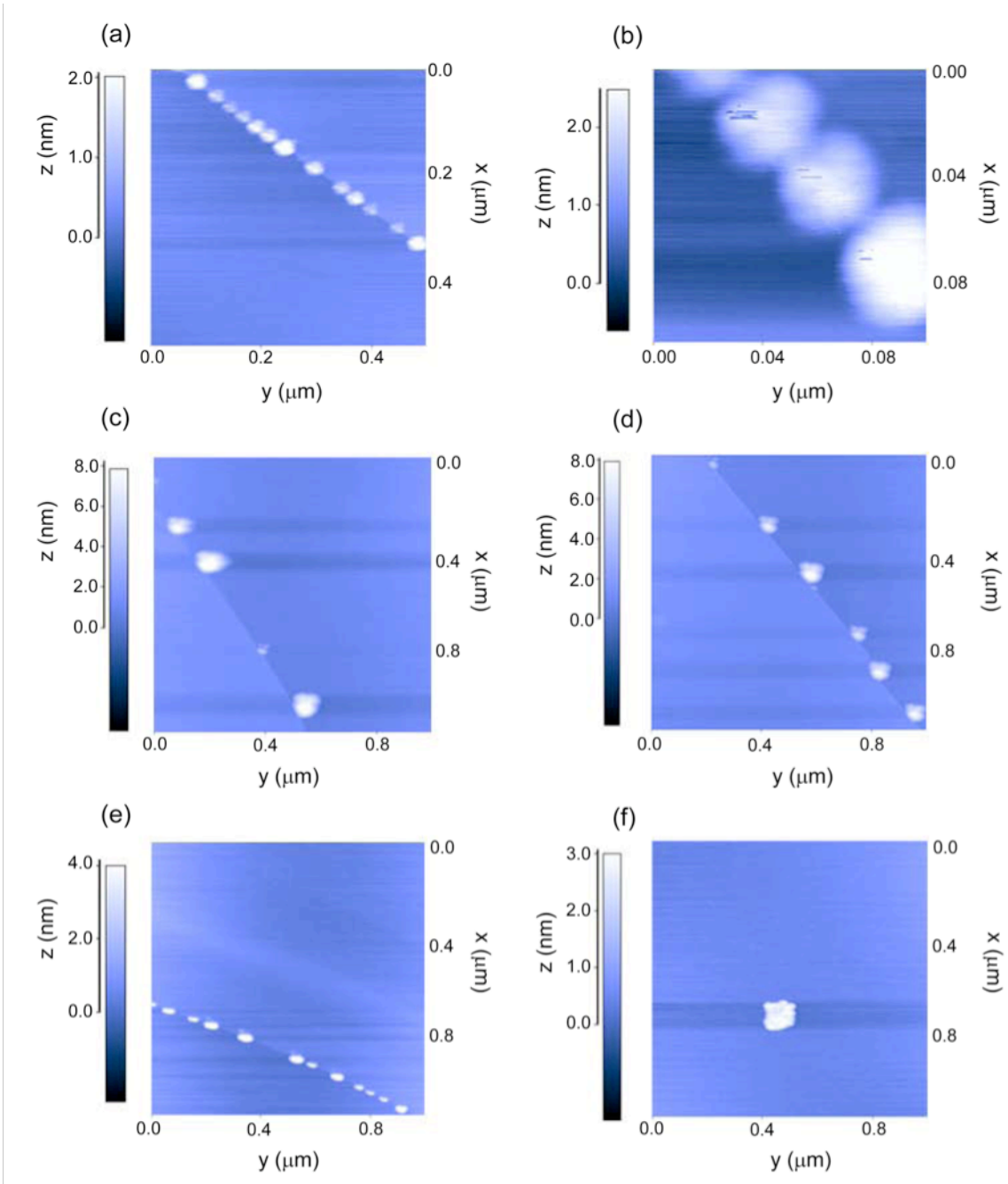

Figure 5.4: AFM images of nanoparticles not size selected and impacted on HOPG in **(a)-(e)** and on mica in **(f)**. **(a)** and **(b):** NaCl, **(c)** and **(d):** 5 wt/wt% SDS/NaCl, **(e):** 11 wt/wt% SDS/NaCl, and **(f):** 50 wt/wt% SDS/NaCl.

Section 5.2 – *X-ray Photoelectron Spectroscopy*

5.2.1 – Quantifying XPS Response Reliably

Our hypothesis that SDS/NaCl nanoparticles are enhanced in SDS prompted us to investigate their composition using XPS methods. Figure 5.5 shows representative narrow scan range XP spectra of S(2p) and Cl(2p) photoelectrons from the various compositions of impacted SDS/NaCl nanoparticles listed in TABLE 2.2. The nanoparticles analyzed by XPS are not sized selected; the full nanoparticle size distribution of each composition (see TABLE 2.2) is impacted for analysis. Spectral features of S(2p), Cl(2p), O(1s), and Na(1s) did not change significantly after several exposures totaling 30 minutes and thus are not affected by beam damage. Differences in the absolute peak areas of the S(2p) and Cl(2p) are attributed to difficulties in positioning the nanoparticle deposition ring directly under the optimum sampling position for the electron energy analyzer. To avoid these problems only relative intensities are used in the analysis.

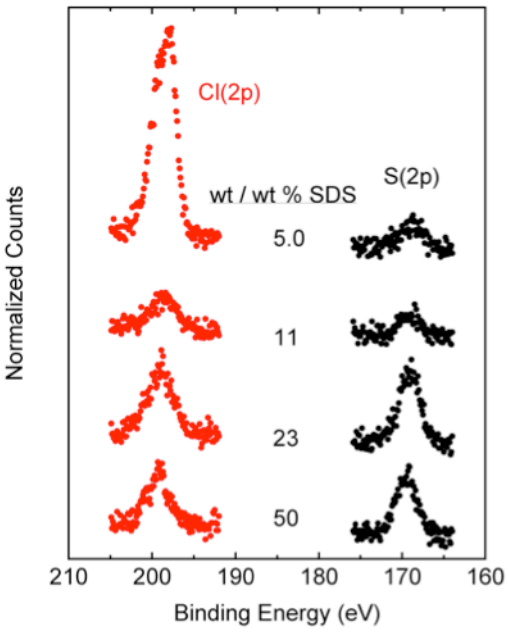

Figure 5.5: Representative narrow scan S(2p) and Cl(2p) XP spectra of impacted SDS/NaCl nanoparticles on graphite.

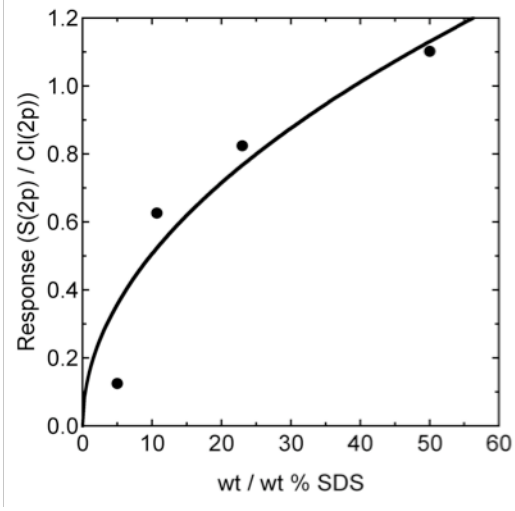

Figure 5.6: The ratio of integrated peak areas for S(2p)/Cl(2p) from XPS plotted as a function of the SDS wt/wt% contained in the electrosprayed solution.

Figure 5.6 shows the S(2p)/Cl(2p) ratio of integrated peak areas as a function of solution composition from which nanoparticles are generated. Nanoparticles from different solutions display markedly different S(2p)/Cl(2p) ratios, which increase with the amount of SDS. The largest increase is observed in going from the 5.0 to 11 wt/wt% SDS. As the fraction of SDS increases further (23 and 50 wt/wt% SDS), the S(2p)/Cl(2p) ratio shows signs of saturation. TABLE 2.2 shows that the size of the nanoparticles from the 5.0 and 11 wt/wt% SDS solutions is similar, while the impacted size for the nanoparticles from the 23 and 50 wt/wt% SDS/NaCl systems are larger. This size difference may affect both the average composition of nanoparticles generated by the electrospray source and the relative XPS response. It is assumed the effect of the impacted particle size on the relative S(2p)/Cl(2p) XPS response is minimal, and the S(2p)/Cl(2p) measurement reflects the relative amount of SDS and NaCl on the surface of the particles.

5.2.2 – Morphology of SDS/NaCl Nanoparticles Deduced from XPS Analysis

Absolute determination of the SDS coverage is not experimentally attainable from the information presented in Figures 5.5 an 5.6. However, a qualitative assessment of the nanoparticle surface can be made, as XPS is a surface sensitive technique. X-rays irradiate the entire depth of sample; however, photoelectrons are collected from a relatively small depth in the sample due to inelastic scattering of photoelectrons. The inelastic mean free path (IMFP) of an electron through NaCl with 1300 eV kinetic energy is roughly 3.5 nm.[5] The Al source produced 1456 eV photons and the binding energy of Cl(2p) is ~200 eV, thus the majority of electrons collected for NaCl would originate roughly 3.5 nm deep into the sample if no SDS existed on the surface. IMFP through aliphatic chains of the sort found in SDS is roughly 4.0 nm for an electron which has 1300 eV kinetic energy.[6] The binding energy of S(2p) is ~170 eV; therefore photoelectrons could be collected through an SDS film thickness of ~4.0 nm.

A simplistic core-shell model, in which a NaCl core floats in the middle of an SDS shell, predicts that the relative S(2p)/Cl(2p) should increase more rapidly than linear (almost exponentially) with the SDS weight fraction. Above the SDS film thickness of 4 nm, nearly all Cl(2p) photoelectrons from the NaCl core should be inelastically scattered and thus not detectible. TABLE 4.1 shows that the particles examined by XPS have an SDS thickness ranging from 0 to 3.9 nm or 0 to 5.5 nm depending on whether one assumes the solution composition or ZSR composition for the nanoparticles. The S(2p)/Cl(2p) should increase greatly over this range of SDS coat thicknesses. Figure 5.5 demonstrates that the measured S(2p)/Cl(2p) signal increases less than linearly with increasing SDS weight fraction. These observations suggest the core-shell morphology is not the best picture at high SDS weight fractions. It is also possible that a large fraction of particles deposited were very small (< 5 nm). For such small particles Cl (2p) photoelectrons would not be attenuated by the presence of SDS on the surface.

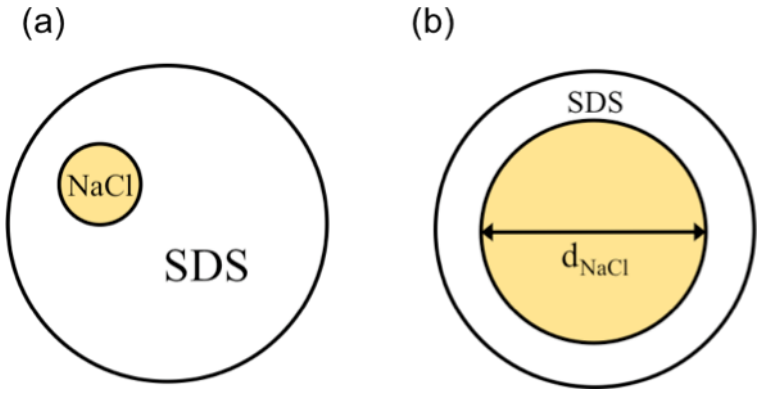

Figure 5.7: A cartoon depiction of the **(a)** "zone-inclusion" model and **(b)** "core-shell" model.

The XPS results are consistent with a "zone-inclusion" model, whereby NaCl and SDS still segregate in separate phases but the NaCl zone is no longer in the very center of the nanoparticle as the core-shell model assumes. Figure 5.7 shows a cartoon depiction of these two models. With the NaCl zone positioned near the edge of the particle, the Cl(2p) photoelectrons originating from NaCl could be fairly close to the surface and detectible by XPS.

Note that the zone-inclusion model is just as consistent with the hygroscopic growth results as the core-shell model.

5.2.3 – Oxygen Photoelectron Spectra

Figure 5.8 shows a narrow scan XP spectrum of the Oxygen, O (1s), region from impacted 23% SDS/NaCl nanoparticles. Two features are attributed to the shape of this spectrum, which indicates there are two experimentally distinguishable, chemically different types of oxygen in 23% SDS/NaCl nanoparticles. The peak at 532.6 eV is attributed to O (1s) from a sulfate moiety (R-O-SO_3) and the peak at 531.3 eV is attributed to O (1s) from a hydroxide moiety (-OH), which are both in good agreement with literature values.[7]

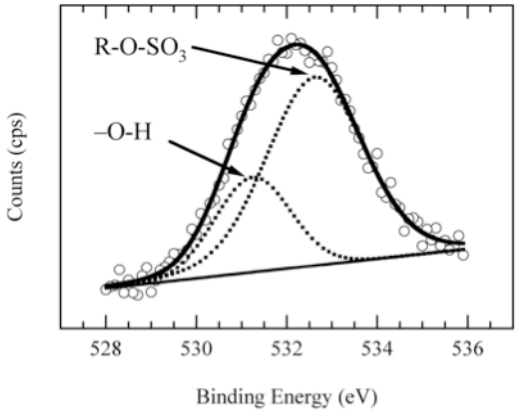

Figure 5.8: A representative narrow scan O (1s) XP spectra from impacted 23% SDS/NaCl nanoparticles.

The majority of impacted nanoparticles are neutral,[1] therefore the contribution of protonated sulfate groups to the O (1s) signal is expected to be extremely small. Adsorption of H_2O on NaCl surfaces with a high surface defect density can lead to dissociation of H_2O to form hydroxide surface species, which will be detectable on NaCl surfaces in the ultra-high vacuum regime.[8] It is uncertain if the electrospray source will make NaCl nanoparticles of the low or high surface defect variety; however, the presence of SDS in NaCl nanoparticles could influence defects of the sort which will contribute to adsorbed surface water, even under nano-Torr conditions. The spectrum in Figure 5.8, along with the very long water degassing times in FTIR analysis discussed in Chapter 2, section 2.6.2, gives evidence that 23% SDS/NaCl nanoparticles may not be entirely void of solvent after production.

Previous investigators have reported residual solvent in SDS/NaCl particles (> 100 nm) after diffusion drying.[9] Zelenyuk et al.[9] discussed the presence of residual solvent in SDS/NaCl particles could lead to a variety of different SDS meso-phases (i.e. liquid crystals, micelles, etc.) which will contribute to a markedly different SDS densities. These observations suggest the phase-state of SDS in nanoparticles could be different in all of our experiments as there are a variety of different environmental conditions and exposure times to that environment that were utilized. For example, in the hygroscopicity experiments SDS/NaCl nanoparticles are diffusion dried for a very shot time (~1 sec.), whereas in the FTIR analysis nanoparticles were exposed to dry air for several days. Nevertheless, we proceed with characterization of SDS/NaCl nanoparticles and caution is used in comparing and reporting the morphology of impacted nanoparticles to aloft nanoparticles in the hygroscopicity experiments.

Section 5.3 – *Fourier Transform Infrared Spectroscopy*

5.3.1 – Nature of SDS in Zones and Inclusions

Figure 5.9 shows an FTIR spectrum of nanoparticles from the 23 wt/wt% SDS system impacted on a ZnSe window without size-selection. The CH-stretching region (2700-3100 cm^{-1}) is plotted to show characteristic vibrations of the aliphatic moiety of SDS. The peaks at 2848 cm^{-1}, 2918 cm^{-1}, and 2956 cm^{-1} are attributed to the symmetric -CH_2- stretch (ν_{sym}), the asymmetric -CH_2- stretch (ν_{as}), and the asymmetric -CH_3 stretch, respectively.[10] Bands associated with the -O-SO_3^- Na^+ moiety were detectible at lower frequencies; however, the signal-to-noise ratio was poor due to the small amount of material analyzed. The collection time and thus amount of impacted SDS/NaCl nanoparticles is limited by the amount of solvent in the electrospray syringe, for XPS and FTIR analysis this was approximately 6 hours of impaction.

As discussed previously, the presence of residual solvent can have an influence on SDS. The phase state of SDS in the nanoparticles (23 wt/wt% and 50 wt/wt%) is therefore uncertain. Some of the possibilities include: (1) a glassy state with the alkyl chains being fairly disordered; (2) a crystalline state with a higher degree of order. All known crystalline forms of SDS pack head to head and tail to tail; however, because of chain tilting stronger bonding occurs between tails and hence the growth rate for the monohydrate and hemihydrate forms are much faster than the 1/8 hydrate and anhydrous forms.[11] If SDS is in a crystalline state, the 23 and 50 wt/wt % SDS/NaCl nanoparticles are likely of the monohydrate variety as the habit of this crystal domain is rectangular and ideally could pack well with the cubic NaCl crystal habit.

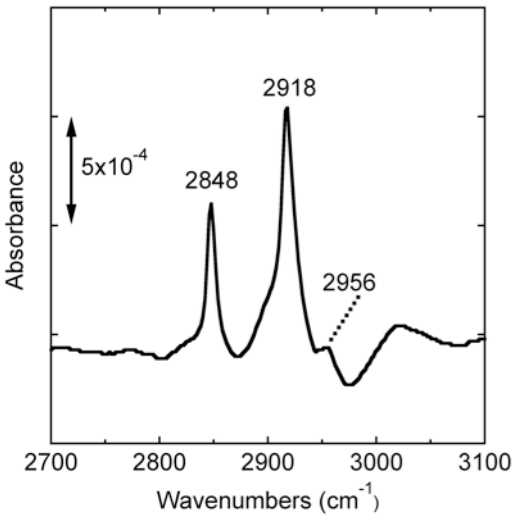

Figure 5.9: Transmission FTIR spectra of impacted 23 wt/wt% SDS/NaCl nanoparticles on a ZnSe window.

The 23 wt/wt% SDS/NaCl nanoparticles were examined by FTIR because this composition should have well in excess of a ML of SDS. FTIR spectra were difficult to obtain due the small amount of material impacted on the ZnSe window. However, the resulting spectra in the CH-stretching range (Figure 5.8) were quite informative. Most significantly, the symmetric and asymmetric -CH_2- stretches, occurring at 2848 and 2918 cm^{-1} respectively, were quite narrow, indicating minimal heterogeneous broadening of the peaks.

FTIR spectra of various SDS phases (crystalline and disordered) have been reported previously.[12] The position of the symmetric -CH_2- stretch was consistently below 2852 cm^{-1} for crystalline phases of SDS, while for micellar solutions of SDS and water was consistently above

2852 cm^{-1}.[12] The position of the asymmetric -CH_2- stretch was just at or below 2920 cm^{-1} for crystalline phases of SDS, while for micellar solutions and liquid crystal phases of SDS was above 2920 cm^{-1}.[12] The position of the peak relative to 2920 cm^{-1} is not necessarily a function of order, but can also be related to packing density.[12] In disordered SDS phases, (i.e. micelles and liquid crystals) broadening of symmetric and asymmetric -CH_2- peaks was observed relative to ordered, crystalline SDS phases (i.e SDS anhydrous, SDS·1/8H_2O, SDS·1/2H_2O, and SDS·H_2O) as well as a decreased molar absorptivity of the asymmetric -CH_2- stretch relative to the symmetric -CH_2- stretch.[12] The FTIR spectra presented in Figure 5.9 in this work appears to be more representative of an ordered, crystalline phase of SDS with high packing density.

It is peculiar that AFM images suggest 23% SDS/NaCl nanoparticles are spherical yet the FTIR spectrum presented in Figure 5.9 suggests SDS is in some type of crystalline state. Once again, the influence of residual solvent on SDS and the very different conditions used to characterize these nanoparticles (recall AFM is done under ambient RH whereas FTIR was done under very dry conditions) suggests these techniques may not be universally applicable to the characterization of SDS/NaCl nanoparticles as they exist in the hygroscopicity experiments. Nevertheless, the wide variety of employed characterization experiments, as far as this author knows, is the first attempt to characterize impacted nanoparticles produced from an electrospray source in this manner.

References

(1) Hinds, W. C., *Aerosol Technology*, 2 ed.; John Wiley & Sons, Inc., **1998**.

(2) Cabrera-Sanfelix, P.; Portal, D. S.; Verdaguer, A.; Darling, G. R.; Salmeron, M.; Arnau, A., **"Spontaneous Emergence of Cl- Anions from NaCl(100) at Low Relative Humidity"**. *Journal of Physical Chemistry C* **2007**, *111*, 8000.

(3) Verdaguer, A.; Segura, J. J.; Fraxedas, J.; Bluhm, H.; Salmeron, M., **"Correlation between Charge State of Insulating NaCl Surfaces and Ionic Mobility Induced by Water Adsorption: A Combined Ambient Pressure X-ray Photoelectron Spectroscopy and Scanning Force Microscopy Study"**. *Journal of Physical Chemistry C* **2008**, *112*, 16898.

(4) Wise, M.; Biskos, G.; Martin, S.; Russell, L.; Buseck, P., **"Phase Transitions of Single Salt Particles Studied Using a Transmission Electron Microscope with an Environmental Cell"**. *Aerosol Science and Technology* **2005**, *39*, 849.

(5) Tanuma, S., **"Calculations of Electron Inelastic Free Paths in Au-Cu and Au-Ag Alloys"**. *Bunseki Kagaku* **1991**, *40*, 667.

(6) Cumpson, P. J., **"Estimation of Inelastic Mean Free Paths for Polymers and Other Organic Materials: Use of Quantitative Structure-Property Relationships"**. *Surface and Interface Analysis* **2001**, *31*, 23.

(7) Moulder, J. F.; Stickle, W. F.; Sobol, P. E.; Bomben, K. D., *Handbook of X-ray Photoelectron Spectroscopy* Physical Electronics Division, Perkin Elmer Corp: Eden, Prairie, MN, **1992**.

(8) Hemminger, J. C., **"Heterogeneous Chemistry in the Troposphere: A Modern Surface Chemistry Approach to the Study of Fundamental Processes"**. *Int. Rev. Phys. Chem.* **1999**, *18*, 387.

(9) Zelenyuk, A.; Imre, D.; Cuadra-Rodriguez, L. A.; Ellison, B., **"Measurements and Interpretation of a Soluble Organic Surfactant on the Density, Shape, and Water Uptake of Hygroscopic Particles"**. *Journal of Aerosol Science* **2007**, *38*, 903.

(10) Socrates, G., *Infrared and Raman Characteristic Group Frequencies*, 3rd ed.; John Wiley & Sons Ltd: West Sussex, England, **2001**.

(11) Smith, L. A.; Duncan, A.; Thomson, G. B.; Roberts, K. J.; Machin, D.; McLeod, G., **"Crystallisation of Sodium Dodecyl Sulphate from Aqueous Solution: Phase Identification, Crystal Morphology, Surface Chemistry and Kinetic Interface Roughening"**. *Journal of Crystal Growth* **2004**, *263*, 480.

(12) Sperline, R. P., **"Infrared Spectroscopic Study of the Crystalline Phases of Sodium Dodecyl Sulfate"**. *Langmuir* **1997**, *13*, 3715.

Chapter 6 – Final Remarks and Suggested Future Work

Section 6.1 – *The Role of Size and Composition*

6.1.1 – Sodium Chloride Nanoparticles

A combination of experimental techniques has been used to explore hygroscopic growth of 14.0 ± 0.2 nm NaCl and SDS/NaCl particles as well as 10.9 ± 0.1 and 17.0 ± 0.2 nm NaCl particles. As the size of the dry NaCl nanoparticle decreases, its DRH increases in full accord with previous studies on NaCl nanoparticles.[1-7] Experimentally determined growth factors of NaCl nanoparticles were also found to have good agreement with modified Köhler theory when properly accounting for particle shape.[3,8] Sodium Chloride 14 nm particles were found to have 3.1 ± 0.5 ML of water adsorbed to the surface at the deliquescence point. This coverage of water was consistent with what would be expected on a bulk NaCl surface when taking the Kelvin effect into consideration for such a 14 nm particle.[8-11]

Interestingly, as the size of the dry particle decreases, its solution composition upon deliquescence increases (see TABLE 3.1), even though its deliquescence relative humidity increases. Recall, the equilibrium vapor pressure over a saturated salt solution is identical to the deliquescence point. The DRH of a salt particle is lower than the equilibrium vapor pressure of neat liquid water due to entropic effects and this is a colligative property.[12] Therefore, it should be expected that the DRH would decrease with particle size. On the contrary, the opposite happens due to nontrivial free energy contributions of the multilayer water film to the total free energy of the particle.[7] This demonstrates the importance of the phenomenological size dependence on thermodynamic phase transitions experienced by NaCl nanoparticles.

6.1.2 – Sodium Dodecyl Sulfate/Sodium Chloride Nanoparticles

14 nm particles electrosprayed from a 5.0 wt/wt% SDS/NaCl solution deliquesce at 79.1 ± 1.0% RH, the same RH as pure NaCl nanoparticles. This composition also has the same water coverage level, 3.1 ± 0.5 ML, as pure NaCl nanoparticles immediately prior to deliquescence. The estimated SDS film thickness (Θ_{SDS}) for the 14 nm 5 wt/wt% SDS/NaCl particles is close to one monolayer, and this SDS monolayer does not appear to have a strong effect on the hygroscopic properties of the NaCl core. The presence of SDS on the surface in fact makes adsorption of water more thermodynamically favorable than on bare NaCl because of the effect of SDS on the interfacial surface tension. The phase state of this H_2O-SDS surface film prior to deliquescence is likely to be fairly mobile,[13] contrary to a highly rigid array of aliphatic chains in a self-assembled monolayer, for example.

The situation changes considerably as the relative amount of SDS increases in the 14 nm particles. XPS analysis suggests that nanoparticles with high SDS content deviate from the simple NaCl core-SDS shell morphology. It is expected there is a strong energetic benefit for the SDS head groups to interact with the NaCl surface, but there is simply not enough space to accommodate all of them and lead to the growth of an SDS crystalline phase around the NaCl inclusion. The FTIR analysis reveals alkane chains are fairly ordered for 23 wt/wt% SDS/NaCl collected particles, confirming that NaCl and SDS exist in segregated crystalline structures within the nanoparticle. This morphology, referred to as a "zone-inclusion" model, is just as consistent in hygroscopic growth as the core-shell morphology, contrary to many "nano-shards" of NaCl and SDS randomly distributed throughout the particle.

As the relative amount of SDS in the nanoparticle grows the deliquescence relative humidity decreases and the deliquescence transition becomes less well defined. Hygroscopic growth curves of SDS containing nanoparticles are representative of NaCl after deliquescence.

The "non-prompt" phase transitions observed in these nanoparticles can be thought of as droplets which are partially dissolved and thus thermodynamically metastable.[12] Eventually, these droplets appear to become fully dissolved droplets due to their agreement with the ZSR model. Unfortunately, these results do not foreshadow agreement with the modified Köhler theory model for surfactants used in this work. The effect of SDS on the deliquescence and hygroscopic growth of NaCl appears to be much greater in nanoparticles than in the bulk NaCl/SDS mixtures of the same composition. This underscores the importance of interfacial properties in the phase transitions experienced by mixed organic-inorganic nanoparticles.

Section 6.2 – *Suggested Future Work: Electrospray Dynamics*

6.2.1 – Distance Dependence of Electrospray for Nanoparticle Generation

Nanoparticle production from the electrospray source is very sensitive to the experimental parameters, which are syringe pump flow rate, applied voltage, and distance l_s from the capillary tip to the neutralizer entrance. The most sensitive parameter is distance l_s and great care was taken to ensure the electrospray conditions presented in TABLE 2.2 were reproducible. A picture of the electrospray Taylor jet-cone illustrated with l_s is shown in Figure 2.8 in Chapter 2.

Initial experimentation on the distance dependence of electrospray nanoparticle production was carried out and those results are presented here. It should be noted, however, these are preliminary observations and a satisfactory explanation for this distance dependence on nanoparticle production is not yet attained.

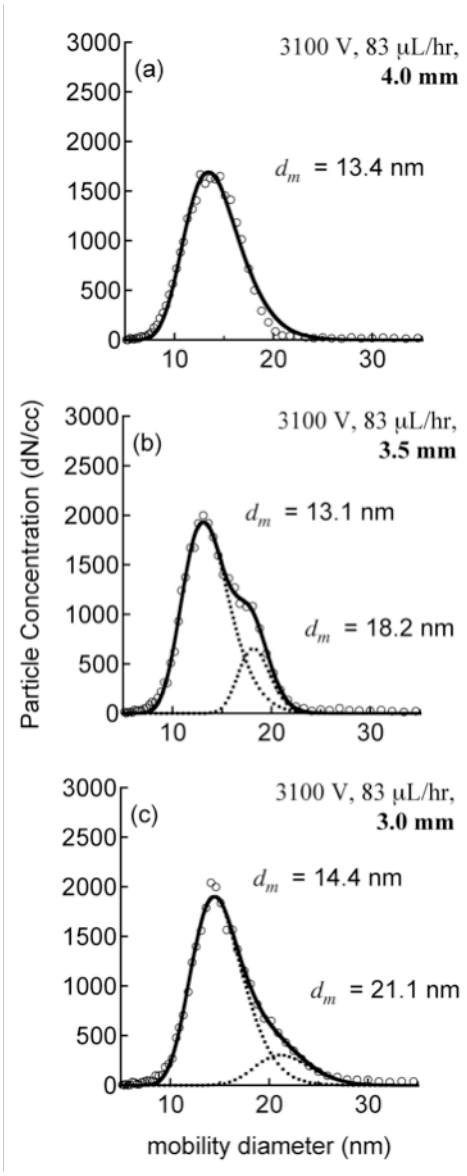

Figure 6.1: 5 wt/wt% SDS/NaCl particle mobility histograms from electrospray source at different l_s. Lognormal distributions have been fit to experimental data.

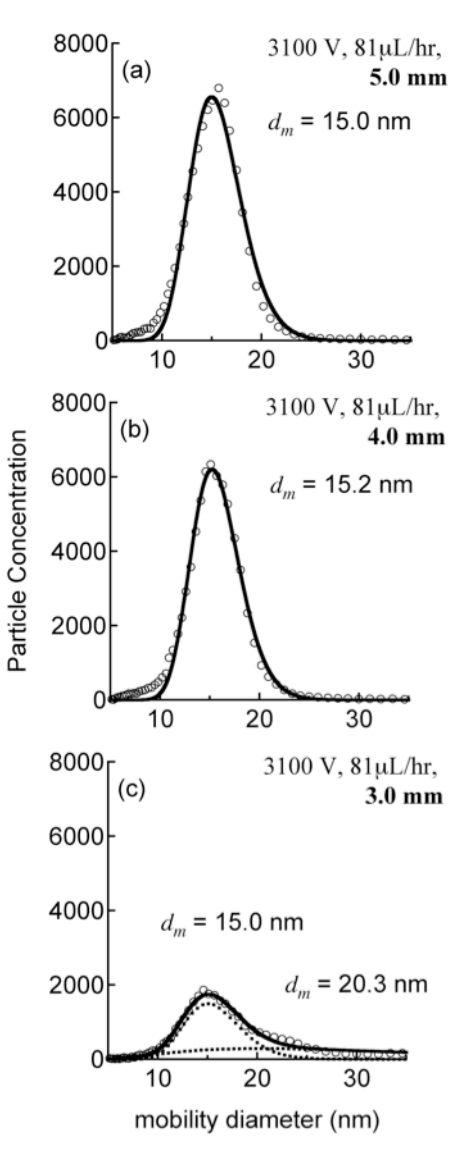

Figure 6.2: 11 wt/wt% SDS/NaCl particle mobility histograms from electrospray source at different l_s. Lognormal distributions have been fit to experimental data.

Figures 6.1 and 6.2 show mobility histograms from the electrospray nanoparticle source for the 5 and 11 wt/wt% SDS/NaCl solutions, respectively. In panels (a), (b), and (c) of each figure the electrospray conditions are nearly same except distance l_s is varied. As l_s is changed,

the nanoparticle distribution changes. Lognormal curves have been fit to the mobility histograms and this analysis reveals some distributions are bimodal. Hygroscopicity experiments were conducted from a size selection of the distributions representative of panel (a) in each figure for both 5 and 11 wt/wt% SDS/NaCl.

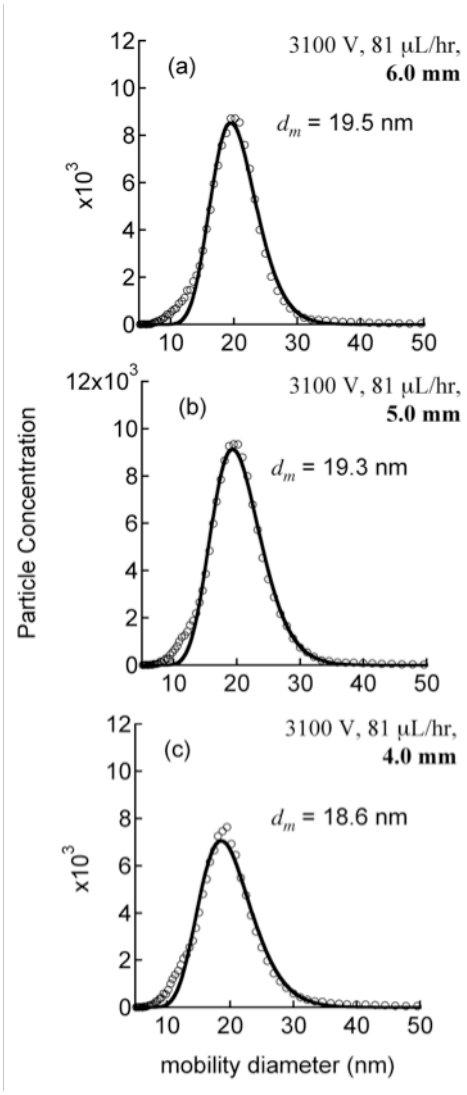

Figure 6.3: 23 wt/wt% SDS/NaCl particle mobility histograms from electrospray source at different l_s. Lognormal distributions have been fit to experimental data.

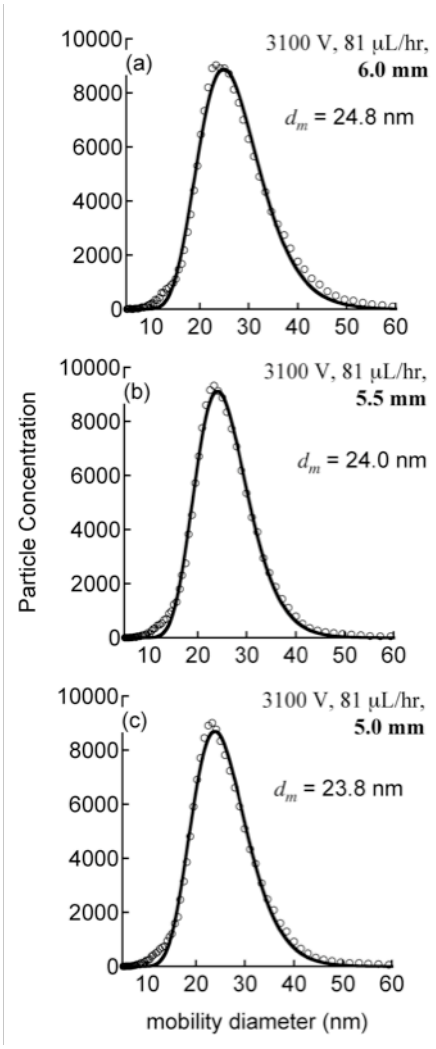

Figure 6.4: 50 wt/wt% SDS/NaCl particle mobility histograms from electrospray source at different l_s. Lognormal distributions have been fit to experimental data.

Figures 6.3 and 6.4 show mobility histograms from the 23 and 50 wt/wt% SDS/NaCl solutions, where the distance l_s was varied similarly as in the data presented in Figures 6.1 and 6.2. Hygroscopicity experiments were conducted from a size selection of the distributions representative of panel (a) in each figure for both 23 and 50 wt/wt% SDS/NaCl. As can be seen in Figures 6.3 and 6.4, the particle distribution is not as sensitive to distance l_s for 23 and 50 wt/wt% SDS/NaCl solutions as it is for the 5 and 11 wt/wt% SDS/NaCl.

The chemical content of nanoparticles emerging directly from the electrospray source as a function of distance l_s can be probed indirectly by water uptake. A size selection (14.0 ± 0.2 nm) of each composition was made from each l_s distance presented in Figures 6.1-6.4 and those particles were exposed to a constant RH (84-86% RH). Figure 6.5 shows the results of this experiment, where the open circles indicate the same hygroscopicity data presented in Chapter 4. The colored markers indicated in each legend in Figure 6.5 are growth factors taken from a size selection at different electrospray distance ls at constant RH.

As can be seen in Figure 6.5, as the electrospray jet-cone is moved closer to the neutralizer, growth factors become larger. The most prominent differences are seen in panels (b) and (d) for 11 and 23 wt/wt% SDS/NaCl, respectively. While there is an electrospray distance dependence for growth factors from 5.0 wt/wt% SDS/NaCl, growth factors from 50 wt/wt% SDS/NaCl seems to show no difference when the electrospray distance was varied. Interestingly, the mobility histogram characteristics as a function of l_s (Figure 6.3) for 23 wt/wt % SDS/NaCl were fairly constant, even though growth factors at constant RH as a function of l_s were very different. This could indicate that younger progeny droplets are deficient in SDS while older progeny droplets are enhanced in SDS assuming the electrospray dynamics are constant over this range of distances. This is likely a bad assumption as the electric field changes over very short distances (millimeters)[14] and solution conductivities of each composition are

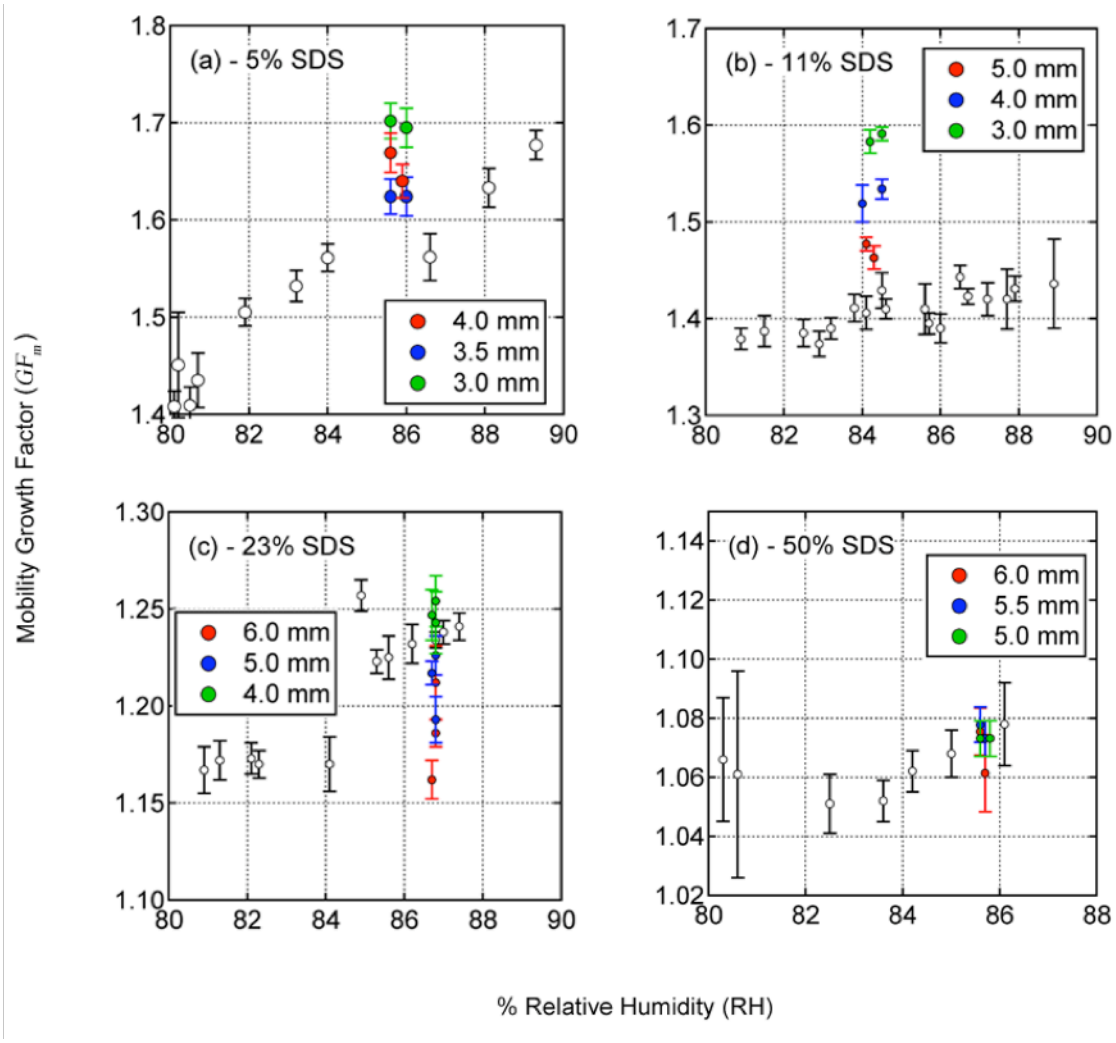

Figure 6.5: Hygroscopic growth curves of 14 nm 5, 11, 23, and 50 wt/wt% SDS/NaCl in **(a)**, **(b)**, **(c)**, and **(d)** respectively. The open circles in each panel are the same data presented in Chapter 4, where l_s = **(a)** 4.0 mm, **(b)** 5.0 mm, **(c)** 4.0 mm, and **(d)** 6.0 mm. The colored markers indicated by the legends are data measured at different distance l_s.

expected to be different. No further attempts to explore these observations were carried out; however, it should be stressed that the hygroscopicity experiments presented in Chapter 4 were conducted at constant l_s and great care was taken to ensure these conditions were reproducible throughout the course of experimentation. The electrospray distance dependence of nanoparticle production certainly merits further investigation.

Section 6.3 – *Suggested Future Work: Theoretical Investigations*

6.3.1 – Molecular Dynamics

The data presented in Chapters 3-5 has recently been submitted to the Journal of Physical Chemistry B in the form of a full journal article,[8] and is currently under review. In this manuscript, preliminary theoretical investigations were conducted by collaborators using molecular dynamics (MD) to compare to experimental data.

Figure 6.6 shows a snapshot from a MD simulation of a SDS/NaCl "core-shell" nanoparticle relaxed for 100 ps. The SDS/NaCl nanoparticle was generated with a crystalline NaCl core that was decorated by SDS molecules (Appendix II shows the input files). The nanoparticle was generated in an *x*-*y*-*z* periodic simulation box of dimensions *x* = 100.00 Å, *y* = 100.00 Å, *z* = 200.00 Å. The diameter of the particle is roughly 5 nm.

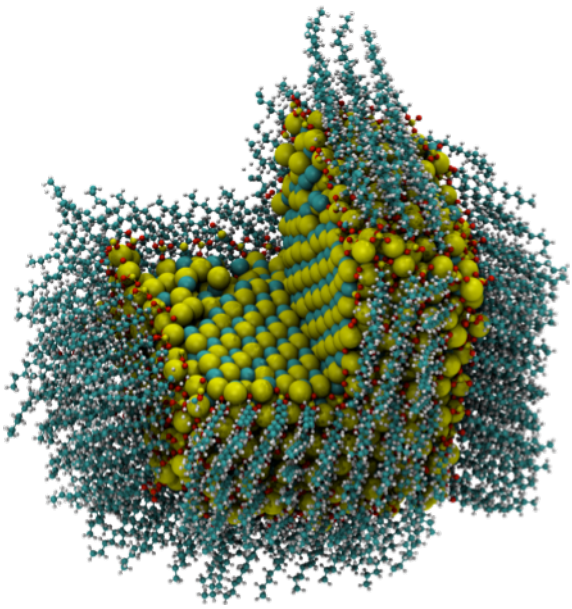

Figure 6.6: A NaCl core-SDS shell nanoparticle relaxed by a 100 ps MD simulation. A section of the particle is cut away to reveal the inner structure of the NaCl core.

The NaCl crystalline core was generated manually using a standard NaCl crystal structure with a lattice constant of 5.63 Å, which gave a nearest neighbor spacing of 2.81 Å. A full coverage monolayer of dodecyl sulfate anions (DS^-) were arranged in a rectangular lattice 5.00 Å apart on the NaCl slab with an appropriate number of sodium cation counterions on all 6 faces of the NaCl core. This defined the slab with Θ_{SDS} = 1.00. SDS molecules were positioned such that the sulfur was placed 6.61 Å above the surface of the NaCl

slab with sodium cation counterions placed between the surfactant head group and NaCl surface.

The SDS/NaCl nanoparticle was relaxed following an initial energy minimization with a 1 ns trajectory using the NAMD (Not Another Molecular Dynamics) program. NAMD was developed by the Theoretical and Computational Biophysics Group in the Beckman Institute for Advanced Science and Technology at the University of Illinois at Urbana-Champaign.[15] The SDS molecules and Na^+ and Cl^- ions were described using the CHARMM27 lipid force field[16] and the SHAKE algorithm constrained the lengths of covalent bonds to hydrogen.[17] Long-range electrostatic interactions were computed using the smooth particle mesh Ewald (PME) method[18] and van der Waals interactions were truncated at a 12 Å cutoff distance. The simulation was run with a 1 fs time step and snapshots were saved at 1 ps intervals for detailed analysis. Langevin dynamics maintained a simulation temperature of 300 K. The goal of this simulations was to probe the behavior of SDS on corners and edges of the underlying NaCl crystal.

This simulation predicts a significant degree of distortion of the NaCl structure by SDS near the edges and corners of the NaCl crystal. These sites are the least protected from water by the alkyl tails of SDS, and therefore represent the most likely sites for the initial water adsorption. From there, water molecules can percolate in between NaCl and SDS, and eventually deliquesce the NaCl crystal. The interaction of water with the SDS/NaCl nanoparticle was not simulated; however, this is the next logical step to proceed in for future work.

In Chapter 5, a peculiar observation was reported for very small (< 5 nm) SDS/NaCl nanoparticles impacted on HOPG and imaged with AFM. It is worthwhile to note the SDS/NaCl nanoparticle simulated by MD is a representative size of actual SDS/NaCl nanoparticles imaged. Simulating water uptake by these nanoparticles should therefore be regarded as a priority as MD simulations are rarely on par with the size of the system studied. These simulations could

reveal insights, over very short time scales, of fundamental water uptake on realistic 3-dimensional systems like the one presented in Figure 6.6.

References

(1) Biskos, G.; Malinowski, A.; Russell, L.; Buseck, P.; Martin, S., **"Nanosize Effect on the Deliquescence and the Effflorescence of Sodium Chloride Particles"**. *Aerosol Science and Technology* **2006**, *40*, 97.

(2) Biskos, G.; Paulsen, D.; Russell, L. M.; Buseck, P. R.; Martin, S. T., **"Prompt Deliquescence and Efflorescence of Aerosol Nanoparticles"**. *Atmospheric Chemistry and Physics* **2007**, *6*, 4633.

(3) Biskos, G.; Russell, L. M.; Buseck, P. R.; Martin, S. T., **"Nanosize Effect on the Hygroscopic Growth Factor of Aerosol Particles"**. *Geophys. Res. Lett.* **2006**, *33*, L07801.

(4) Wise, M.; Biskos, G.; Martin, S.; Russell, L.; Buseck, P., **"Phase Transitions of Single Salt Particles Studied Using a Transmission Electron Microscope with an Environmental Cell"**. *Aerosol Science and Technology* **2005**, *39*, 849.

(5) Romakkaniemi, S.; Haemeri, K.; Vaekevae, M.; Laaksonen, A., **"Adsorption of Water on 8-15 nm NaCl and $(NH_4)_2SO_4$ Aerosols Measured Using an Ultrafine Tandem Differential Mobility Analyzer"**. *Journal of Physical Chemistry A* **2001**, *105*, 8183.

(6) Hameri, K.; Laaksonen, A.; Vakeva, M.; Suni, T., **"Hygroscopic Growth of Ultrafine Sodium Chloride Particles"**. *Journal of Geophysical Research* **2001**, *106*, 20749.

(7) Russell, L. M.; Ming, Y., **"Deliquescence of Small Particles"**. *Journal of Chemical Physics* **2002**, *116*, 311.

(8) Harmon, C. W.; Grimm, R. L.; McIntire, T. M.; Peterson, M. D.; Njegic, B.; Angel, V. M.; Alshawa, A.; Underwood, J. S.; Tobais, D. J.; Gerber, R. B.; Gordon, M. S.; Hemminger, J. C.; Nizkorodov, S. A., **"Hygroscopic Growth and Deliquescence of NaCl Nanoparticles Mixed with Surfactant SDS"**. *Journal of Physical Chemistry B* **2009**, *submitted*.

(9) Finlayson-Pitts, B. J.; Hemminger, J. C., **"Physical Chemistry of Airborne Sea Salt Particles and Their Components"**. *Journal of Physical Chemistry A* **2000**, *104*, 11463.

(10) Hemminger, J. C., **"Heterogeneous Chemistry in the Troposphere: A Modern Surface Chemistry Approach to the Study of Fundamental Processes"**. *Int. Rev. Phys. Chem.* **1999**, *18*, 387.

(11) Foster, M. C.; Ewing, G. E., **"Adsorption of Water on the NaCl(001) Surface. II. An Infrared Study at Ambient Temperatures"**. *Journal of Chemical Physics* **2000**, *112*, 6817.

(12) Raff, L. M., *Principles of Physical Chemistry*; Prentice Hall: Upper Saddle River, NJ, **2001**.

(13) Woods, E., III; Kim, H. S.; Wivagg, C. N.; Dotson, S. J.; Broekhuizen, K. E.; Frohardt, E. F., **"Phase Transitions and Surface Morphology of Surfactant-Coated Aerosol Particles"**. *Journal of Physical Chemistry A* **2007**, *111*, 11013.

(14) Hinds, W. C., *Aerosol Technology*, 2 ed.; John Wiley & Sons, Inc., **1998**.

(15) Phillips, J. C.; Braun, R.; Wang, W.; Gumbart, J.; Tajkhorshid, E.; Villa, E.; Chipot, C.; Skeel, R. D.; Kale, L.; Schulten, K., **"Scalable Molecular Dynamics with NAMD"**. *Journal of Computational Chemistry* **2005**, *26*, 1781.

(16) Feller, S. E.; MacKerell, A. D., **"An Improved Empirical Potential Energy Function for Molecular Simulations of Phospholipids"**. *Journal of Physical Chemistry B* **2000**, *104*, 7510.

(17) Ryckaert, J. P.; Ciccotti, G.; Berendsen, H. J. C., **"Numerical-Integration of Cartesian Equations of Motion of a System with Constraints - Molecular-Dynamics of N-Alkanes"**. *Journal of Computational Physics* **1977**, *23*, 327.

(18) Essmann, U.; Perera, L.; Berkowitz, M. L.; Darden, T.; Lee, H.; Pedersen, L. G., **"A Smooth Particle Mesh Ewald Method"**. *Journal of Chemical Physics* **1995**, *103*, 8577.

APPENDIX I

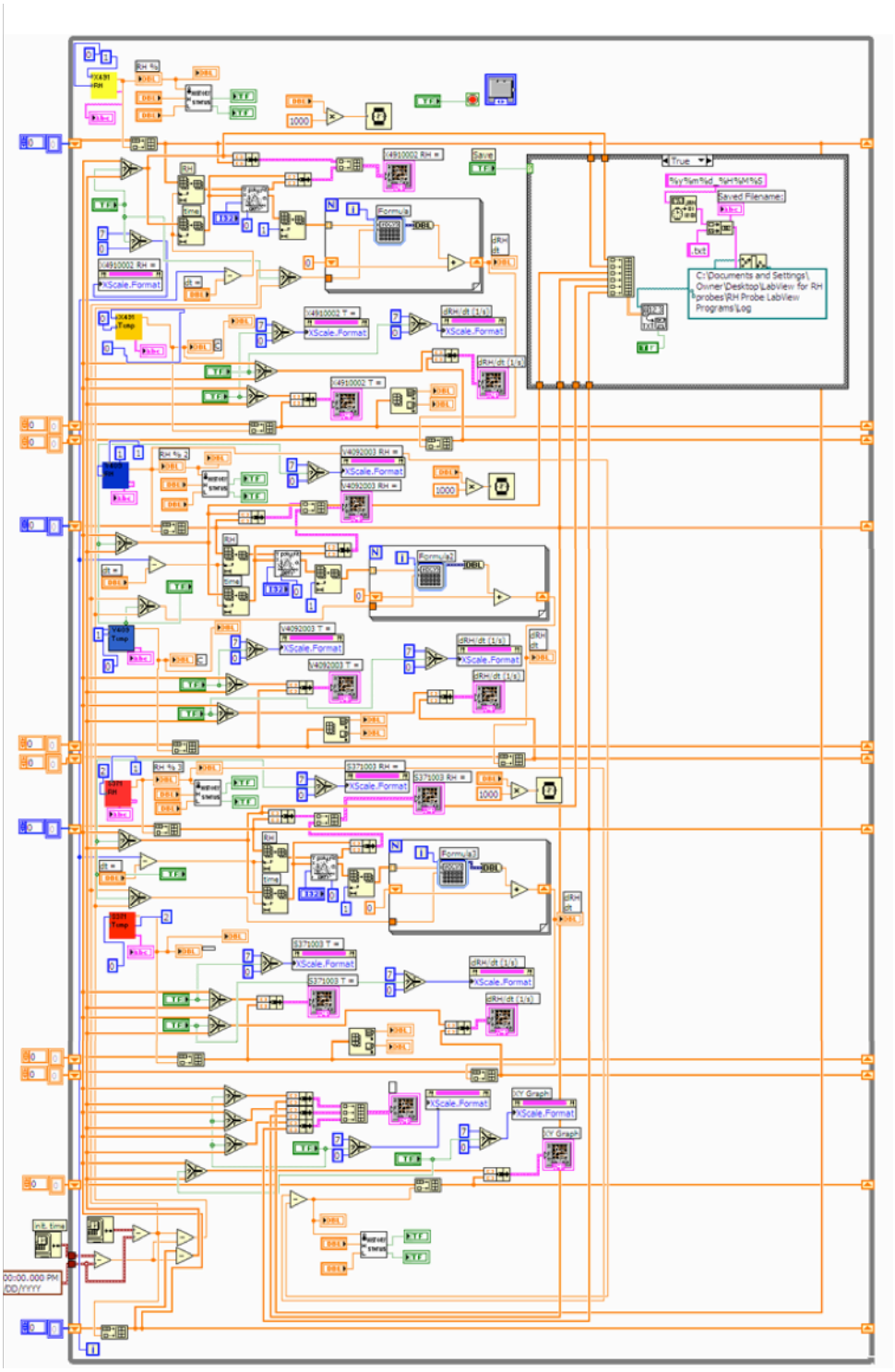

APPENDIX Ia: A block diagram of the custom LabView™ program used to monitor relative humidity.

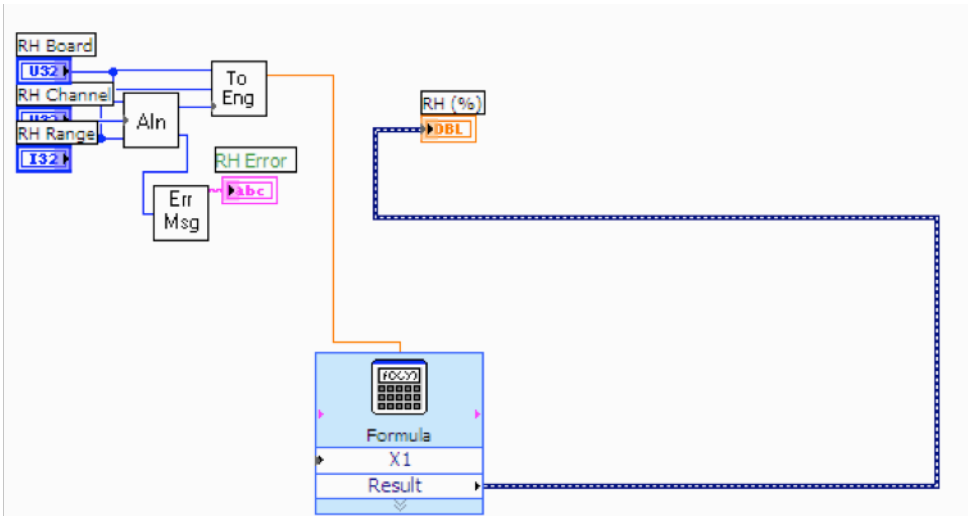

APPENDIX Ib: A block diagram of the custom virtual instrument (VI™) used for Vaisala Humidity probes in the LabView™ program used to monitor relative humidity.

APPENDIX II

A PDB structure file of one dodecyl sulfate anion.

```
ATOM   1374  C1  SDS X   1      20.680 -26.914 -17.977  1.00  0.00      SDS  C
ATOM   1375  C1  SDS X   1      20.680 -26.914 -17.977  1.00  0.00      SDS  C
ATOM   1376  C2  SDS X   1      20.659 -28.444 -17.986  1.00  0.00      SDS  C
ATOM   1377  C2  SDS X   1      20.659 -28.444 -17.986  1.00  0.00      SDS  C
ATOM   1378  C3  SDS X   1      22.095 -28.973 -17.975  1.00  0.00      SDS  C
ATOM   1379  C3  SDS X   1      22.095 -28.973 -17.975  1.00  0.00      SDS  C
ATOM   1380  C4  SDS X   1      22.074 -30.503 -17.983  1.00  0.00      SDS  C
ATOM   1381  C4  SDS X   1      22.074 -30.503 -17.983  1.00  0.00      SDS  C
ATOM   1382  C5  SDS X   1      23.509 -31.033 -17.972  1.00  0.00      SDS  C
ATOM   1383  C5  SDS X   1      23.509 -31.033 -17.972  1.00  0.00      SDS  C
ATOM   1384  C6  SDS X   1      23.488 -32.562 -17.981  1.00  0.00      SDS  C
ATOM   1385  C6  SDS X   1      23.488 -32.562 -17.981  1.00  0.00      SDS  C
ATOM   1386  C7  SDS X   1      24.924 -33.092 -17.970  1.00  0.00      SDS  C
ATOM   1387  C7  SDS X   1      24.924 -33.092 -17.970  1.00  0.00      SDS  C
ATOM   1388  C8  SDS X   1      24.903 -34.622 -17.978  1.00  0.00      SDS  C
ATOM   1389  C8  SDS X   1      24.903 -34.622 -17.978  1.00  0.00      SDS  C
ATOM   1390  C9  SDS X   1      26.338 -35.152 -17.967  1.00  0.00      SDS  C
ATOM   1391  C9  SDS X   1      26.338 -35.152 -17.967  1.00  0.00      SDS  C
ATOM   1392  C10 SDS X   1      26.318 -36.681 -17.976  1.00  0.00      SDS  C
ATOM   1393  C10 SDS X   1      26.318 -36.681 -17.976  1.00  0.00      SDS  C
ATOM   1394  C11 SDS X   1      27.753 -37.211 -17.965  1.00  0.00      SDS  C
ATOM   1395  C11 SDS X   1      27.753 -37.211 -17.965  1.00  0.00      SDS  C
ATOM   1396  C12 SDS X   1      27.732 -38.741 -17.973  1.00  0.00      SDS  C
ATOM   1397  C12 SDS X   1      27.732 -38.741 -17.973  1.00  0.00      SDS  C
ATOM   1398  OS1 SDS X   1      19.339 -26.419 -17.987  1.00  0.00      SDS  O
ATOM   1399  OS1 SDS X   1      19.339 -26.419 -17.987  1.00  0.00      SDS  O
ATOM   1400  OS2 SDS X   1      18.099 -24.434 -17.808  1.00  0.00      SDS  O
ATOM   1401  OS2 SDS X   1      18.099 -24.434 -17.808  1.00  0.00      SDS  O
ATOM   1402  OS3 SDS X   1      19.847 -24.461 -19.375  1.00  0.00      SDS  O
ATOM   1403  OS3 SDS X   1      19.847 -24.461 -19.375  1.00  0.00      SDS  O
ATOM   1404  OS4 SDS X   1      20.528 -24.584 -17.132  1.00  0.00      SDS  O
ATOM   1405  OS4 SDS X   1      20.528 -24.584 -17.132  1.00  0.00      SDS  O
ATOM   1406  S   SDS X   1     19.431 -24.900 -17.978  1.00  0.00      SDS  S
ATOM   1407  S   SDS X   1     19.431 -24.900 -17.978  1.00  0.00      SDS  S
ATOM   1408  H11 SDS X   1      21.207 -26.553 -18.860  1.00  0.00      SDS  H
ATOM   1409  H11 SDS X   1      21.207 -26.553 -18.860  1.00  0.00      SDS  H
ATOM   1410  H12 SDS X   1      21.190 -26.562 -17.081  1.00  0.00      SDS  H
ATOM   1411  H12 SDS X   1      21.190 -26.562 -17.081  1.00  0.00      SDS  H
ATOM   1412  H21 SDS X   1      20.149 -28.795 -18.882  1.00  0.00      SDS  H
ATOM   1413  H21 SDS X   1      20.149 -28.795 -18.882  1.00  0.00      SDS  H
ATOM   1414  H22 SDS X   1      20.132 -28.805 -17.103  1.00  0.00      SDS  H
ATOM   1415  H22 SDS X   1      20.132 -28.805 -17.103  1.00  0.00      SDS  H
ATOM   1416  H31 SDS X   1      22.622 -28.612 -18.858  1.00  0.00      SDS  H
ATOM   1417  H31 SDS X   1      22.622 -28.612 -18.858  1.00  0.00      SDS  H
ATOM   1418  H32 SDS X   1      22.605 -28.622 -17.078  1.00  0.00      SDS  H
ATOM   1419  H32 SDS X   1      22.605 -28.622 -17.078  1.00  0.00      SDS  H
ATOM   1420  H41 SDS X   1      21.564 -30.855 -18.880  1.00  0.00      SDS  H
ATOM   1421  H41 SDS X   1      21.564 -30.855 -18.880  1.00  0.00      SDS  H
ATOM   1422  H42 SDS X   1      21.547 -30.864 -17.100  1.00  0.00      SDS  H
ATOM   1423  H42 SDS X   1      21.547 -30.864 -17.100  1.00  0.00      SDS  H
ATOM   1424  H51 SDS X   1      24.036 -30.672 -18.855  1.00  0.00      SDS  H
ATOM   1425  H51 SDS X   1      24.036 -30.672 -18.855  1.00  0.00      SDS  H
ATOM   1426  H52 SDS X   1      24.019 -30.681 -17.076  1.00  0.00      SDS  H
ATOM   1427  H52 SDS X   1      24.019 -30.681 -17.076  1.00  0.00      SDS  H
```

```
ATOM   1428  H61 SDS X   1      22.978 -32.914 -18.878  1.00  0.00      SDS  H
ATOM   1429  H61 SDS X   1      22.978 -32.914 -18.878  1.00  0.00      SDS  H
ATOM   1430  H62 SDS X   1      22.961 -32.924 -17.098  1.00  0.00      SDS  H
ATOM   1431  H62 SDS X   1      22.961 -32.924 -17.098  1.00  0.00      SDS  H
ATOM   1432  H71 SDS X   1      25.451 -32.731 -18.853  1.00  0.00      SDS  H
ATOM   1433  H71 SDS X   1      25.451 -32.731 -18.853  1.00  0.00      SDS  H
ATOM   1434  H72 SDS X   1      25.434 -32.741 -17.073  1.00  0.00      SDS  H
ATOM   1435  H72 SDS X   1      25.434 -32.741 -17.073  1.00  0.00      SDS  H
ATOM   1436  H81 SDS X   1      24.393 -34.974 -18.875  1.00  0.00      SDS  H
ATOM   1437  H81 SDS X   1      24.393 -34.974 -18.875  1.00  0.00      SDS  H
ATOM   1438  H82 SDS X   1      24.376 -34.983 -17.095  1.00  0.00      SDS  H
ATOM   1439  H82 SDS X   1      24.376 -34.983 -17.095  1.00  0.00      SDS  H
ATOM   1440  H91 SDS X   1      26.866 -34.790 -18.850  1.00  0.00      SDS  H
ATOM   1441  H91 SDS X   1      26.866 -34.790 -18.850  1.00  0.00      SDS  H
ATOM   1442  H92 SDS X   1      26.849 -34.800 -17.071  1.00  0.00      SDS  H
ATOM   1443  H92 SDS X   1      26.849 -34.800 -17.071  1.00  0.00      SDS  H
ATOM   1444 H101 SDS X   1      25.807 -37.033 -18.873  1.00  0.00      SDS  H
ATOM   1445 H101 SDS X   1      25.807 -37.033 -18.873  1.00  0.00      SDS  H
ATOM   1446 H102 SDS X   1      25.790 -37.042 -17.093  1.00  0.00      SDS  H
ATOM   1447 H102 SDS X   1      25.790 -37.042 -17.093  1.00  0.00      SDS  H
ATOM   1448 H111 SDS X   1      28.280 -36.850 -18.848  1.00  0.00      SDS  H
ATOM   1449 H111 SDS X   1      28.280 -36.850 -18.848  1.00  0.00      SDS  H
ATOM   1450 H112 SDS X   1      28.263 -36.859 -17.068  1.00  0.00      SDS  H
ATOM   1451 H112 SDS X   1      28.263 -36.859 -17.068  1.00  0.00      SDS  H
ATOM   1452 H121 SDS X   1      27.222 -39.092 -18.870  1.00  0.00      SDS  H
ATOM   1453 H121 SDS X   1      27.222 -39.092 -18.870  1.00  0.00      SDS  H
ATOM   1454 H122 SDS X   1      28.755 -39.118 -17.966  1.00  0.00      SDS  H
ATOM   1455 H122 SDS X   1      28.755 -39.118 -17.966  1.00  0.00      SDS  H
ATOM   1456 H123 SDS X   1      27.205 -39.102 -17.090  1.00  0.00      SDS  H
ATOM   1457 H123 SDS X   1      27.205 -39.102 -17.090  1.00  0.00      SDS  H
```

A PDB structure file of a cluster of $(Na_2Cl)_4^+$

```
ATOM      1 CLA  CLA 0   1    -18.291 -18.291 -18.291  1.00  0.00      CLA CL
ATOM      2 CLA  CLA 0   2    -15.477 -18.291 -15.477  1.00  0.00      CLA CL
ATOM      3 CLA  CLA 0   3    -15.477 -15.477 -18.291  1.00  0.00      CLA CL
ATOM      4 CLA  CLA 0   4    -18.291 -15.477 -15.477  1.00  0.00      CLA CL
ATOM  28255  SOD SOD 0   1    -18.291 -21.477  15.477  1.00  0.00      SOD NA
ATOM  28256  SOD SOD 0   1    -18.291 -21.477  15.477  1.00  0.00      SOD NA
ATOM  28257  SOD SOD 0   2     -9.849 -21.477  18.291  1.00  0.00      SOD NA
ATOM  28258  SOD SOD 0   2     -9.849 -21.477  18.291  1.00  0.00      SOD NA
ATOM  28259  SOD SOD 0   3    -12.663 -21.477  15.477  1.00  0.00      SOD NA
ATOM  28260  SOD SOD 0   3    -12.663 -21.477  15.477  1.00  0.00      SOD NA
ATOM  28261  SOD SOD 0   4     -4.221 -21.477  18.291  1.00  0.00      SOD NA
ATOM  28262  SOD SOD 0   4     -4.221 -21.477  18.291  1.00  0.00      SOD NA
```